Data Report on Corrosion Testing of Stainless Steel SNF Storage Canisters

Fuel Cycle Research & Development

Sandia
National
Laboratories

APPENDIX E

FCT DOCUMENT COVER SHEET [1]

Name/Title of
Deliverable/Milestone/Revision No.   Data Report on Corrosion Testing of Stainless Steel SNF Storage Canisters___

Work Package Title and Number   ST Storage and Transportation Experiments - SNL FT-13SN080506

Work Package WBS Number   1.02.08.05

Responsible Work Package Manager   Charles R. Bryan / _(signature)_   September 30, 2013
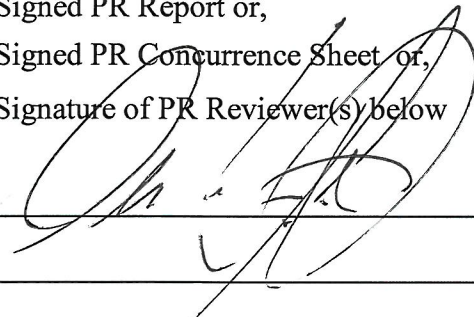   (Name/Signature)   Date Submitted

Quality Rigor Level for Deliverable/Milestone[2]	☒ QRL-3	☐ QRL-2	☐ QRL-1 Nuclear Data	☐ Lab/Participant QA Program (no additional FCT QA requirements)

This deliverable was prepared in accordance with   Sandia National Laboratories
                                                     (Participant/National Laboratory Name)

QA program which meets the requirements of

☒ DOE Order 414.1   ☐ NQA-1-2000   ☒ Other: FCT QAPD

This Deliverable was subjected to:

☒ Technical Review   ☐ Peer Review

Technical Review (TR)   **Peer Review (PR)**

Review Documentation Provided   **Review Documentation Provided**

☐ Signed TR Report or,   ☐ Signed PR Report or,

☐ Signed TR Concurrence Sheet or,   ☐ Signed PR Concurrence Sheet or,

☒ Signature of TR Reviewer(s) below   ☐ Signature of PR Reviewer(s) below

Name and Signature of Reviewers

Carlos Jove-Colon

_____   _____

_____   _____

_____   _____

NOTE 1: *Appendix E should be filled out and submitted with the deliverable. Or, if the PICS:NE system permits, completely enter all applicable information in the PICS:NE Deliverable Form. The requirement is to ensure that all applicable information is entered either in the PICS:NE system or by using the FCT Document Cover Sheet.*

NOTE 2: *In some cases there may be a milestone where an item is being fabricated, maintenance is being performed on a facility, or a document is being issued through a formal document control process where it specifically calls out a formal review of the document. In these cases, documentation (e.g., inspection report, maintenance request, work planning package documentation or the documented review of the issued document through the document control process) of the completion of the activity, along with the Document Cover Sheet, is sufficient to demonstrate achieving the milestone. If QRL 1, 2, or 3 is not assigned, then the Lab / Participant QA Program (no additional FCT QA requirements) box must be checked, and the work is understood to be performed and any deliverable developed in conformance with the respective National Laboratory / Participant, DOE or NNSA-approved QA Program.*

SUMMARY

This progress report describes work done at Sandia national Laboratories (SNL) to assess the localized corrosion performance of container/cask materials used in the interim storage of used nuclear fuel. A detailed evaluation of the environment to which these storage systems are exposed is included to provide context for the experimental evaluation of the effect of deliquesced salts on storage relevant steels. The results of dust deliquescence testing on 304SS obtained to date are presented and evaluated regarding feasibility of stifled localized corrosive attack.

Salt deliquescence can occur on interim storage containers only over a small part of the temperature and RH range that the storage containers will experience. A reasonable maximum possible absolute humidity is 40-45 g/m^3; for sea salts, this corresponds to a maximum temperature of deliquescence of ~85ºC. Existing experimental work investigating stress corrosion cracking (SCC) of stainless steel in marine environments indicates that SCC is likely to occur under storage conditions. However, test conditions may not be representative of field conditions for several reasons; sea salt may not be representative of what is on the container surfaces; exchange with atmospheric gases is limited in the experiments, and other components in the dust may either reduce or increase the corrosivity of deliquesced brines in the dust.

To address the uncertainty in the environment, the Electrical Power Research Institute and the U.S. Department of Energy have initiated a sampling program for in situ dust deposits on current storage containers. Sandia is collaborating with EPRI on the dust sampling, analyzing the dusts and aiding in data interpretation. Two samples of dust that were collected from the surface of interim storage containers at the Calvert Cliffs ISFSI were delivered to Sandia characterized using several different methods, including chemical analysis of the soluble and insoluble fractions, mineralogical analysis by scanning electron microscopy and X-ray diffraction, and others. Important results are that the soluble components in the dust are largely calcium sulfate; chlorides are present only in trace amounts. The low Na and Cl concentrations indicate that, despite the location of the Calvert Cliffs ISFSI adjacent to Chesapeake Bay, the salts deposited on the storage containers appear to be dominantly continental in origin as opposed to being marine. The analyzed soluble salts may not represent a corrosive environment, as the chloride load may be too light to support SCC, or the deliquesced brine composition may be insufficiently aggressive.

In an effort to determine if there is indeed a potential for deliquescent brines to result in extensive localized corrosion, or if any localized corrosion will stifle due to limitations as described above, a series of experiments has been (and continues to be) performed. Materials of interest have been decorated with thin layers of salt in the presence of an occluded geometry in an effort to establish if localized corrosion (i.e., crevice corrosion) could initiate and propagate under such conditions. In these experiments, no inert species were added, so potential physical sequestration of the brine by the dust layer due to capillary forces have been eliminated, allowing all of the material deposited on the metal surface to participate in the corrosion reaction.

Experiments performed on 304 stainless steel, a material used to manufacture interim storage containers for a number of manufacturers, demonstrated that

localized corrosion was able to initiate and propagate into the material. Assessment of stifling requires characterization of the extent of corrosion as a function of exposure time. While characterization of the test samples continues at this time, results to date from specimens with mass loadings from 50 to 200 $\mu g/cm^2$ of chloride bearing salt exposed to an elevated temperature and dewpoint for time intervals from 7 to 100 days suggest that stifling has not yet taken place. Additional tests and more detailed analyses are planned, as discussed below.

CONTENTS

FIGURES

TABLES

ACRONYMS

AH	absolute humidity
ATR	attenuated total reflection
BSD	[electron] backscatter detector
DOE	Department of Energy
EDS	energy dispersive [X-ray] spectroscopy
EPRI	Electrical Power Research Institute
FCRD	Fuel Cycle Research and Development
FSAR	Final Safety Analysis Report
FTIR	Fourier Transform Infrared Spectroscopy
GC-MS	Gas Chromatography-Mass Spectroscopy
IC	ion chromatography
ICP-OES	inductively coupled plasma-optical emission spectroscopy
ISFSI	Independent Spent Fuel Storage Installation
MCA	multiple crevice former assembly
NADP	National Airfall Deposition Program
RAI	Request for Additional Information
RH	relative humidity
RH_L	limiting relative humidity
NRC	Nuclear Regulatory Commission
SCC	stress corrosion cracking
SEM	scanning electron microscope
SNF	spent nuclear fuel
SNL	Sandia National Laboratories
XRD	X-ray diffraction
XRF	X-ray fluorescence

DATA REPORT ON CORROSION TESTING OF STAINLESS STEEL SNF STORAGE CANISTERS

1.   INTRODUCTION

This progress report describes work done at Sandia national Laboratories (SNL) to assess the localized corrosion performance of container/cask materials used in the interim storage of used nuclear fuel. A detailed evaluation of the environment to which these storage systems are exposed is included to provide context for the experimental evaluation of the effect of deliquesced salts on storage-relevant steels. The results of dust deliquescence testing on 304SS obtained to date are presented and evaluated regarding feasibility of stifled localized corrosive attack.

Following initial cooling in pools, spent nuclear fuel (SNF) is transferred to dry storage casks for longer term storage at the reactor sites. The storage cask systems are commonly welded stainless steel (304SS; Hanson et al. 2011) containers enclosed in ventilated concrete or steel overpacks. These cask systems are intended as interim storage until a permanent disposal site is developed, and until recently, were licensed for up to 20 years, and renewals also up to 20 years. In 2011, 10 CFR 72.42(a) (DOE 2011) was modified to allow for initial license periods of up to 40 years, and also, license extensions of up to 40 years. However, the United States does not currently have a disposal pathway for SNF, and these containers may be required to perform their waste isolation function for many decades beyond their original design criteria. A few license renewals for existing containers have already been carried out, and at some point, all existing containers will have to be recertified.

For most dry cask storage systems, passive ventilation is utilized to cool the casks within the overpacks, and large volumes of outside air are drawn through the system. As a result, atmospherically borne particulates (i.e., dust and aerosols) carried by the ventilation system will be deposited on the cask surface. This was demonstrated recently at an inspection of the independent spent fuel storage installation at the Calvert Cliffs Nuclear Power Station in Calvert Cliffs, MD (Gellrich 2012).

A portion of most atmospheric dusts consists of soluble salts. While the fraction of soluble salts in the particulates can be very small at locations far inland, for coastal locations, such as many interim storage sites, the fraction may be large. These salts may deliquesce to form brines on the surface of a storage container at temperatures well above the boiling point of water, and the resulting brines might be corrosive depending on the material used to construct the package. Stress corrosion cracking (SCC) of heat-affected zones near welds is of special concern, as it a well-documented mode of attack for austenitic stainless steels (including 304SS and 316SS) in marine environments (Kain 1990). A number of researchers have demonstrated that localized corrosion can take place under such situations on materials commonly used for interim storage containers, including 304SS (Cook et al. 2010; Shirai et al. 2011) and 316SS (Tani et al. 2009).

However, many uncertainties exist with respect to the composition of salts that are deposited on storage container surfaces, the degree to which those salts are modified by reactions with the atmosphere and with other phases in the dust, both before and after deliquescence, and the corrosiveness of the resulting brines. Moreover, little information is available for with respect to the salt loads on the container surfaces. Because of these uncertainties, the representativeness of the environments that have been used in corrosion testing of interim storage container materials to date is not clear. To meet the need for a better understanding of the environment on the surface of storage containers, the Electrical Power Research institute (EPRI) has initiated a sampling program for dust on in-service storage containers. Sandia is collaborating with EPRI analyzing the samples and aiding in data interpretation. One set of samples, from the Calvert Cliffs Independent Spent Fuel Storage Installation (ISFSI) is in the process of analysis. Preliminary results are presented here.

Some researchers have suggested that for highly corrosion resistant/passive materials, several factors will prevent extensive localized corrosion in the presence of a thin electrolyte layer such as might form be dust deliquescence. Turnbull (1997) demonstrated for cracks and crevices that if the cathodic reactions which support the dissolution taking place at the corrosion site are pushed into the occluded geometry of the crack/crevice, that the pH would increase (due to hydroxyl ion production at the cathode), resulting in an inhibiting effect. Essentially, by moderating the pH it would not be possible to form and maintain the critical crevice solution required for continued activity of the crevice. More recently, Payer (2008) and Kelly (2006) demonstrated that the capacity of the external cathode controls the extent to which a crevice may propagate. Furthermore, Payer demonstrated that the capacity of the cathode would be determined by the quantity of salt/contaminant available on the metal surface outside of the crevice, as it dictates the volume and properties of the brine layer. In addition to the electrochemical limitations, physical limitations (e.g., limited volume of brine coupled with consumption or sequestration of aggressive species in the corrosion product) can also play a role in governing the stability of a localized corrosion site.

In an effort to determine if there is indeed a potential for deliquescent brines to result in extensive localized corrosion, or if any localized corrosion will stifle due to limitations as described above, a series of experiments has been (and continues to be) performed. Materials of interest have been decorated with thin layers of salt in the presence of an occluded geometry in an effort to establish if localized corrosion (i.e., crevice corrosion) could initiate and propagate under such conditions. In these experiments, no inert species (e.g., silicate minerals) were added, so potential physical sequestration of the brine by the dust layer due to capillary forces have been eliminated, allowing all of the material deposited on the metal surface to participate in the corrosion reaction.

The chemical compositions of the brines that can form are a function of temperature, as well as the available constituent materials (SNL 2008). At very high temperatures, brines must be very nitrate rich relative to chloride, whereas at lower temperatures, the composition can be dominated by other species, such as chloride. In terms of the corrosiveness of the brine, both the chemistry (e.g., concentration of aggressive species) and the exposure temperature have a strong impact on corrosion processes.

Experiments performed to date on Alloy 22 and other nickel based alloys have demonstrated that, consistent with the modeling performed to date (Turnbull 1997; Kelly et al. 2006; Payer et al. 2008), localized corrosion cannot be supported, either in terms of initiation or propagation, with the small volume of electrolyte anticipated to be present due to deliquescence of salts in dust (Enos 2012). This was demonstrated to be true for multicomponent nitrate-rich brines as well as chloride-based brines at lower temperatures.

However, a series of experiments was performed on more susceptible stainless steels, SS303 (a free-machining stainless steel which has an elevated sulfur concentration) and SS304. In this case, localized corrosion was able to initiate and propagate into the material. While SS303 was too susceptible to be useful for analyses, SS304 has proved to be an effective material for evaluating the argument that localized corrosion, if it were to initiate, would stifle due to consumption of the reactants.

2.   INTERIM STORAGE ENVIRONMENT CONSIDERATIONS

2.1   Overview

Here, the possible environments on the surface of SNF interim storage containers are discussed, along with how they may evolve through time, and how the *in-situ* environment on storage container surfaces may vary from conditions used in experimental studies of storage container SCC. Many processes may affect the environment on the surface of the storage containers, and there is little data to assess current models. A sampling program has been initiated by the EPRI to meet that need. In collaboration with EPRI, Sandia is analyzing the samples and aiding in data interpretation. One set of samples, from the Calvert Cliffs Independent Spent Fuel Storage Installation (ISFSI), is in the process of analysis, and preliminary results are presented here.

2.2   Environment on the Surface of the Storage Container

2.2.1   Range of Conditions on the Storage Container Surface

The majority of SNF is stored in stainless steel storage containers which are enclosed in concrete or steel overpacks. As the stainless steel casks are shielded from the weather, formation of aqueous solutions on the metal surface can only occur by deliquescence or condensation. Three factors control whether deliquescence will occur: the temperature at the metal surface; the relative humidity (RH) at the surface; and the composition of salts deposited on the surface. Temperature and relative humidity are coupled. The water content of the air within the overpack will be the same as that of the ambient air outside the overpack, but the relative humidity at the container surface will vary with the temperature. At high container surface temperatures, corresponding to low relative humidities, salts cannot deliquesce and corrosion cannot occur. The actual relative humidity at which deliquescence occurs is controlled by the salt assemblage that is present. Recent work suggests that there is a temperature limit above which deliquescence is unlikely, and SCC cannot occur.

A sampling program for *in situ* dust deposits on current storage containers is currently underway, and will provide critical compositional data for new stress corrosion cracking studies. It will also allow evaluation of the applicability of existing studies of stainless steel stress corrosion cracking under conditions of dust deliquescence.

2.2.1.1   Temperature

Detailed predictions of the temperatures on the storage container surfaces are rarely available. Storage system final safety analysis reports (FSARs) generally only report maximum container surface temperatures, and often, the calculations are conducted utilizing bounding thermal loads and ambient temperature values. Some examples are provided in Table 1(NAC International 2005; Transnuclear Inc. 2007; 2008; Holtec International 2010). For larger storage containers, maximum surface temperatures can exceed 200ºC. However while the potential range of temperatures is quite large, not all of these conditions have to be considered for corrosion testing. As noted previously, SCC will not occur above a certain temperature, because the relative humidity cannot be sufficiently high to allow deliquescence cannot occur.

Table 1. Maximum waste package surface temperature estimates for several storage systems

Storage system	Container (Max. Heat load)	Ambient T, ºF (ºC)	Max. shell Temp., ºC
NAC UMS	24PWR (23.0 kW)	76 (24.4)	177
		106 (41.1)	194
	56BWR (23.0 kW)	76 (24.4)	191
		106 (41.1)	207
NUHOMS HSM-H	24PTH-S[A] (40.8 kW)	0 (-17.8)	186
		100 (37.8)	235
		117 (47.2)	237
	24PTH-L (31.2 kW)	117 (47.2)	203
	24PTH-S-LC (24.0 kW)	117 (47.2)	176
NUHOMS HSM-HD	32PTH[B] (34.8 kW)	115 (46.1)	208
	32PTH[C] (32.0 kW)	115 (46.1)	201
	32PTH[D] (26.1 kW)	115 (46.1)	187
HI-STORM	MPC-68 (38.0 kW)	80 (26.7)	233
	MPC-32 (38.0 kW)	80 (26.7)	242

[A] Flat SS heat shields
[B] Finned Al side shields
[C] Unfinned Al side shields
[D] Galvanized steel side shields

For several reasons, determining the surface temperature on a storage container at any given time is difficult. The initial temperature of each container will vary with the initial activity of the SNF it contains, and the surface temperatures evolve over time, as the radioactivity of the SNF decays and the thermal load decreases. Moreover, the temperature varies over the surface of the container, depending on the distribution of the heat-generating waste inside the container and on the air flow over and around the container in the ventilated overpack. A recent thermal model of a specific NUHOMS storage cask at the Calvert Cliffs Independent Spent Fuel Storage Installation (ISFSI) illustrates the temperature variability (Suffield et al. 2012). The model implements both radiative and conductive heat transfer, as well as heat loss due to convective air flow through the overpack. Predicted surface temperatures on the 24PWR storage container (which contains fuel removed from the reactor 25-30 years ago) varied over a range of 90ºC, from 27ºC to 122ºC (the assumed ambient temperature was ~14ºC). For this horizontally emplaced cask, the ends were coolest, and the lower surface, where the incoming air first contacted the package, was much cooler than the upper surface. Although the actual temperatures and the range of temperatures will vary with the storage system design and the spent fuel load, it is apparent some regions of the storage container surface will cool sufficiently for deliquescence, and potentially SCC, decades earlier than other regions.

Predicted waste package surface temperatures control the RH at the surface, and can be used to estimate when conditions of deliquescence will be present. The resulting "time of wetness" model can be combined with measured corrosion penetration rates to estimate penetration over time. This approach has been used to estimate penetration on the bottom of a vertical storage cask emplaced on a concrete pad (Shirai et al. 2011). However, it is apparent that such a model would be very difficult to parameterize for

storage containers across the nuclear waste complex, as it would not only require complex thermal modeling of each individual container and heat load (the number, history, and burnup characteristics of each assembly), but also would have to be specific to individual locations on the waste package surface corresponding to welds. For instance, for the NUHOMS horizontally-emplaced container, the timing of deliquescence and total time of wetness for a longitudinal weld would vary not only with the radial location of the weld, but also along the length of the weld, with deliquescence occurring sooner at the cooler regions (lower surface and container ends). The surface temperature would potentially drop below the nominal 85ºC upper limit for deliquescence many decades earlier at cooler regions than at hotter regions.

2.2.1.2   Relative Humidity

Relative humidity (RH) is the ratio of the partial pressure of water vapor in air (P) to the saturated vapor pressure at the same temperature (P_{sat}). As ambient air with a given water content (or absolute humidity, AH) advects through a storage system and heats up, P does not change, but P_{sat} increases, so the RH drops. The RH at the container surface is controlled by the water content in the outside air and the temperature at the container surface. This is illustrated in Figure 1, for three different absolute humidities. A reasonable upper bound for the water content in the ambient air is 45 g/m^3, corresponding an RH of 100% at 95ºF (35ºC). In Figure 1, conditions to the left of this line are accessible under interim storage conditions. Also shown on this figure are the deliquescence RH values for several potentially relevant salts or salt assemblages, including NaCl, MgCl$_2$, and sea salts. It is important to note that experimentally, corrosion is observed at RH values significantly lower than the deliquescence RH, implying that even very thin adsorbed water films are sufficient to cause corrosion. The RH values at which corrosion occurs are referred to as the limiting RH (RH$_L$). The RH$_L$ is a strong function of the cleanliness of the surface, the nature of the surface oxide, and the speciation of the ionic contaminants on the surface. At values above the deliquescence RH, the activity of water in the brine is equivalent to the RH expressed as a unit value; as RH increases, solutions on the container surface become progressively more dilute. At RH values below the RH$_L$, corrosion cannot occur; at sufficiently high RH values, the deliquesced solution is too dilute to support SCC.

It should be noted that some nitrate-chloride salt mixtures have been shown to deliquesce at very low relative humidities, and may never dry out, instead transitioning to molten salt mixtures as temperatures increase (SNL 2008). The potential relevance of these mixtures to interim storage conditions is not known; however, at inland sites, atmospheric salts are nitrate-rich, as discussed in the next section.

2.2.1.3   Salt Composition

As noted in the previous section, the composition of the salts on the container surface will determine the temperature at which deliquescence will occur. Many ISFSIs are in near-marine settings, and salts in dust and aerosols are expected to be dominated by salts from sea water. Table 2 lists the composition of ASTM D1141-98 synthetic sea water (ASTM International 2008), which is widely used in corrosion experiments to represent sea spray. As can be seen, sea salt is dominated by sodium-magnesium chloride-sulfates. It should be noted, though, that while sea water may represent the most important source of salts in near-marine environments, it is not the only one. Rainwater and fog in near-marine environments are not pure sea salts, but contain variable but generally quite significant amounts of ammonium and nitrate, and are enriched in sulfate relative to sea salts (EPRI 2006). For marine aerosols, reactions with atmospheric volatiles may greatly modify the composition of sea-salt particulates. Reactions with nitric acid and acidic sulfur compounds in the atmosphere act to convert sea salts to nitrate and sulfate compounds, accounting for the enrichment of these species in atmospheric aerosols in near-marine areas and even above the oceans. Sea-salt chloride in sea breezes on the west shore of the Iberian Peninsula is depleted by 67% and 24% for fine and coarse particles respectively, by the time the air mass reaches the coast (Pio and Lopes 1998).
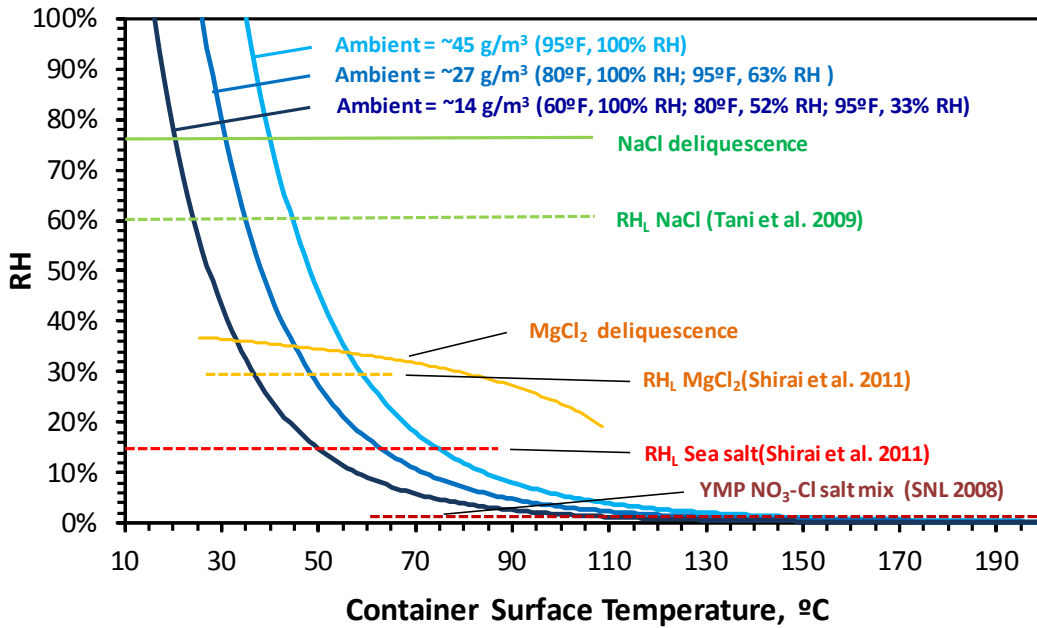
Figure 1. Relationship between RH, surface temperature, and conditions of deliquescence for potentially relevant salt assemblages.

Table 2. Composition of ASTM Ocean Water and Typical Inland Rainwater.

Species	Syn. ocean water, mg/L	Iowa rainwater, μeq/L
NH_4^+	—	29.22
Na^+	11031	2.045
K^+	398	0.511
Mg^{2+}	1328	3.208
Ca^{2+}	419	16.766
Cl^-	19835	1.975
Br^-	68	ND
F^-	1	ND
SO_4^{2-}	2766	17.685
NO_3^-	—	15.565
BO_3^{3-}	26	ND
HCO_3-	146	ND
pH	8.2	ND

At inland sites, atmospheric salts are largely derived from anthropogenic activities, terrestrial sources, and atmospheric reactions with marine salts (Hitchcock et al. 1980; Rossi 2003). Typical rainout data from an inland site in Iowa (NADP 2013) is shown in Table 2. Inland atmospheric salts are dominantly ammonium-calcium-nitrate-sulfates, with only minor chloride. It should be noted, however, that rainout data represent the atmospheric salt load, not composition of materials deposited as dust and aerosols on a storage container.

Chloride is generally the species of concern with respect to corrosion, although other industrial contaminants such as SO_2 are also important. For stainless steels, nitrate is protective. For this reason, marine environments are of greatest concern, and experimental work on SNF storage canister corrosion has largely focused on sea salt and its components. Magnesium chloride is especially important, as it deliquesces at very low relative humidities, and produces a brine with high chloride contents. Since a mixture of salts will deliquesce at a lower RH than any single component within it, sea salt deliquesces at an even lower RH than $MgCl_2$.

2.2.2   Experimental Work Evaluating SCC of Interim Storage Containers

2.2.2.1   Summary of Existing Experimental Work

Experimental work assessing SCC due to deliquescence of sea spray or its components, conducted over a range of RH values, temperatures, and salt loads, is summarized in Figure 2. Also shown are the absolute humidity isopachs from Figure 1. The salts used include NaCl, the major component in sea water; $MgCl_2$, which is largely responsible for the low deliquescence RH of sea salts; synthetic sea spray as per ASTM D1141-98; and bittern, the near-neutral, magnesium chloride-rich brine residue produced by seawater evaporation for NaCl production. SCC was observed under many environmental conditions that are relevant to interim storage, and also in some experiments that were run at higher water vapor pressures than are achievable for field conditions). No SCC was observed under dry (high temperature, low RH) conditions, or in cool, high RH (dilute) conditions, indicating that the test methods were largely appropriate for determining aggressive environments. If the experimental conditions are relevant to storage conditions, the data strongly suggest that SCC may be a concern for stainless steel interim storage containers. It is also relevant to note that pitting (a form of localized attack) was observed under nearly all test conditions.

Inland environments are considered to be less aggressive than chloride-rich near-marine locations, and no testing has been carried out using dusts or salts characteristic of inland sites.
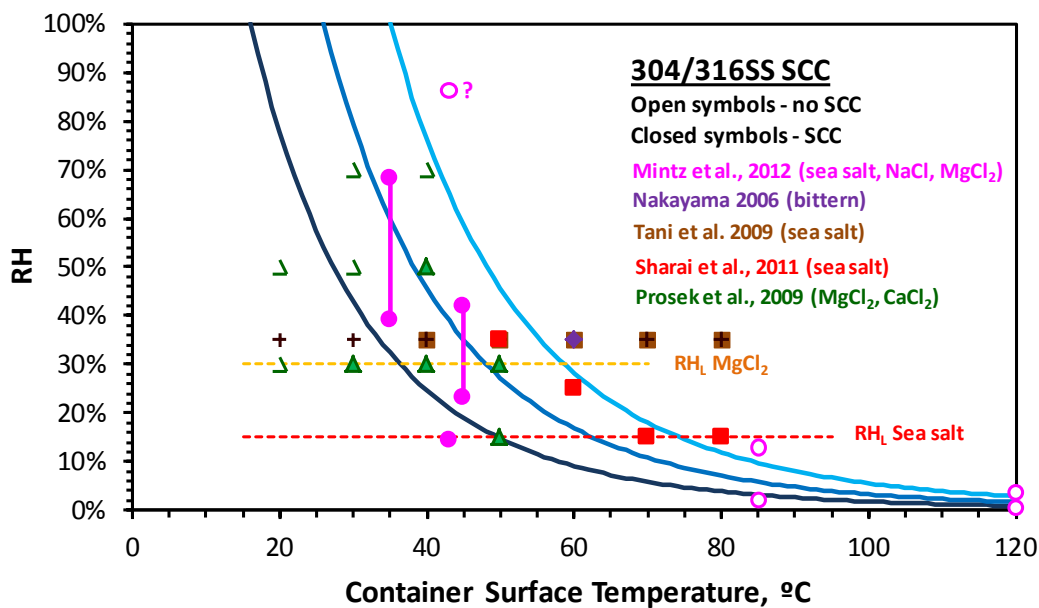
Figure 2. Summary of stainless steel SCC corrosion experiments with sea water components.

2.2.2.2   Relevance of the Environmental Conditions Used in Testing

The general methods used for corrosion testing are differ from field conditions in several ways: (1) deposited salts are not sea salt, but will contain significant amounts of ammonium, nitrate, and other components; (2) salts are deposited directly on the metal surface in relatively large amounts, and temperature and RH conditions are rapidly adjusted to the test conditions at which deliquescent brines are present; (3) air flow through the systems is low relative to advective flow through an overpack; and (4) real dusts on a storage container will be an admixture of salts, inorganic mineral phases, volatile and semi-volatile organics, more refractory organics (e.g., plant fibers, pollen), and possibly cementitious material from the overpack.

Several processes occurring in the natural systems will not occur, or will be minimized, in the laboratory systems. These include exchange reactions with the atmosphere and reactions with organics or mineral phases in the salt which may change the deliquescent brine chemistry.

Exchange Reactions with the Atmosphere

Possible exchange reactions with the atmosphere include acid degassing, equilibration with atmospheric CO_2, and decomposition of ammonium minerals/ ammonium degassing. At low pH, concentrated, deliquesced brines will produce partial pressures of acid gases (HCl, HNO_3) that are higher than the concentrations in ambient air. The brines degas the acid gases, resulting in loss of the acid gas anions (Cl^-, NO_3-) from solution. The solution pH rises, and the acid gas partial pressures decrease until (1) they are equal to that of the ambient air; or (2) a buffering reaction occurs which stabilizes the pH. One buffering reaction involves adsorption of CO_2 from the atmosphere and precipitation of carbonate. For a sodium-rich brine, this occurs only at high pH (>10), because of the high solubility of sodium carbonate phases. For a magnesium-rich brine, saturation with magnesite and precipitation occurs between pH 6 and 7. A second buffering reaction for Mg-rich brines is precipitation of Mg-hydroxy-chlorides. Because this reaction is internally buffered, it can occur rapidly under some conditions. At 150ºC, deliquesced $MgCl_2$ brine has been experimentally shown to rapidly convert to nondeliquescent $Mg(OH,Cl)_2$. While this temperature is excessive for long term interim storage, it does illustrate that acid degassing can potentially change brine composition over the long term. The effect of acid degassing is always to raise the pH; if a buffering reaction such as precipitation of carbonate occurs such that the degassing reaction can go to completion, then dryout may also occur (SNL 2008). In field conditions, for salts deposited over a period of years or decades in a storage container experiencing exposure to large volumes of air, it is likely that degassing will limit brine pH, and may result in precipitation of non-deliquescent Mg carbonate or hydroxyl-chloride. In a laboratory testing setting, these effects are minimized by rapid deposition of relatively large amounts of salt, and low rates of ventilation.

For ammonium-bearing salt assemblages, ammonia degassing is an important process. Prior to deliquescence, ammonium salts decompose via the following reactions:

$$NH_4Cl(s) \leftrightarrow NH_3(g) + HCl(g) \qquad\qquad (1)$$

$$NH_4NO_3(s) \leftrightarrow NH_3(g) + HNO_3(g) \qquad\qquad (2)$$

$$(NH_4)_2SO_4(s) \leftrightarrow 2NH_3(g) + H_2SO_4 (g) \qquad\qquad (3)$$
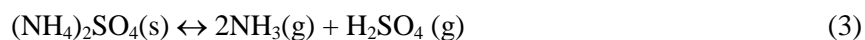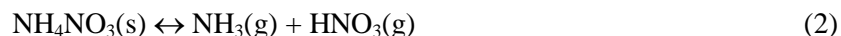
As ammonia degasses, there is concomitant loss of an acid gas species. Experiments with bulk salts show that ammonium chloride and ammonium nitrate reactions are very rapid even at moderately elevated temperatures. At 100ºC, the reaction is complete within days or weeks; even at 50ºC, a large fraction of the minerals will be lost over years. Ammonium sulfate decomposition is much slower, but is complete in less than 1 year at 100ºC (SNL 2008). For fine particulates, loss is rapid even at ambient temperatures—loss of nitrate due to volatilization of particulate ammonium nitrate from sampling filters is a widely recognized bias in atmospheric dust sampling (Zhang and McMurry 1992; Chang et al. 2000). It is evident that ammonium salts deposited on a hot dry storage container will decompose rapidly, taking

a significant fraction of acid gas anions with them. The ratio of cations removed is a function of the identity of the salt phases—for atmospheric aerosols, most ammonium is associated with sulfate, and to a lesser degree, nitrate (Seinfeld 1986).

Salt deposition, however, is an ongoing process, and will continue to occur after conditions cool to the point of deliquescence. Once ammonium salts fall onto existing deliquesced brines, they will dissolve and the brine will degas ammonia and acid gas cations in proportion to their equilibrium vapor pressure above the brine; the identity of the cation lost is no longer a function of the original mineral ion association. Little has been done to evaluate the composition of salts on inland storage containers. However, it is likely that the original deposited composition, perhaps similar to the Iowa rainwater composition in Table 2, will be extensively modified by ammonia and acid gas loss, and potentially carbonation, over long time spans on the heated package surface. These reactions may not be beneficial—nitrate is likely to be lost preferentially to chloride. In near-marine environments, ammonia is a relatively minor component of the atmospheric salt load, but ammonia degassing may still have some role in modifying deposited dust compositions.

Reactions with Other Dust Components (Organics, Minerals)

A large fraction of dusts is likely to be organic in nature, including plant materials (pollen, plant fibers) naturally occurring organic acids, and in industrial settings anthropogenic volatile compounds such as components in diesel fuel. Insoluble organic compounds do not appear to significantly affect the RH at which deliquescence occurs (Ming and Russell 2002; Parsons et al. 2004) but soluble organics, when added to an inorganic salt mixture, lower the deliquescence point of the mixture, and raise the water content at a given RH (Marcolli et al. 2004a; Marcolli et al. 2004b). Thus, organic compounds may affect the temperature at which deliquescence occurs, and the salt concentration of the resulting brine.

Organic compounds may also react with and consume nitrate in dust. Atmospheric dusts and dusts collected in the underground tunnels at the Yucca Mountain Site experienced order-of-magnitude losses in nitrate upon heating to 180ºC (Peterman 2008; 2009) The atmospheric dust concomitantly lost similar amounts of ammonium, suggesting that ammonium nitrate volatilization was responsible. The underground dusts were very low in ammonium, and the nitrate loss was attributed to reaction with organics in the dust. However, even if this is initially an important effect on the hot storage container, temperatures would eventually fall to the point that reactions between nitrate and organics would not be kinetically favored.

Alteration or dissolution of low solubility minerals such as clays and other silicates potentially buffer the pH of deliquescent brines in dust to near-neutral values (SNL 2008). However, these reactions may be kinetically limited; occurring too slowly to effectively modify brine compositions.

2.2.3   Summary

In this section, we summarize expected conditions on the surface of stainless steel SNL interim storage containers, and assess the relevance of those conditions to test conditions in published articles evaluating corrosion of those containers. The range of potential surface temperatures is large, with maximum potential surface temperatures as high as 250ºC; however, only conditions that may lead to the presence of a deliquesced water film must be considered in testing. Deliquescence is a function of the ambient RH, which controls the absolute humidity at the storage container surface, and the composition of the deposited salts. A reasonable maximum possible absolute humidity is 40-45 g/m^3; for sea salts, this corresponds to a maximum temperature of deliquescence of ~85ºC. However, it should be noted that complex mixtures of nitrate and chloride salts, potentially relevant at inland sites and even at coastal sites, may deliquesce at much higher temperatures.

Existing experimental work investigating stress corrosion cracking of stainless steel in marine environments indicates that SCC is likely to occur under storage conditions. However, test conditions may not be representative of field conditions for several reasons. The experiments use synthetic sea water

as the salt source, while field studies show that other salt components, including ammonium and nitrate, are significant in atmospheric aerosols even in near-marine environments. Moreover, experimental designs limit gas-phase exchange with the atmosphere relative to field conditions. In the field, acid degassing and CO_2 exchange may contribute to the dry-out of Mg-chloride brines by conversion to Mg hydroxychlorides or carbonates. Also, reactions with atmospheric components (nitric and sulfuric acid) results in the conversion of aerosol sea-salt chlorides to nitrates and sulfates, such that deposited salts may significantly vary from the sea salts used experimental studies. Finally, experiments do not assess the effects of other components in dust, such as organics or pH-buffering minerals, in either reducing or increasing the corrosivity of deliquesced brines in dust.

Deposited salts may not resemble the atmospheric salt load, which varies compositionally with particle size. Moreover, particles generated from the concrete overpack may contribute to the dust load on the package. Also, once deposited on the hot container surface, deposited salts will evolve over time by exchange with the atmosphere and reaction with other components in the dust. The Electrical Power Research Institute and the U.S. Department of Energy have initiated a sampling program for *in situ* dust deposits on current storage containers. This program will provide critical compositional data for new stress corrosion cracking studies, and will allow evaluation of the applicability of existing studies of stainless steel stress corrosion cracking under conditions of dust deliquescence.

2.3   Analysis of Dusts Collected from the Surface of In-Service Interim Storage Containers

This section summarizes the results of analysis of dust samples collected from the surface of Spent Nuclear Fuel Storage Containers at the Calvert Cliffs ISFSI. Interim storage systems at the site are NUHOMS horizontal storage modules (HSM), consisting of a concrete overpack, into which a stainless steel (304L) storage cask is placed horizontally (Figure 3). The system is passively ventilated via air inlet vents at the base of the unit, and outlet vents on the top. Decay heat from the waste drives convective airflow through overpack, cooling the container. Over time, dust, drawn into the overpacks with the circulating air, is deposited on the surfaces of containers within the storage systems. Salts within the dust will deliquesce as heat production declines over time and the packages cool, and it is possible that deliquescence-induced corrosion of the 304L waste container could lead to penetration of the container walls by chloride-induced SCC.

To address this concern, in June, 2012, an overpack was opened, and the surface of the waste container was examined with remotely deployed cameras. In addition, EPRI, working with the plant operator, collected samples of the dust and salts on the container surface using two methods:

- A "SaltSmart©" sensor was placed on the canister and then retrieved; this device leaches salts off the surface using a wet sponge, and provides a direct reading of the conductivity of the salts thus removed. Later, the dried sponge was leached, and the entrained salts were analyzed by wet chemical methods.

- A scraper tool was used in an attempt to sample loose dust on the container surface. This device consisted of a steel head with an abrasive sponge backed with a filter pad for capturing >5 µm particles. The sampler was attached to a vacuum line and a long rod, and was inserted into the overpack through the annulus around the package at the front entrance. The sampler head was designed such that, when rubbed over the container surface, dust dislodged by the abrasive sponge would be pulled through the sponge and collected on the filter.

Figure 3. NUHOMS horizontal storage module, at the Calvert Cliffs ISFSI, with doorway open for storage container insertion. The air inlet vent is below the door (Figure 1.2, Suffield et al., 2012).

The remote observations of the container surface indicated that the dust load was significant, especially on the top of the container (Figure 4); however, the top of the container proved to be inaccessible during the sampling. Instead, samples were taken from regions on the side of the container, with a much lighter coating of dust. The on-site SaltSmart© readings indicated a significant amount of soluble salts were present, and this generated some concern that chloride-induced SCC could indeed occur at the site. Later analysis of the dried sponge and of two of the dry dust samples indicated that the majority of the soluble salts present were not chlorides, reducing the possibility of SCC. However, there was some question especially with the analysis of the dried SaltSmart© sponge, that chloride might have been lost by degassing during storage, as the sponge dried out. The post-test analyses of the SaltSmart© and dry dust samples are documented in a response to a Nuclear Regulatory Commission (NRC) Request for Additional Information (RAI) by the plant owners in June 2013 (Calvert Cliffs Nuclear Power Plant LLC 2013a).

To further assess the composition of the salts, and of the dusts, the two remaining sample heads were sent to Sandia for characterization. The heads were disassembled and the abrasive pads and filters were removed for analysis. The following analyses were used to characterize the dust and salts:

- Scanning Electron Microscopy (SEM) imaging and energy dispersive system (EDS) element mapping. SEM/EDS analysis provides textural and mineralogical information of dust/dust components, and allows visual identification of organic matter (floral/faunal fragments)

- X-ray fluorescence (XRF) analysis. This method was implemented as a microbeam technique, allowing chemical mapping of the filter/pad surfaces with a resolution of ~50 µm. It provides semi-quantitative chemical analyses; yielding element ratios that can be used in mass balance and normative mineral calculations. However, one limitation is that elements lighter than sodium (e.g. oxygen, nitrogen, carbon) cannot be detected.

Figure 4. Photograph of dust on the surface of the waste container, Calvert Cliffs container inspection, June, 2012.

- X-ray diffraction (XRD) analysis of the dust on the abrasive pads and filters. This in-situ analysis provides mineralogical information on the dust.

- Gas Chromatography-Mass Spectroscopy (GC-MS) analysis. Stepwise thermal decomposition was used to evolve volatile and semi-volatile components in the dust. By analyzing at progressively higher temperatures, organic compounds released prior to breakdown of the organic substrates (the pads and filters) could be analyzed.

- Analysis by Fourier Transform Infrared Spectroscopy (FTIR). As with the GC-MS, this method was used to identify volatile and semi-volatile organics in the dust. Samples were treated with solvents, and the solvents analyzed to determine the organic components leached from the sample.

- Raman spectroscopy. This microscopic technique provides mineralogical/compositional information of individual dust grains, including both organics and silicates, if the grains are sufficiently large.

- Chemical analyses of the dust and soluble salts. The abrasive pads and filters were leached with deionized water, and the leachate was analyzed by to determine the composition of the soluble salts. The insoluble fraction was also digested and analyzed to determine the bulk chemistry of the material.

In the following sections, the results of these analyses are presented and discussed.

2.3.1   Samples and Methods

2.3.1.1   Samples

Following use at Calvert Cliffs, the dust sampling tools were stored at EPRI. The heads were stored at room temperature in Ziploc© plastic bags prior to being sent to Sandia. In June, 2013, the remaining two the sampling heads from the Calvert Cliffs sampling episode were sent to Sandia for analysis. Also sent were unused samples of both the abrasive sponge and the filter pad, for use as analytical blanks. Upon arrival, it was observed that the plastic bags containing the sample heads contained some loose dust, and

also, that they were heavily abraded on the inside by the abrasive sponge—it was likely that some of the plastic (polyethylene) contaminated the abrasive pad. The two samples that were sent to Sandia were labeled "#1" and "#4", and are hereafter referred to as EPRI #1 and EPRI #4, respectively.

The sampling heads were disassembled, and the abrasive pads and filters were extracted, generating two subsamples, the pad and the filter, for each sample. These were photographed immediately upon disassembly, and photographs are provided in Figure 5. Adhering dust was observed both pads, especially along the edges, and both filters were discolored, indicating that dust matter had been pulled through the pad and deposited on the filters. Filter EPRI#1 as more strongly discolored, suggesting a greater amount of dust was present. Along with the pad and filter blanks, a total of six samples were analyzed.

The abrasive pads used for the Calvert Cliffs sampling are Scotch-brite© Type 7440 pads, made by 3M Company. The material safety data sheet for the pads indicates that the pads are nylon fibers (5-15 wt%), with aluminum oxide as the abrasive (45-65 wt%),bound together with a cured resin (15-40 wt%). A small amount of titanium oxide (0.5-2.75 wt%) is present; later analysis showed that it was primarily present in the white letters stenciled on the back surface of the pad. The filters (Mc Master-Carr Company #51625K11) are polyester fiber pads about 2 mm thick; they are rated as 5 µm filters.
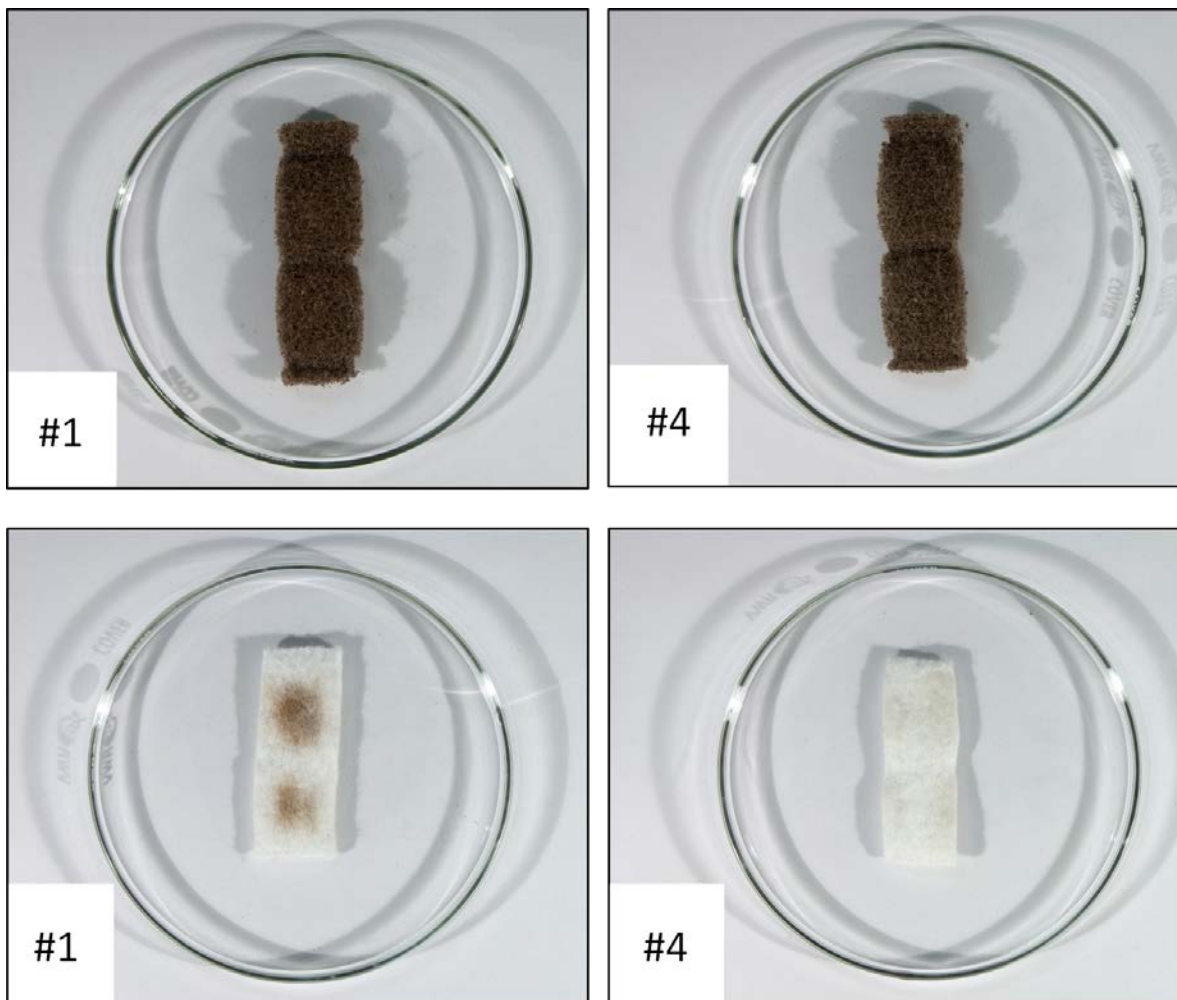

Figure 5. Photographs of the abrasive pads (top row) and filters (bottom row), from samples EPRI #1 and EPRI #4.

Prior to analysis, each sample was subdivided into several pieces. Approximately ½ of each sample was retained for non-destructive XRF/XRD analysis, followed by leaching and chemical analysis. The remaining half was subdivided into four pieces, for analysis by (1) FTIR/Raman; (2) SEM/EDS; and (3) GC-MS; the final piece was reserved as a backup.

2.3.1.2   Methods

SEM analysis

Samples fractions retained for SEM analysis were plasma-coated with gold to reduce sample charging during analysis. Imaging and element mapping was done with a Carl Zeiss Supra^{Tm} 55VP SEM, equipped with an Oxford X-Max EDS detector and Aztec$^©$ software. An accelerating voltage of 15 KeV was used, and working distances of 7.1 to 9.4 mm, with varying degrees of magnification. Images were obtained using both secondary and backscattered electron imaging. A relatively high beam current was used to produce a high count rate and facilitate rapid element mapping. However, the elevated beam current did enhance sample charging for the fibrous pad samples, resulting lower image quality in some cases.

XRF analysis

X-ray fluorescence (XRF) mapping was accomplished using a Bruker M4 Tornado micro-XRF system. This energy dispersive system was equipped with a micro-focus Rhodium X-ray source operated at 50 keV and 200 µA. The spatial resolution was ~30 µm, dictated by a poly-capillary focusing optic (lens) attached to the x-ray source. Mapping was performed via an XY translation stage. An XFlash® Silicon Drift Detector was employed for data collection. Samples were run under vacuum atmosphere (5×10^{-3} Torr). The summed X-ray spectrum was processed to produce a semi-quantitative chemical analysis for the filter/pad and the dust on the sample surface. The XRF analysis is not complete, as elements lighter than Na cannot be analyzed, but it provides element ratios which, in combination with the wet chemical analysis, can be used to estimate the concentration of silica in the sample. Sample sizes were too small to analyze silica directly via wet methods.

XRD analysis

XRD analysis was performed using a Bruker D2 Phaser diffractometer with a Cu Kα X-ray source, and a LynxEye solid-state energy discriminating X-ray detector. Samples were analyzed "as-received," with minimal modification, directly on the filters (the abrasive pads were too coarsely porous to allow in-situ XRD analysis).

GC-MS analysis

For GC-MS analysis, the filter/pad aliquots were cut approximately in half and tested for volatile and semi-volatile organics using thermal desorption GC-MS. A first round of testing was performed in a "split" model to mitigate possible overload of the instrumentation due to filter or Scotchbrite© pad decomposition. An additional round of testing was performed in a "no-split" mode which has lower detection limits (~100 nanograms). Samples were tested using a Perkin Elmer Turbo Matrix ATD thermal desorption unit. Samples were placed into a pre-conditioned thermal desorption tube (Supleco 28174-U Glass Thermal Desorption Tubes, ¼" (6.35 mm) O.D. and 3.5" (89 mm) long), and desorbed at multiple temperatures (100C, 200C, 250C°C) for a specified time. Desorbed samples are sent via heated transfer line to an Agilent 6890N with a Restek Rxi-5 column (60 m × 0.32 mm × 1.0 um), and peaks detected with an Agilent 5975 Inert XL mass spectrometer.

FTIR analysis

For Fourier Transform Infrared (FTIR) spectroscopy analysis, the filter and pad samples were sequentially leached, first with isopropanol to extract polar organics, and then with hexane, to extract nonpolar hydrocarbons. The leachate was deposited on a trapezoid-shaped, ZnSe attenuated total reflection (ATR) element and allowed to evaporate, depositing any leached substances. The ATR

accessory was placed in a Nicolet Nexus 870 Fourier Transform Infrared Spectrometer, and infrared spectra were obtained of the residues present on the ATR element. Attempts to obtain infrared spectra of any dust on the filters/pads by contacting them with the surface of the small, diamond ATR element in a "DurasamplIR" accessory were not successful, probably because intimate contact of the sample to the ATR element surface could not be achieved. Components in the infrared spectra were identified by functional group analysis combined with comparison to a reference library of infrared spectra.

Raman analysis

Raman spectroscopy and infrared spectroscopy are complementary techniques that are useful in identifying molecular species, both organic and inorganic. However, instead of the absorption of photons by vibrational motions as employed in infrared spectroscopy, Raman spectroscopy utilizes inelastic scatter of photons as they interact with the vibrational modes, with a laser as the source of photons. Incorporating a microscope into the Raman system makes possible resolution and detection on the microscopic scale. For this analysis, a small part of each sample was gently tapped onto a salt plate to dislodge dust particles. The dislodged particles were illuminated by a focused laser beam under a microscope, and individual grains were selected for analysis using a Raman spectrometer with a charge-coupled-device detector to record spectra of scattered photons. The mineralogy of the grain was determined by use of a search-match routine, which compared the collected spectra to a reference library of spectra.

Chemical analysis

The composition of soluble salts and insoluble minerals in the dust was determined by wet chemistry. The samples used were the filter/pad aliquots reserved for non-destructive XRD/XRF analysis. Following those analyses, the samples and blanks were weighed (to allow accurate correction for the blank values). Then, each sample was placed in a beaker with 10 mL of deionized water and gently agitated for 20 minutes. After leaching, the fiber filters and the abrasive pads were treated differently. The filters and liquid were transferred to a filtering funnel lined with Whatman 541 ashless filter paper. The water was allowed to drain into a 25 ml Class A volumetric flask, and the fiber filter and the Whatman filter paper were repeatedly rinsed to transfer all soluble salts into the flask. Once thoroughly rinsed, the Whatman filter and the fiber filter, along with the insoluble components in the dust, were removed from the funnel and placed in a weighing dish to dry. The abrasive pads were not transferred to the filtering funnels, but instead were repeatedly rinsed into the funnels, to dislodge any dust particles. Then, the Whatman filter paper was thoroughly rinsed to wash soluble salts into the volumetric flask. After rinsing, the Whatman filter and the insoluble filtrate, without the abrasive pad, was set aside to dry.

The different treatment of the fiber filters and abrasive pads was done because of the differing compositions of each. The filters are almost entirely organic material (polyester fibers), and do not contribute much to the mineral content of the sample. Hence, ashing them with the Whatman filter paper has little effect on the blank values for the elemental analysis. Moreover, the porosity in the filters is fine enough that some dust was probably enmeshed in the fibers and not rinsed out. However, the abrasive pad is largely comprised of alumina, and retaining and ashing the pad would result in a huge background relative to the small amount of dust present. Moreover, because of the coarse porosity, it is likely that all dust was readily rinsed from the pad. Disposing of the pad after thorough rinsing top dislodge the dust was unlikely to result in any significant loss of dust components.

Soluble salts—After filtering, the filter effluents were brought to 25 ml in the volumetric flasks. This volume was then subdivided into separate aliquots for anion and cation analysis. Five ml was extracted, acidified to 2% HNO_3 with Optima grade acid, and then diluted to 10 ml and spiked with 1 µg/ml Sc as an internal standard for cation analysis by inductively coupled plasma optical emission spectroscopy (ICP-OES). Cationic analytes included Na^+, K^+, Ca^{+2}, and Mg^{+2}. Eight ml was retained for anion analysis by ion chromatography (IC). Anionic analytes were F^-, Cl^-, Br^-, NO_2^-, NO_3^-, SO_4^{-2}, and PO_4^{-3}. The remainder was acidified to 0.1% HNO_3, and retained for ammonium analysis by cation IC.

Insoluble minerals—After drying, the Whatman paper filters (and the fiber filters, for the filter samples) were transferred to platinum beakers and ashed at 500ºC for one hour. Then, 5 ml Optima grade HF and 2 ml Optima-grade HNO_3 were added to each crucible and the crucibles were placed on a hot plate. The samples were taken to dryness, and then redissolved in 500 µL of trace-metal grade HCl, to convert hard-to-dissolve fluorides into chlorides. The samples were taken to dryness, and the HCl treatment repeated. Finally, the dried samples were taken up in 2% HNO_3 and quantitatively transferred to 15 ml sample tubes, the crucibles being rinsed several times to ensure complete transfer. The sample mass was brought up to 10 grams with 2% HNO_3 (mass was used instead of volume because of the small sample sizes). For analysis, the samples were spiked with 1 µg/ml Sc as an internal standard, and analyzed by ICP-OES. Whole-rock analytes included Na, K, Ca, Mg, Fe, and Al. Because silica was lost as silicon tetrafluoride when the sample was dissolved, it could not be measured directly. Instead, silica was calculated using the calcium concentrations in the dust, determined by the wet chemical methods (soluble + insoluble fractions), and the Ca/Si ratios measured by XRF.

ICP-OES analyses were done using a sequential Perkin-Elmer Optima 8000 ICP-OES, in both axial and radial viewing modes. A minimum of two wavelengths were evaluated for each element; collected spectra were evaluated for interfering peaks, and for each element, the wavelength was chosen that best reproduced known standard concentrations when the standards were analyzed as unknowns. Concentrations were estimated using integrated peak areas. Five to six standards, made by diluting Spex Certiprep® Assurance and Claritas-Grade ICP stock standard solutions, were used because the range of the sample concentrations was unknown. Sample concentrations were estimated using a subset of the standards (never less than three and a blank), excluding those which were higher than necessary to constrain the sample concentration. This was done because the calibration curves were based on the least squares method, which over-weights higher-concentration standards and results in larger errors for values in the lower part of the range.

IC analyses were done with a Dionex ICS-1100 RFIC Ion chromatograph with a Dionex Ionpac AS-23 RFIC column and AG-23 guard column, and a Dionex AERS 500 suppressor. As with the ICP analyses, a subset of standards (never less than three and a blank) were used when calculating sample concentrations, to minimize overweighting of the higher standards. The standards were made by dilution of stock Dionex IC anion standards.

For both ICP-OES and IC analyses, a blank of the Whatman paper filter was also analyzed, and reported sample concentrations were corrected for contributions if any, from the paper filter; contributions to chloride and nitrate were observed, possibly due to absorption of hydrochloric and nitric acids from the laboratory environment.

2.3.2   Results

Analysis results are presented by method, for each sample. Mineralogical and textural information is provided first, and chemical analyses are provided last, utilizing the mineralogical results to interpret the chemical data.

2.3.2.1   SEM/EDS Analysis

Filter blank

The filters consist of relatively fine polyester fibers, compressed to produce a thick (~2mm filter). The fine fibers made imaging and element mapping on the filters difficult—despite the gold coating, the fibers tended to charge in the electron beam, and to shift or vibrate during imaging; this effect was worse at higher magnifications. Moreover, fibers deeper in the filter were poorly coated, and charged strongly, producing blurring and streaks in the SEM images. While the filters are not the optimal substrates for dust analysis, reasonable photos were obtained. The filter blanks were largely clean, showing little contamination by particulates (Figure 6). The polyester fibers are 10-20 µm in diameter, and are not

bound with a resin. The few particles present were large (tens of microns in diameter), and easily differentiated from the fine dust particles observed on the filters actually used in dust sampling.
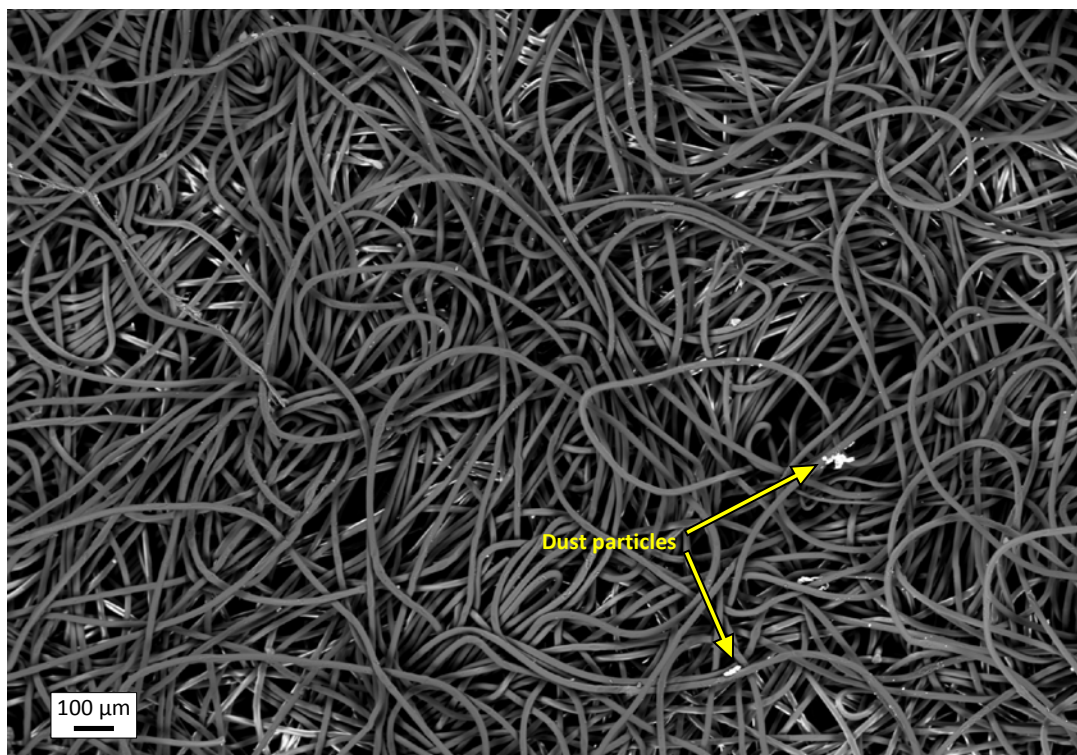
Figure 6. SEM electron backscatter detector (BSD) image of filter blank. The filter consists of polyester fibers, with no binder. The blank has rare dust particles adhering to the fibers.

Abrasive pad blank.

Figure 7 is a BSD image of the Scotch-brite© pad blank. The abrasive pads consist of 30-50 µm nylon fibers and angular grains of alumina 200-400 µm in diameter. The fibers and abrasive are bound together with voluminous amounts of resin. The coarse fibers and large abrasive grains provide good, broad substrates for dust particles, and are coarse enough to resist movement due to charging in the electron beam, providing a stable surface for imaging and analysis of dust particles. The blank abrasive pad sample was relatively clean, but tiny particles were readily visible on the fibers. These appeared to be mostly titania, which is listed as a trace ingredient in the pads. Titanium is more concentrated in the white letters and numbers that were stenciled onto the back of the pads; the pigment in the paint was apparently titanium oxide.

Both the pads and the filters are organic material, making analysis of organic components in the dust difficult. Moreover, carbonates cannot readily be distinguished. In addition, the alumina in the abrasive pads generates high background aluminum concentrations, potentially interfering with identification of aluminosilicates (e.g. clay minerals) in the samples. A collection substrate allowing identification of carbonates would be preferred, as carbonates are a common component of atmospheric aerosols; however, an appropriate alternative has not been identified.
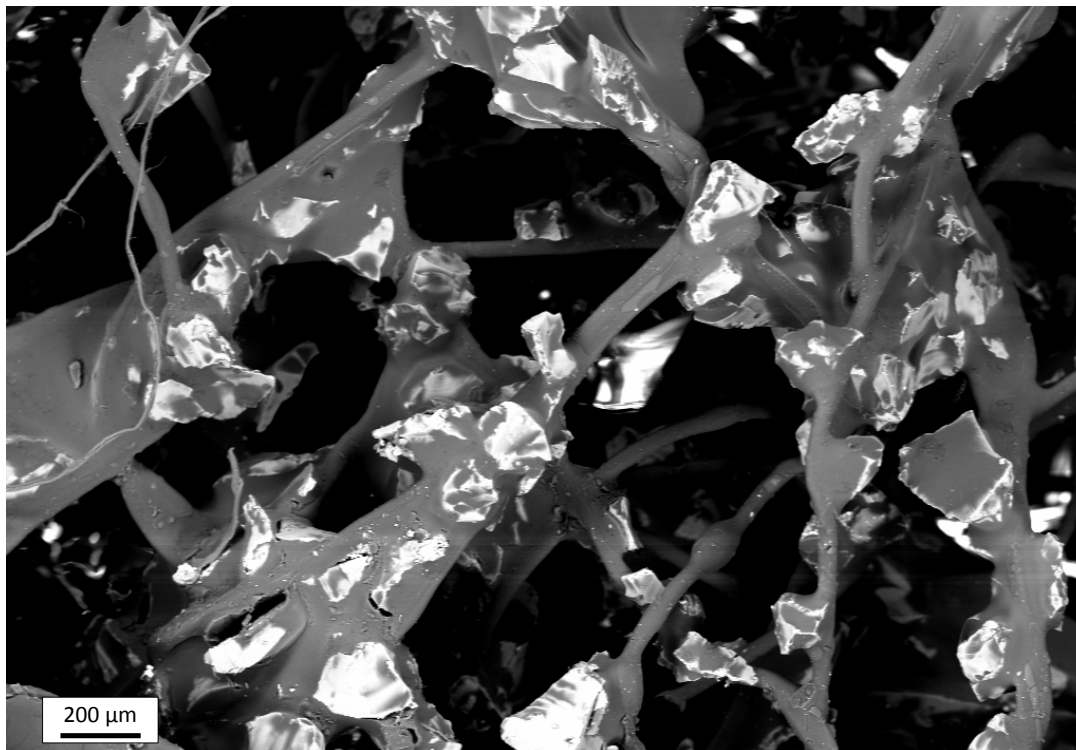
Figure 7. SEM backscattered electron image of the Scotchbrite pad blank, illustrating the presence of the abrasive particles within a polymeric matrix.

EPRI #1 Filter.

As noted previously (Figure 5), The EPRI #1 filter sample was discolored, indicating a relatively high dust load had been captured. SEM imaging confirmed that dust was on the filter, and showed that the trapped material was largely bimodal in size. Figure 8A and Figure 8B are BSD images of a typical region of the filter. Large particles, 20-40 µm across, are trapped between the polyester fibers of the filter and fall into two categories. Most appear to be biological materials such as pollen and plant fibers (at least 10 pollen grains are in this image); but composite mineral grains, clusters of minerals possibly cemented together with salts are also present. Smaller particles, less than ~5 µm in diameter, adhere to the surface of the fibers. The smaller particles are generally angular, and analysis shows that they are dominantly inorganic materials—salts and other minerals.

Higher magnification views of the some of the coarser materials are shown in Figure 9. Figure 9A is a bilobate pollen grain; Figure 9B shows a cluster of desiccated pollen grains; Figure 9C is a possible fragment of fungal material; and Figure 9D shows three pollen grains with a large composite mineral grain. The SEM survey suggests that the majority of the material on Filter #1 is pollen; this was confirmed by other analyses, as discussed later.
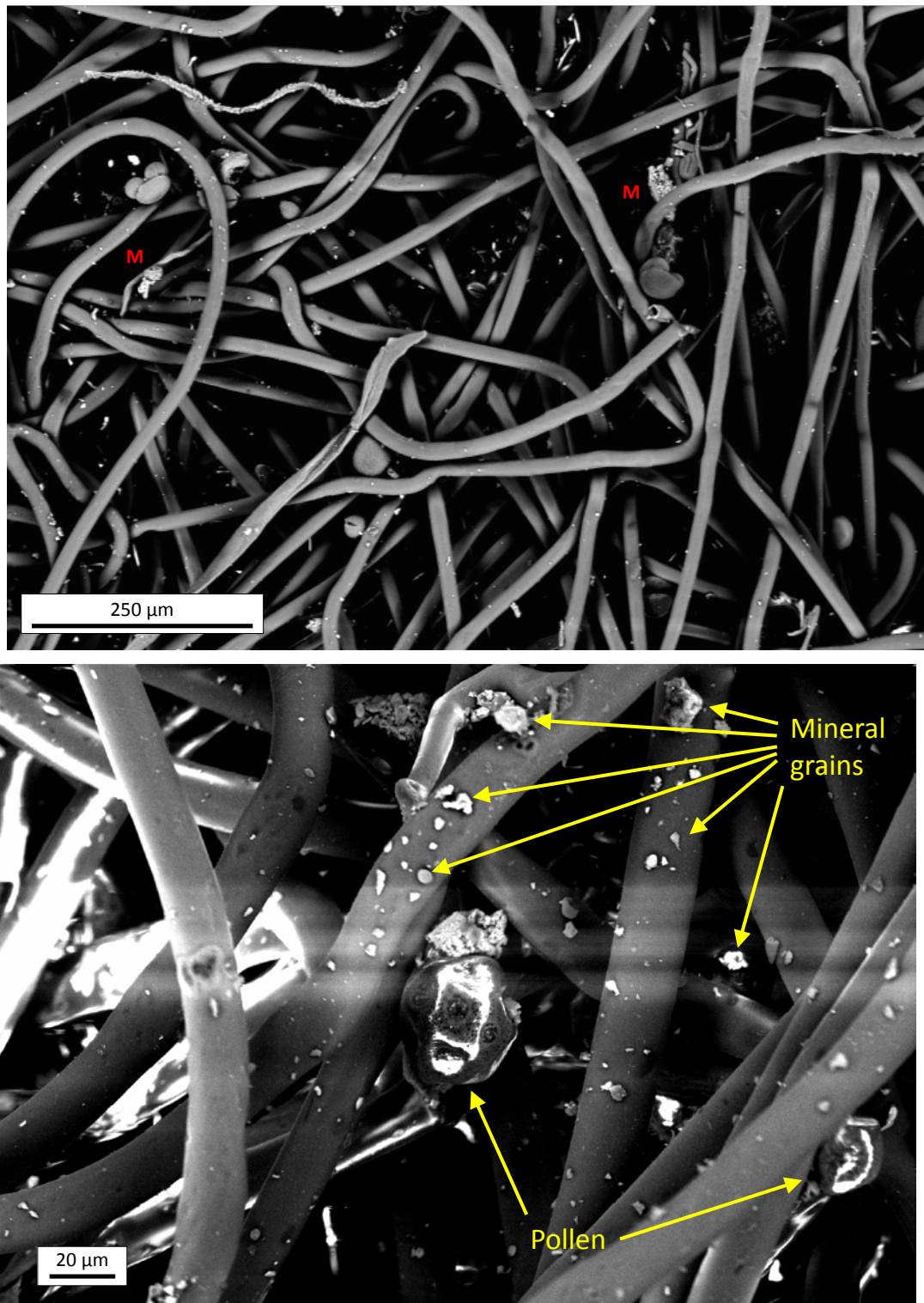
Figure 8. SEM BSD images of EPRI filter #1. A) Low magnification view, showing coarser particles—plant material and composite mineral grains (M)—trapped between filter fibers. B) High magnification view, showing fine dust particles, mostly mineral grains, adhering to the fiber surfaces (blurring and burned-out regions are charging effects).
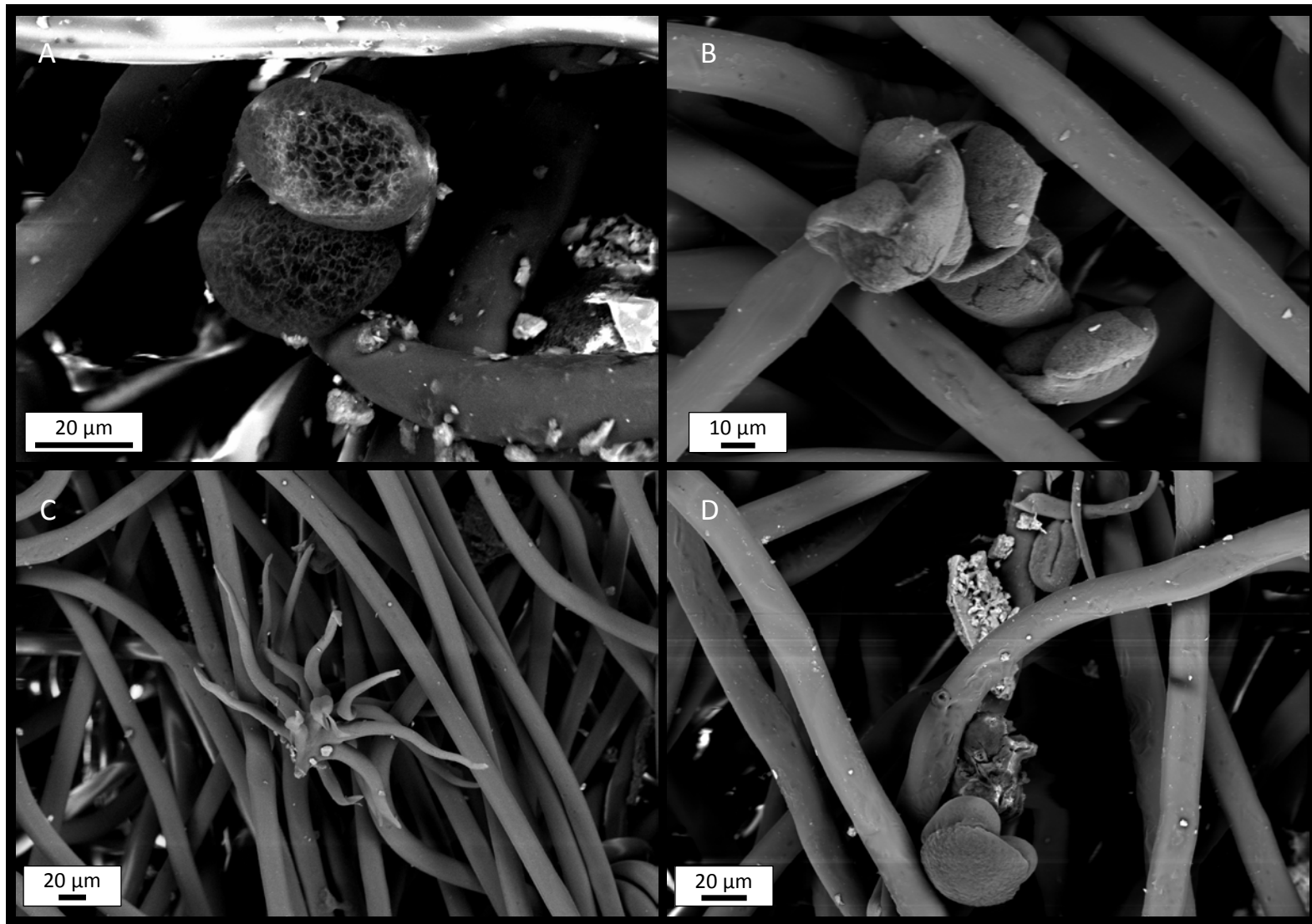
Figure 9. SEM BSD images of coarse particles, mostly biological materials, trapped on EPRI filter #1. A-B) Pollen grains; C) fungal material(?); and D), pollen and a coarse composite mineral grain.

Identification of the mineral phases present, especially the salts, is the primary goal of this study. To do this, the filters and pads were imaged by SEM, and then element maps were collected using the EDS system on the SEM. These maps provide mineralogical information by showing correlations between element locations, and also provide some estimate of relative element abundances. However, it is important to remember that they provide information only locally, because only a tiny fraction of the filter or pad is being imaged; the mapped area may not be representative of the sample as a whole. In some cases, maps are included here because they show features of interest, rather than because they are representative of the filter as a whole.

Figure 10 shows the image, EDS spectrum, and EDS element maps for a region on EPRI filter #1. To interpret element maps, some discussion is necessary. Element maps show the distribution of individual elements within the imaged area, with the brightness of each pixel correlating to the abundance of that element relative to the abundance at other locations within the map. The contrast and brightness are adjusted for each map to span the range of counts received for that element over the mapped area. Therefore, similar brightnesses for different elements do not indicate similar concentrations. It is also important to note that parts of the image that are shadowed from the X-ray detector due to topography will appear dark on the maps. Figure 10 illustrates many of points. The carbon (C) and oxygen (O) maps are bright and smooth, showing the polyester fibers well, because the C and O count rate from the fibers was high. Shadows due to the high topography of the filters are clearly defined; although the composition did not vary in the shadowed and unshadowed regions, the count rate did. For most of the remaining elements, a few bright regions are present on a dark background, showing that mineral grains containing these elements are present. For potassium (K), the image is bright, but very grainy. This is because K count rates were very low across the mapped area, and contrast was greatly increased to show what minor enrichments were present. The brighter areas in the K map indicate that here is some weak enrichment in those areas. However, note, that the polyester fibers are visible in the K map. This is an artifact; there is no potassium in the fibers. Instead, they are visible because they create a slight increase in X-ray background, which is showing up on the K map due to the low total count range. The same is true, to a lesser degree, for magnesium (Mg) and nitrogen (N). A few grains are present that are somewhat enriched in these elements, but the faint images of the fibers are artifacts of the low total count range; there is no Mg or N in the fibers.

Figure 10 is included here in part because it is a good example of element maps and their limitations, but also because it contains a large grain of NaCl near the center of the image. NaCl is the only chloride phase observed in either EPRI #1 or EPRI #2, and it was not common in either case. A potassium aluminosilicates, possibly potassium feldspar, is present near the center of the image, and there is a general correlation of Si and Al. Few other correlations can be made at this scale, because the individual grains visible at this scale are generally composites. For instance, Figure 11 shows the spectrum and element maps for the single dust grain in the upper left center of Figure 10. As can been seen, this grain, several microns across, contains several different mineral species. The majority of the grain is calcium x, a significant fraction appears to be magnesium silicate, and an aluminum containing phase, possibly a clay, is present.

The large composite mineral grain from Figure 9D is shown in Figure 12. The grain appears to largely consist of a large Mg-Ca containing phase, possibly dolomite—the grain appears dark in the C map, but this may just be relative to the carbon-rich substrate. On the front surface of the Mg mineral are crystals of calcium sulfate, which have apparently lost water and desiccated, either in the electron beam, or on the hot waste package surface (see Figure 13). Other phases present include silica, a grain of potassium aluminosilicates (K-feldspar), and possibly a magnesium aluminosilicates phase. There is virtually no chloride present, and nitrogen is also very low.

Because of the charging effects, images were blurry, and dust particles would disengage from the surface of the fibers. Element maps of the Scotch-brite ® pads were more effective

Figure 10. SEM BSD photo, EDS spectrum, and element maps of EPRI filter #1, showing dust particles adhering to filter fibers.
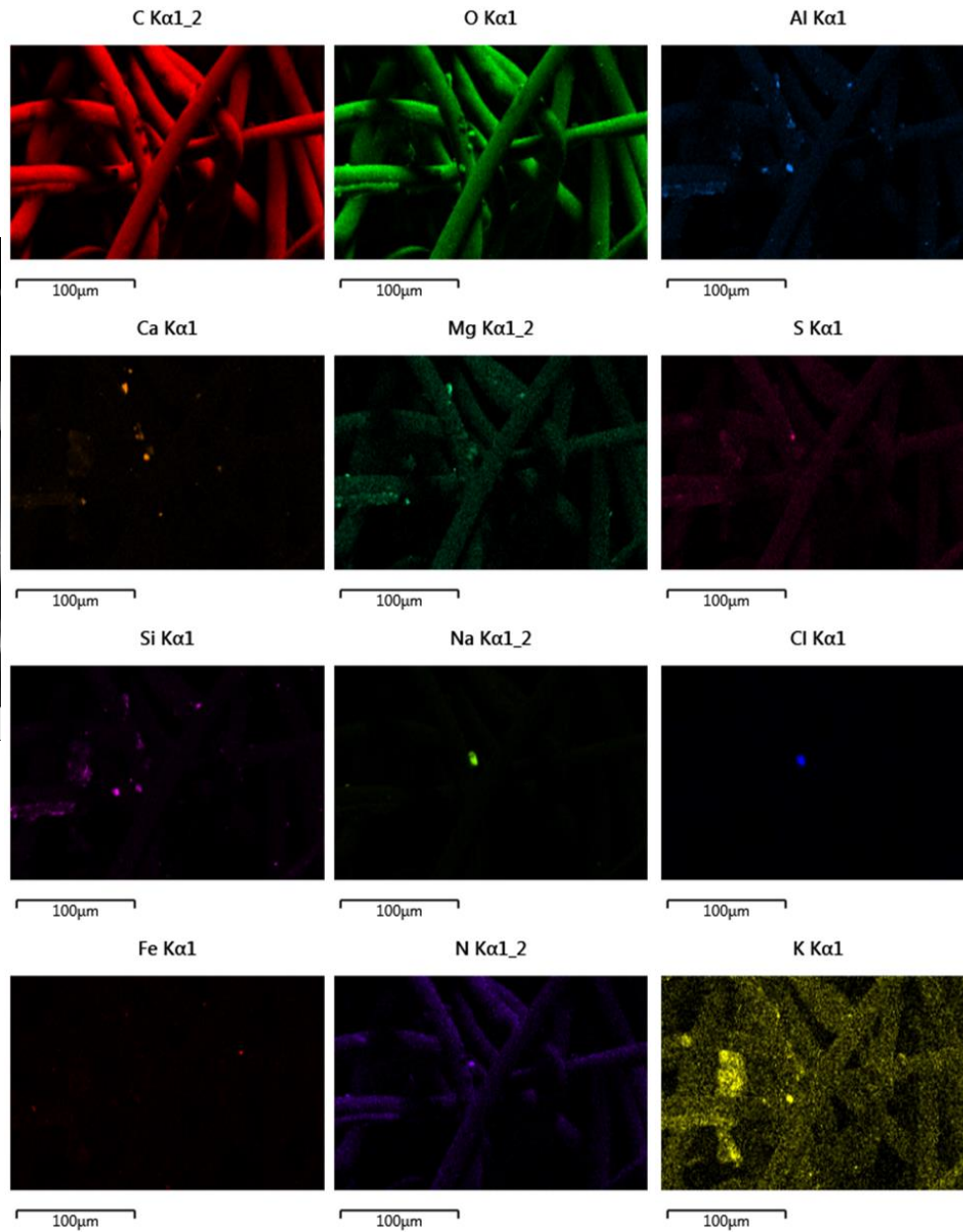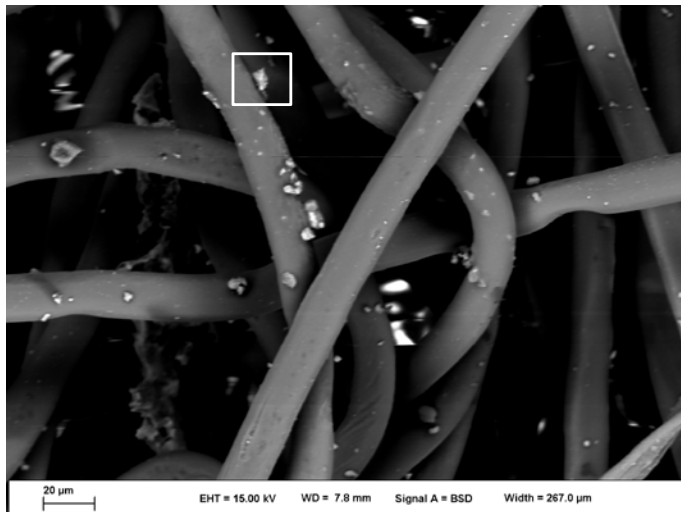
Figure 11. SEM BSD photo, EDS spectrum, and element maps of EPRI filter #1, showing close-up of multicomponent grain in Figure 10.
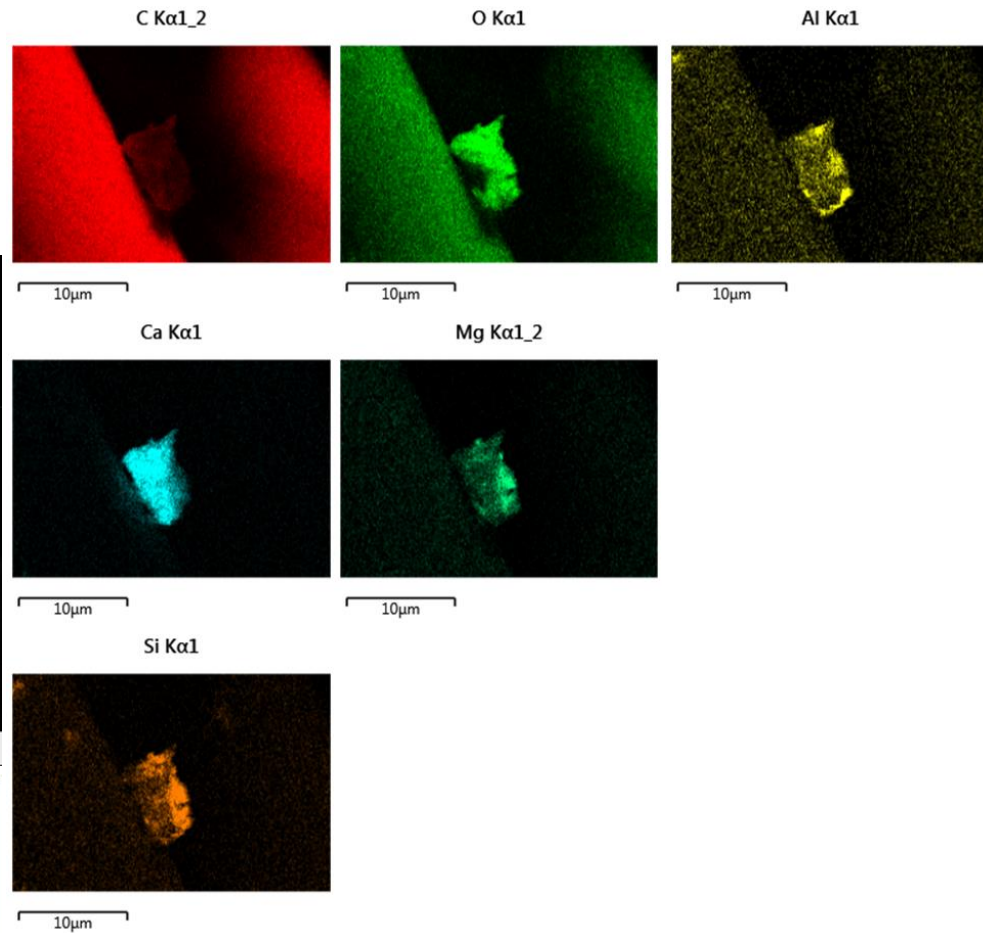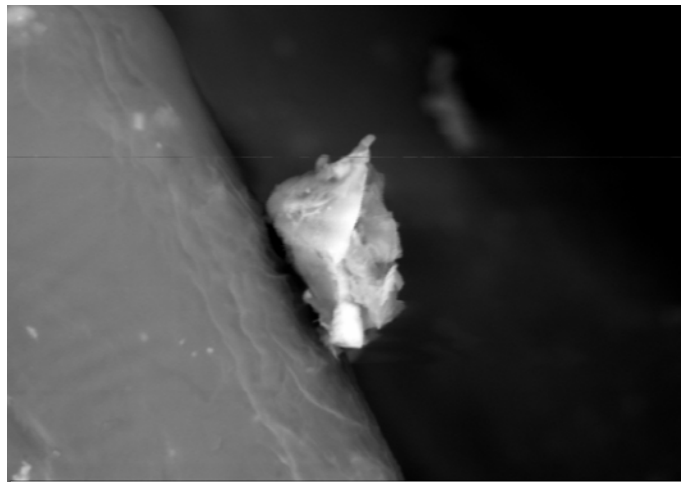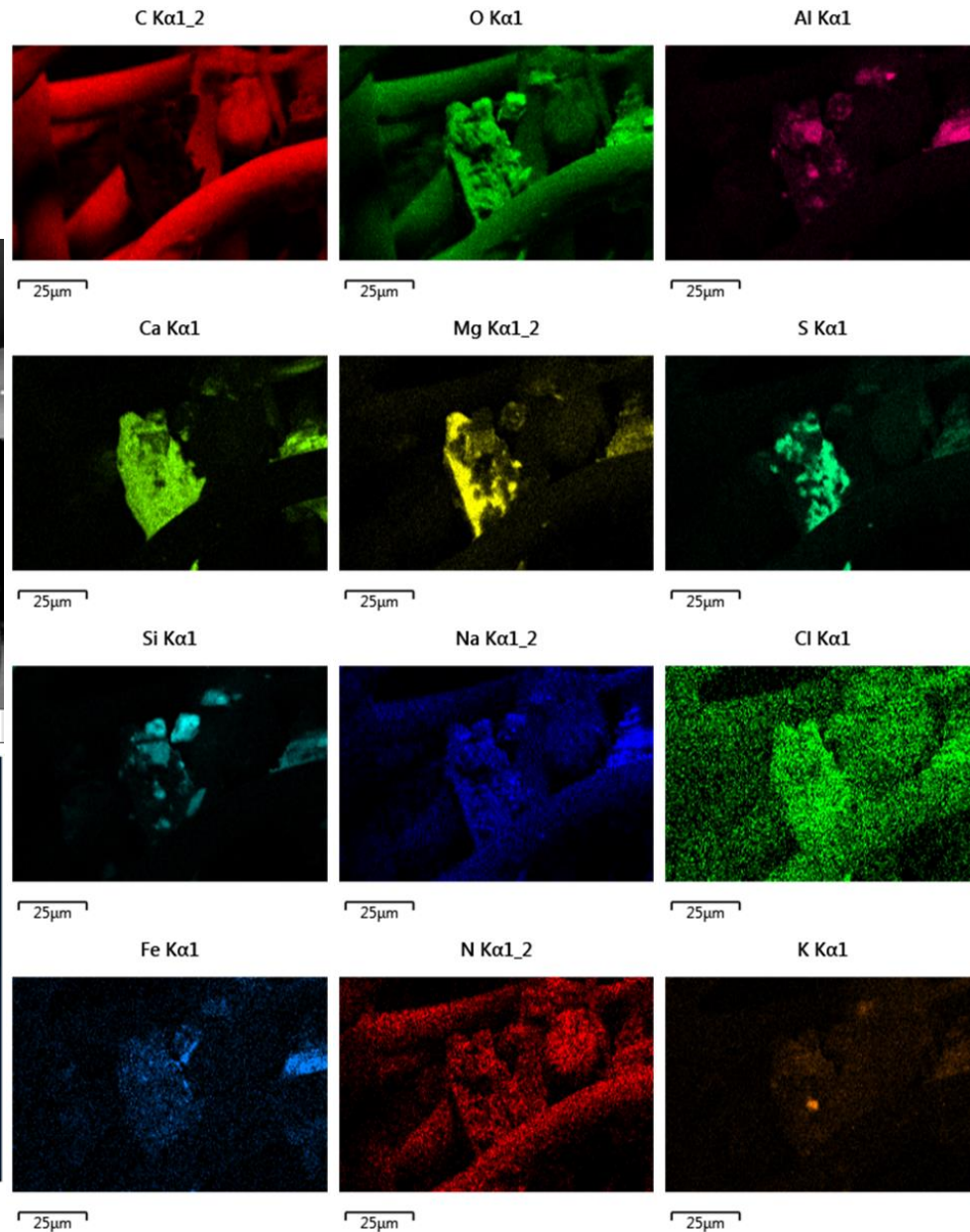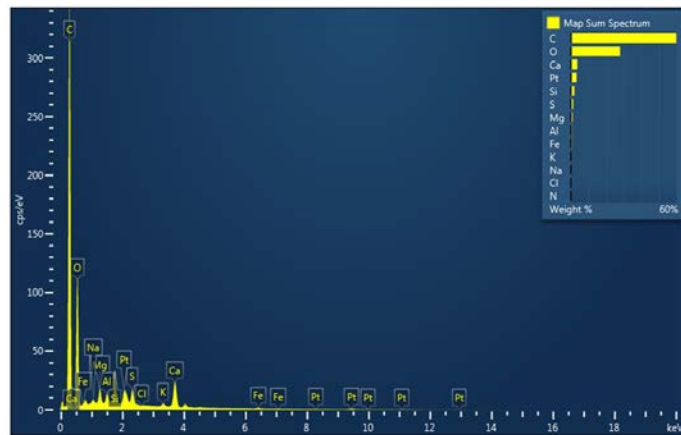
Figure 12. SEM BSD photo, EDS spectrum, and element maps of EPRI filter #1, showing close-up of the multicomponent mineral grain in Figure 9D (Note that pattern of fiber is beam damage).
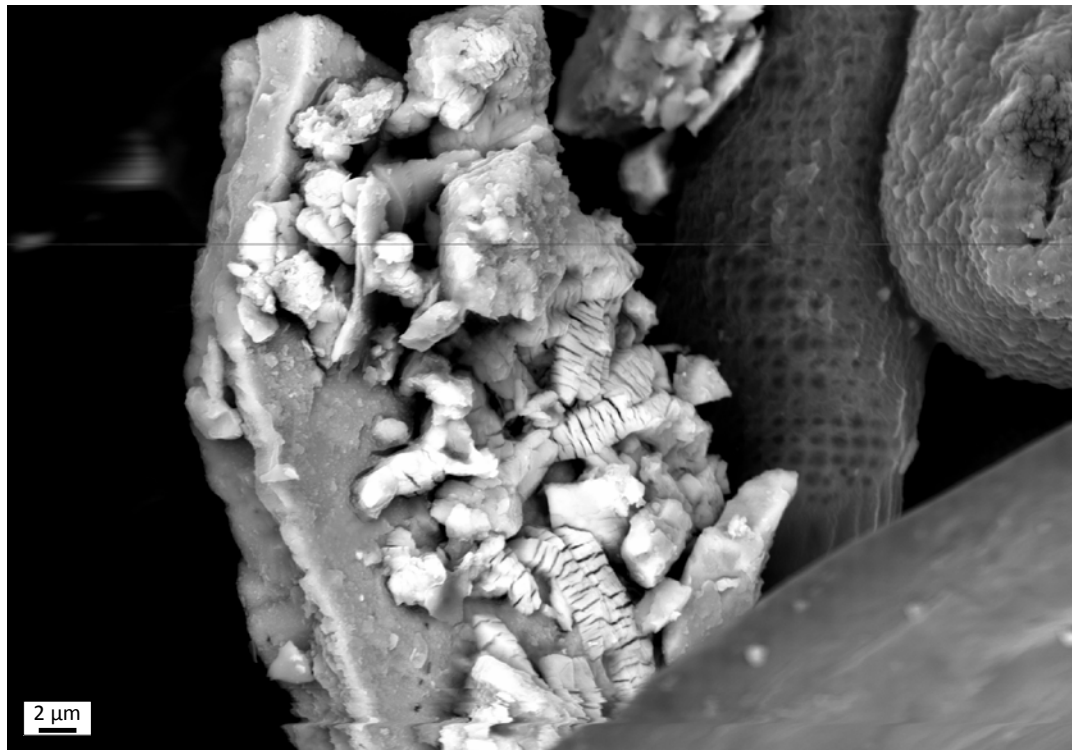
Figure 13. Composite mineral grain on EPRI filter #1. Magnesium-rich grain with desiccated Ca-sulfate crystals on the top, and associated aluminosilicate grains (Note that the pattern on the polyester fiber in the background is beam damage).

EPRI #1 Pad

SEM BSD images of a suite of materials found on the EPRI #1 pad are shown in Figure 14. In Figure 14A, a broken alumina abrasive particle is decorated with steel from the storage container, showing that there was sufficient pressure applied to the sampler to adequately remove materials from the container side. Figure 14B shows dust adhering to the broad resin surfaces of the spongy pad. Figure 14C shows two spherical particles, the largest of which appears to show skeletal textures suggesting quenching. The EDS shows that these particles are nearly pure iron—they are not oxides. They may be fly ash; alternatively they may be products of nearby welding operations. The latter seems unlikely, however, as other components of steel (chrome or nickel) are missing. These spherical objects were not uncommon on the pad surface. Figure 14D is an agglomeration of pollen fragments. Despite its abundance on the EPRI #1 filter, pollen was rare on the EPRI #1 pad; the coarse porosity the pad allowed the large pollen grains to be drawn through and deposited on the filter.

Figure 15 shows element maps for the dust on the surface of the pad. In the case of the pad, the resin surface appears to contain relatively little oxygen, but the alumina abrasive grains are rich in both aluminum and oxygen. It is possible to distinguish oxygen and aluminum in dust grains on the resin surface, but not on the alumina. The elements maps show that may of the grain contain silica, and in fact many do not show other elements, indicating that quartz is the likely constituent. Calcium and sulfur correlate in a few grains, suggesting calcium sulfate is present; however, in many instances, Ca does not correspond to other elements, indicating that it is also likely present as a carbonate. Magnesium and silicon co-locate in several instances, and magnesium and calcium, suggesting either detrital dolomite grains, or perhaps primary huntite. Potassium correlates with silica, and may be present dominantly as illite. Finally, two small grains of sodium chloride are present; no other chloride is visible.

The correlations for the major species present are illustrated by layering the element maps onto each other, using a different color for each element. Where elements coincide, the colors are blended to create an intermediate color. This is shown in Figure 16, using the element maps for Si, Ca, S, and Mg. Orange grains indicate the colocation of S (yellow) and Ca (red), red grains, Ca alone (probably calcium carbonate); purple grains, Mg (blue) and Ca (red); blue grains generally indicate Mg (blue) and Si (cyan)—Mg does not appear to occur alone, suggesting that a magnesium carbonate is not present.

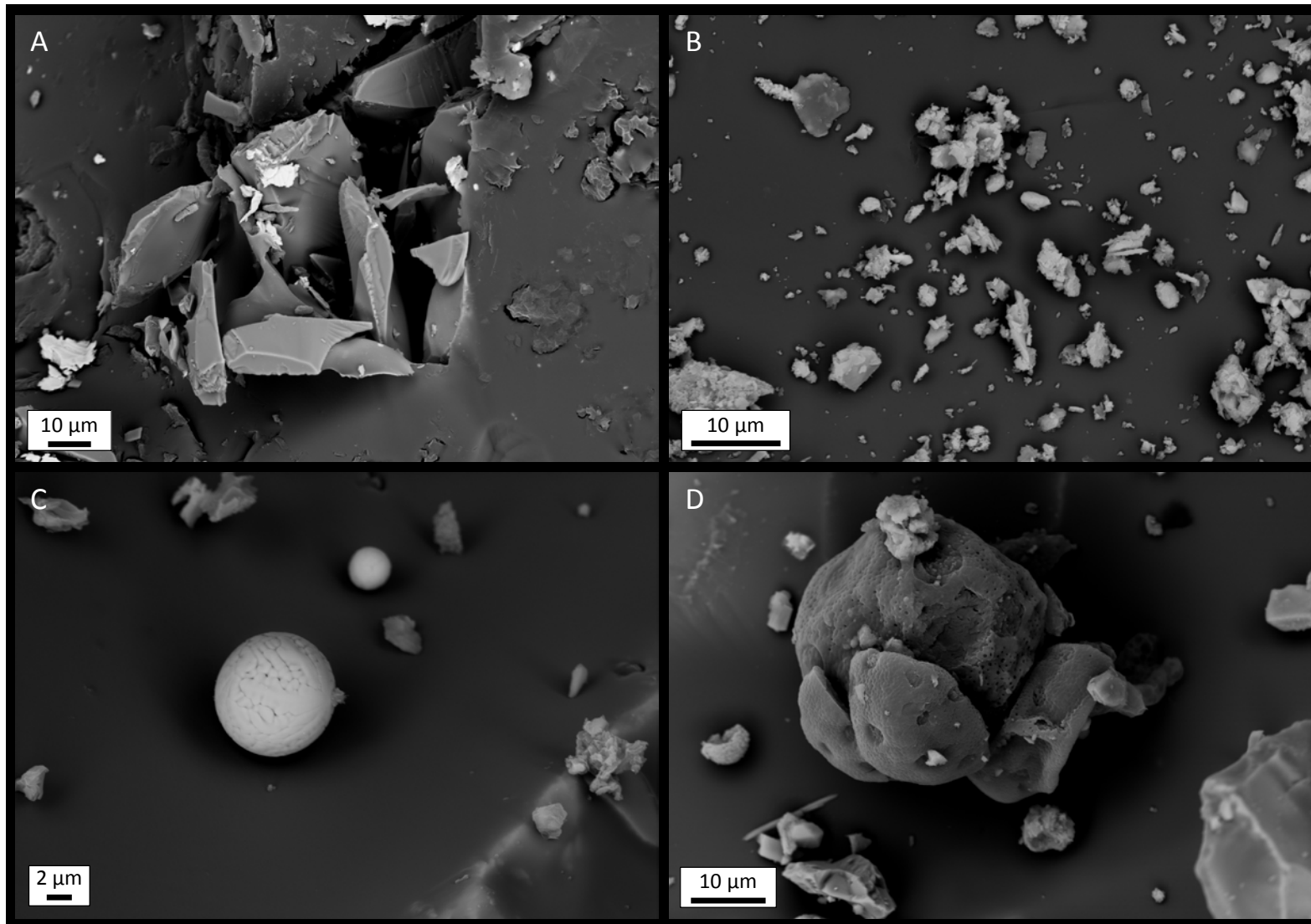Figure 14. SEM images of EPRI #1 Pad. A) Steel from the storage container adhering to a broken alumina grain; B) dust particles on the surface of the abrasive pad; C) iron spheres (fly ash?); D) pollen fragments on the pad.

Figure 15. SEM BSD photo, EDS spectrum, and element maps of EPRI pad #1.
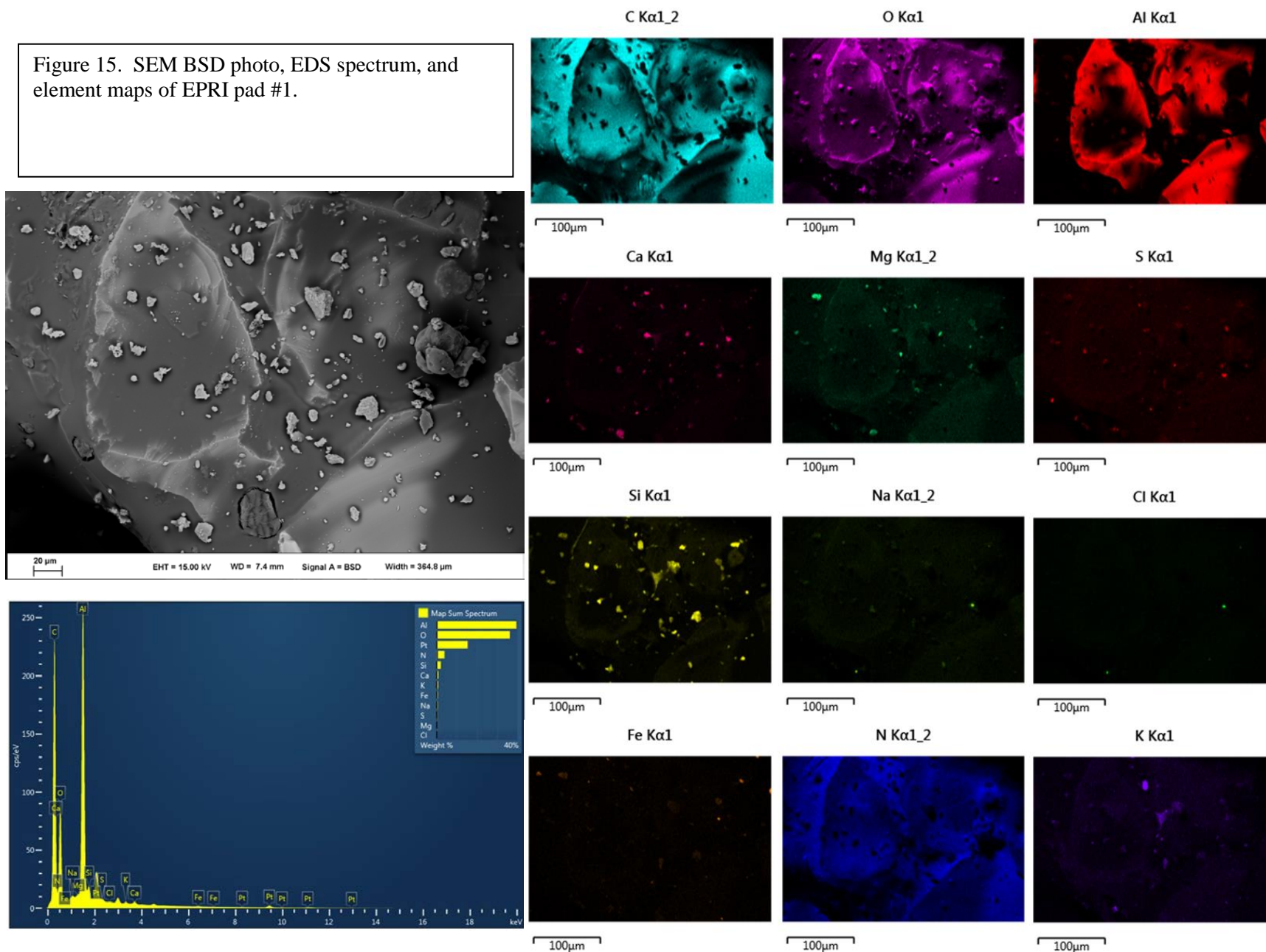
Figure 16. Layered image of dust on the surface of the EPRI #1 pad, using element maps for Si, Mg, S, and Ca.
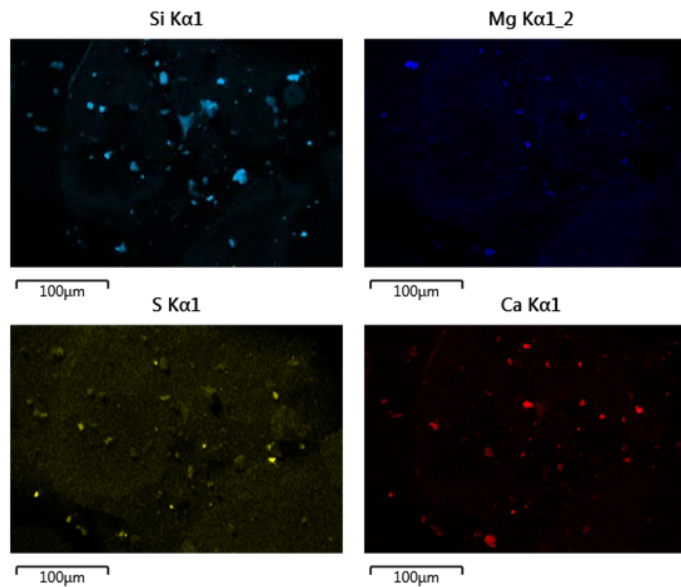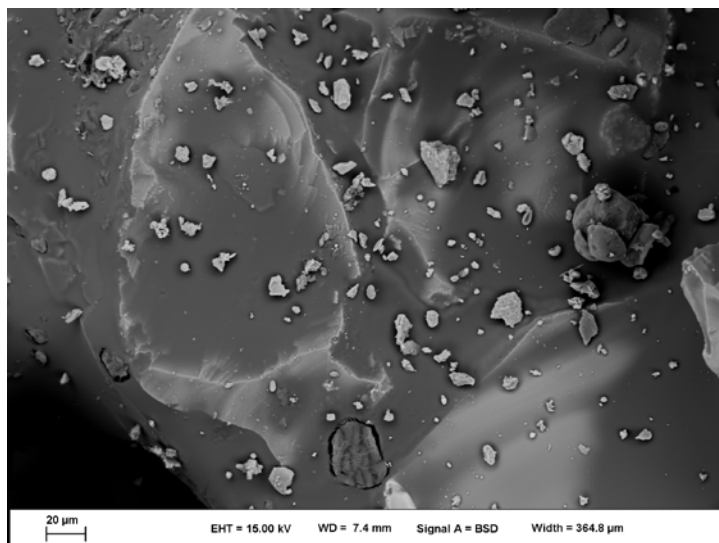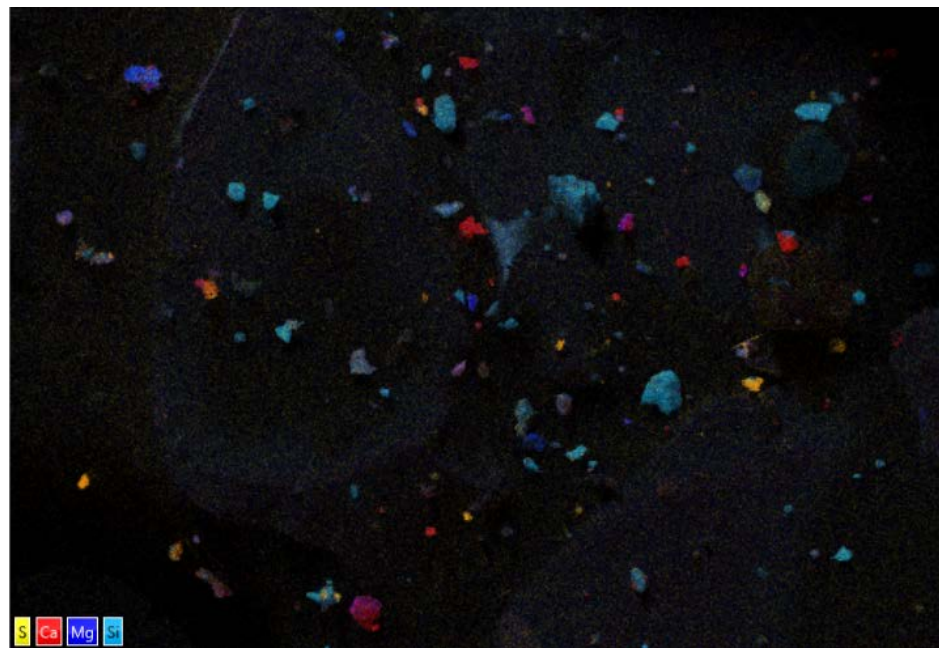
EPRI #4 Filter

Four typical images of the EPRI #4 filter are shown in Figure 17. Unlike the EPRI #1 filter, the #4 filter was not discolored with dust. SEM EBS images showed that it was not as heavily loaded with pollen as the #1 filter; however, it still had a significant quantity of finer inorganic dust particles. Element maps of the region shown in Figure 17A are given in Figure 18. The mineralogy is simpler than for EPRI #1, in that only a few mineral s appear to be present. Calcium and sulfur co-locate nearly exactly, suggesting that calcium sulfate is common. A few enrichments in Ca occur without sulfate, suggesting calcium carbonate is present. A single large potassium-rich grain is also rich in Si, O, and Al, suggesting it may be K-feldspar. The few remaining Si-rich grains do not correlate with any other element, and appear to be quartz. Sodium, potassium, and nitrate are virtually nonexistent.

A second region is shown in Figure 19. Once again, S co-loocates with calcium nearly perfectly, suggesting that the majority of sulfate present is as calcium sulfate. However, Ca and S co-locate well, indicating the common occurrence of calcium sulfate. Magnesium occurs both with Ca (dolomite?) and with aluminum and silica, possibly a clay phase. A grain of sodium alumino-silicate (possibly albite) is present, and a single grain each of NaCl and KCl. This is the only example of a chloride other than NaCl that was observed.

In both of these examples, calcium sulfate is the dominant salt present. Calcium carbonate also occurs, and alkali feldspars. Chloride salts are rare, and are mostly halite, NaCl.
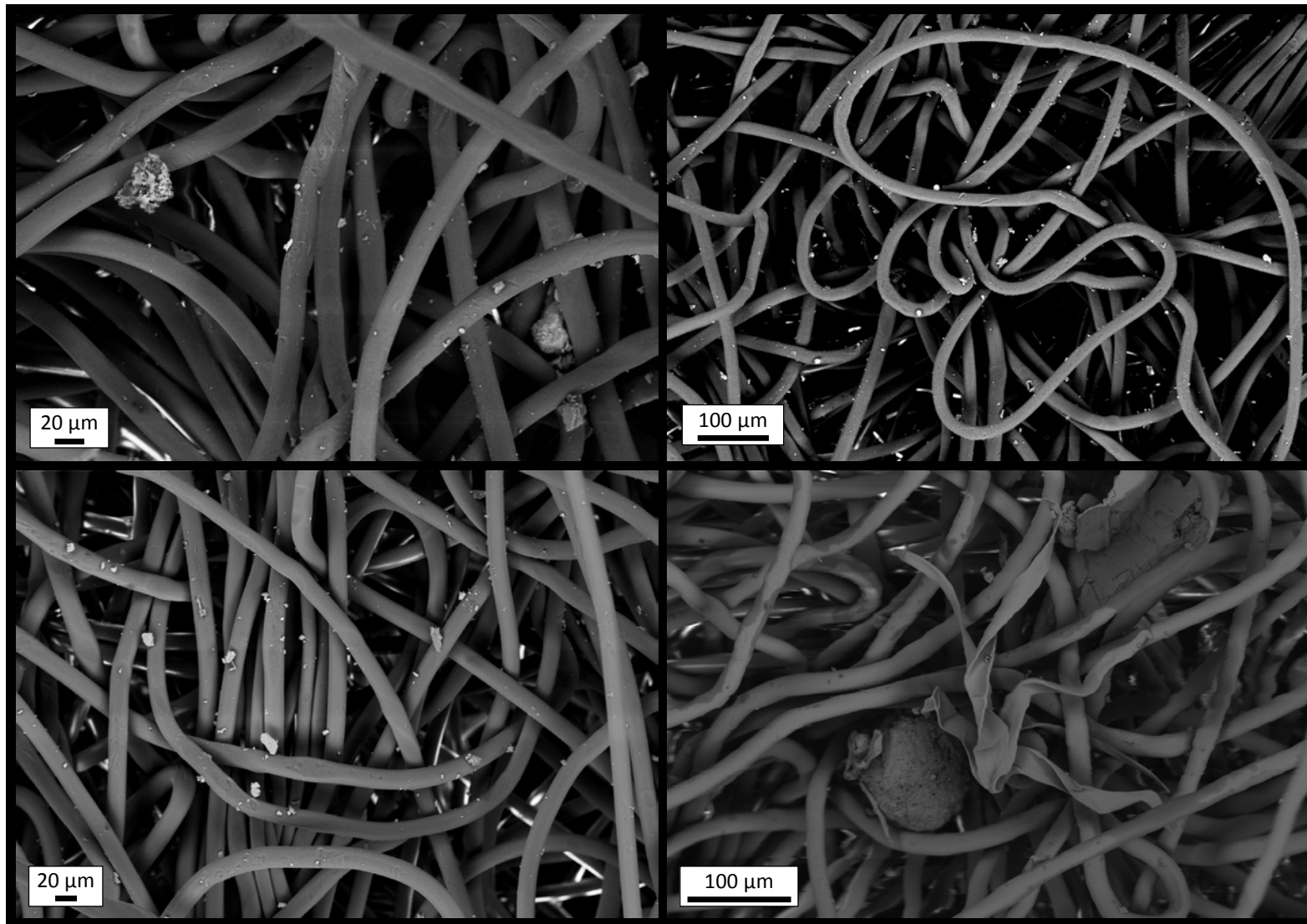
Figure 17. SEM BSD images of EPRI filter #4. A) isolated dust on the filter fibers, and a few large composite grains; B-C) isolated dust on the filter fibers; D) Composite mineral grain (analysis EDS showed it to be primarily calcium sulfate)and organic detritus.

Figure 18. SEM BSD photo, EDS spectrum, and element maps of EPRI filter #4.
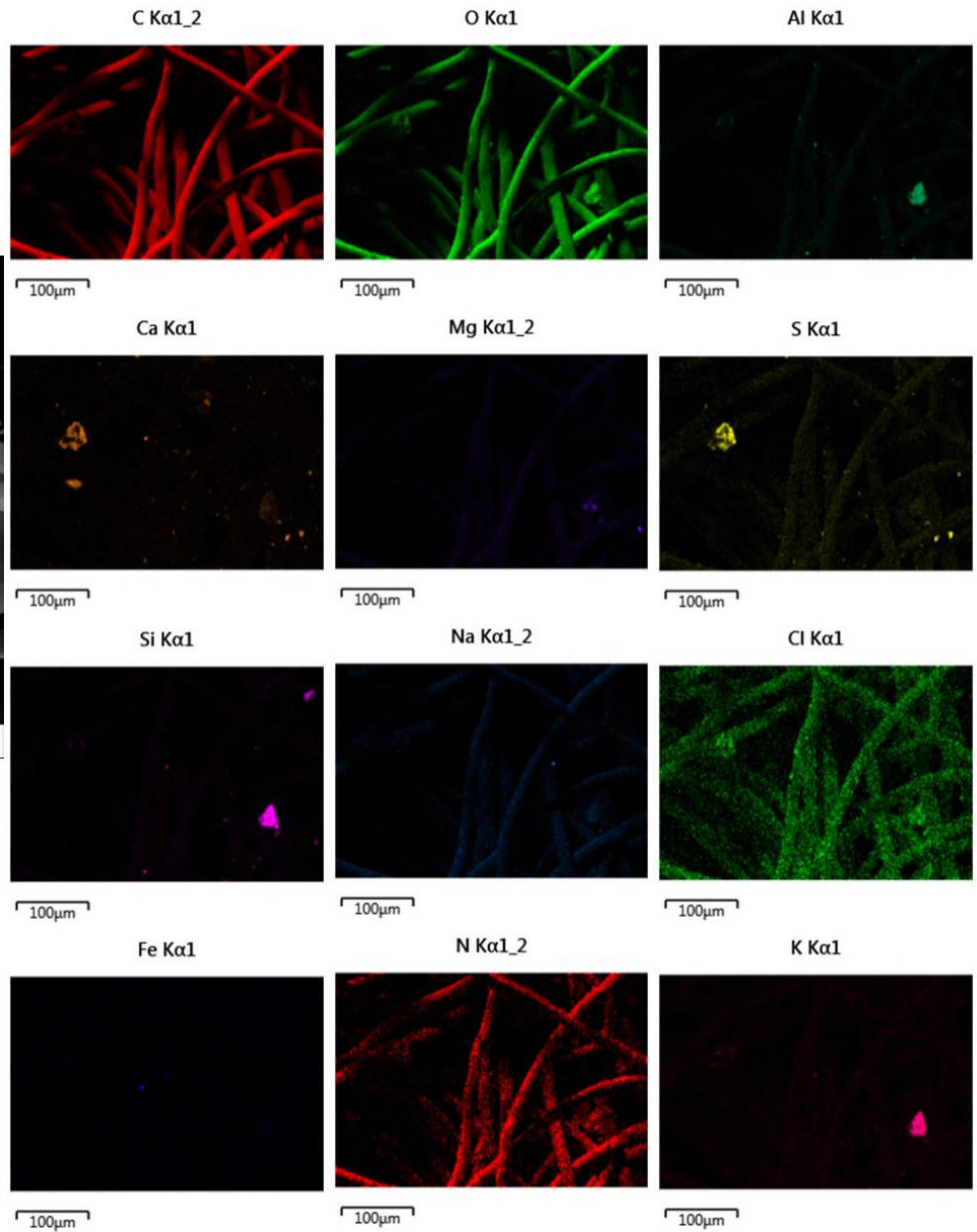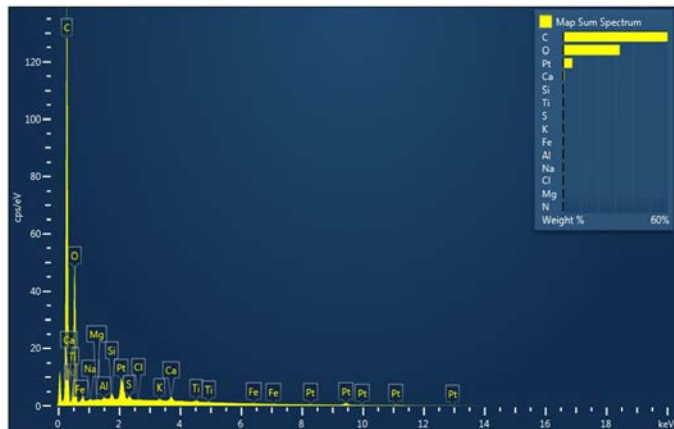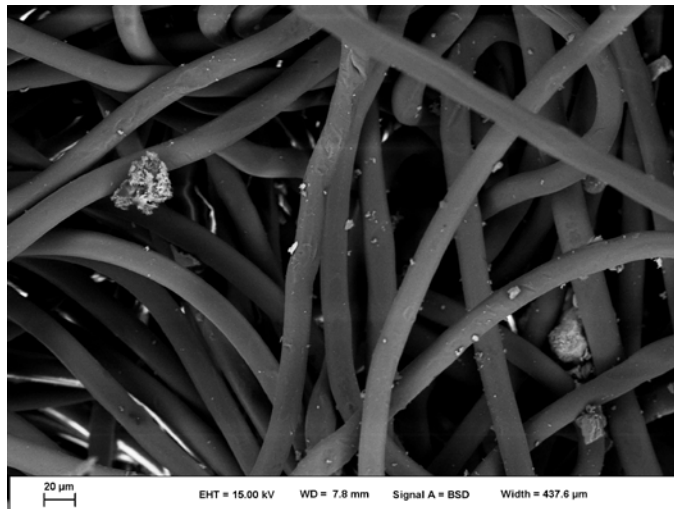
Figure 19. SEM BSD photo, EDS spectrum, and element maps of EPRI filter #4, region 2.
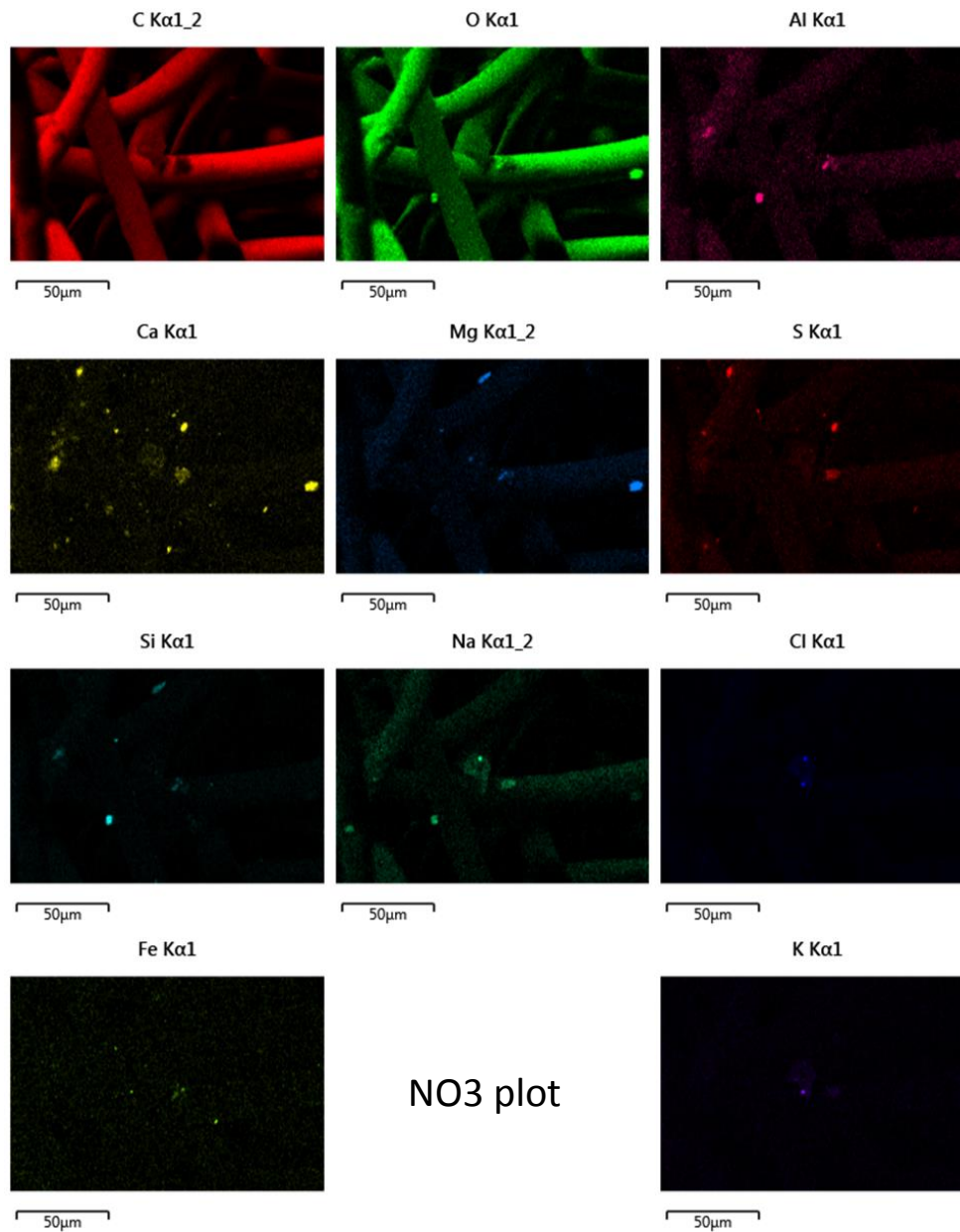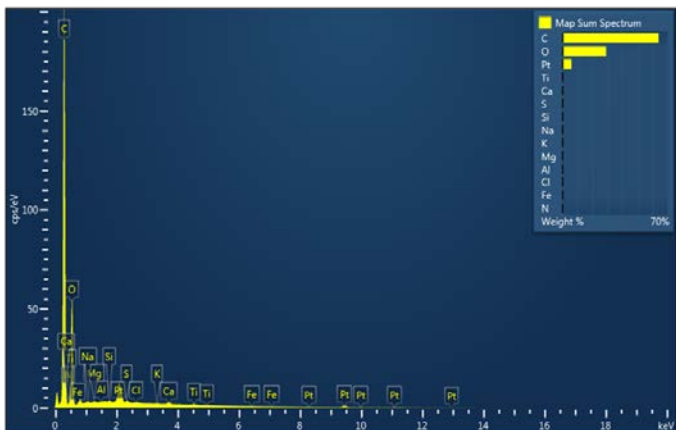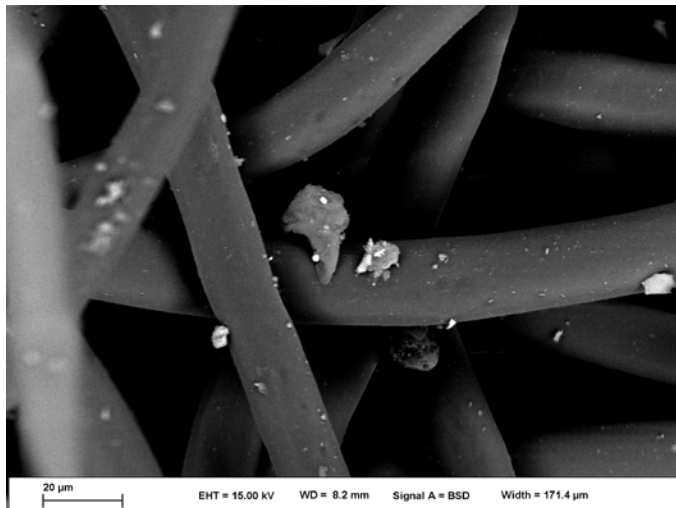
EPRI #4 Pad

Although the EPRI#4 filter was only slightly discolored, the #4 pad was very heavily loaded with fine, inorganic dust particles (Figure 20). It was apparently the lack of pollen that resulted in a lack of visible discoloration on the filter. Figure 21 and Figure 22 show element maps for the filter, and several dominant phases are apparent. Ca-sulfate is a common phase, as is quartz. Minor Na and K aluminosilicates are present, but the dominant aluminosilicate appears to be deficient in mono- and divalent cations—possibly kaolinite. Magnesium is present as a silicate, or possibly a magnesium-aluminum silicate. Chloride and sodium are nearly absent.
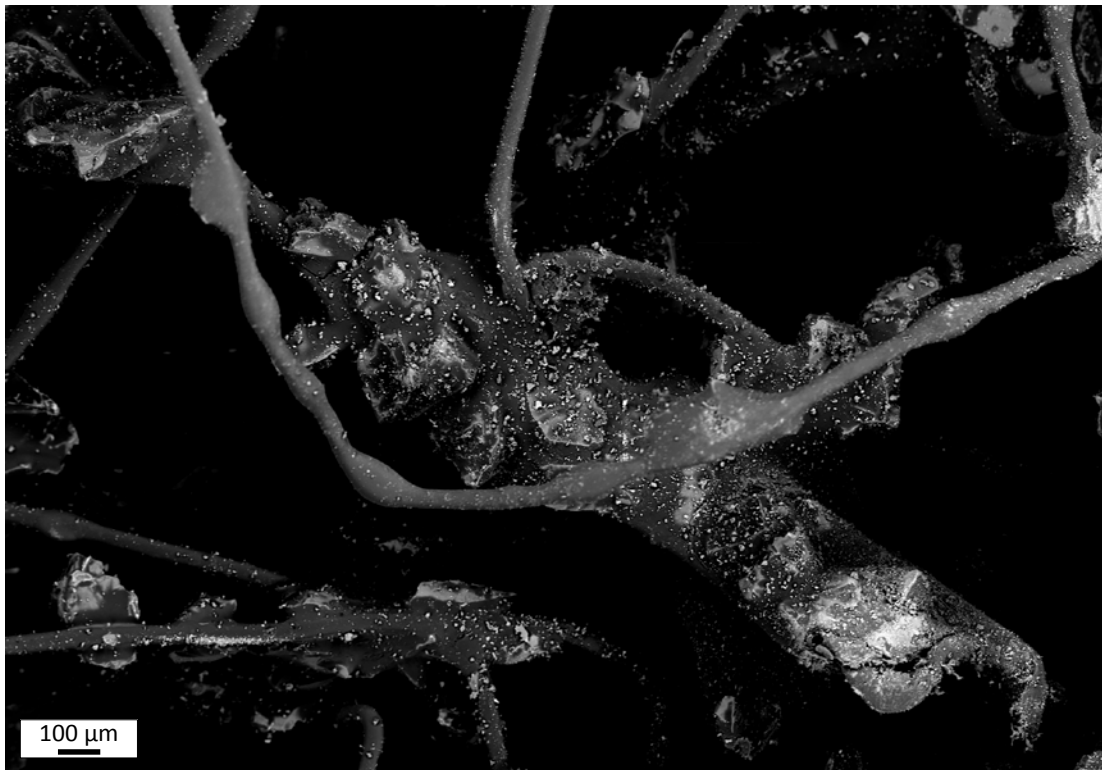
Figure 20. EPRI #4 abrasive pad, heavily coated with dust particles.

Figure 21. SEM BSD photo, EDS spectrum, and element maps of a region on EPRI #4 pad.
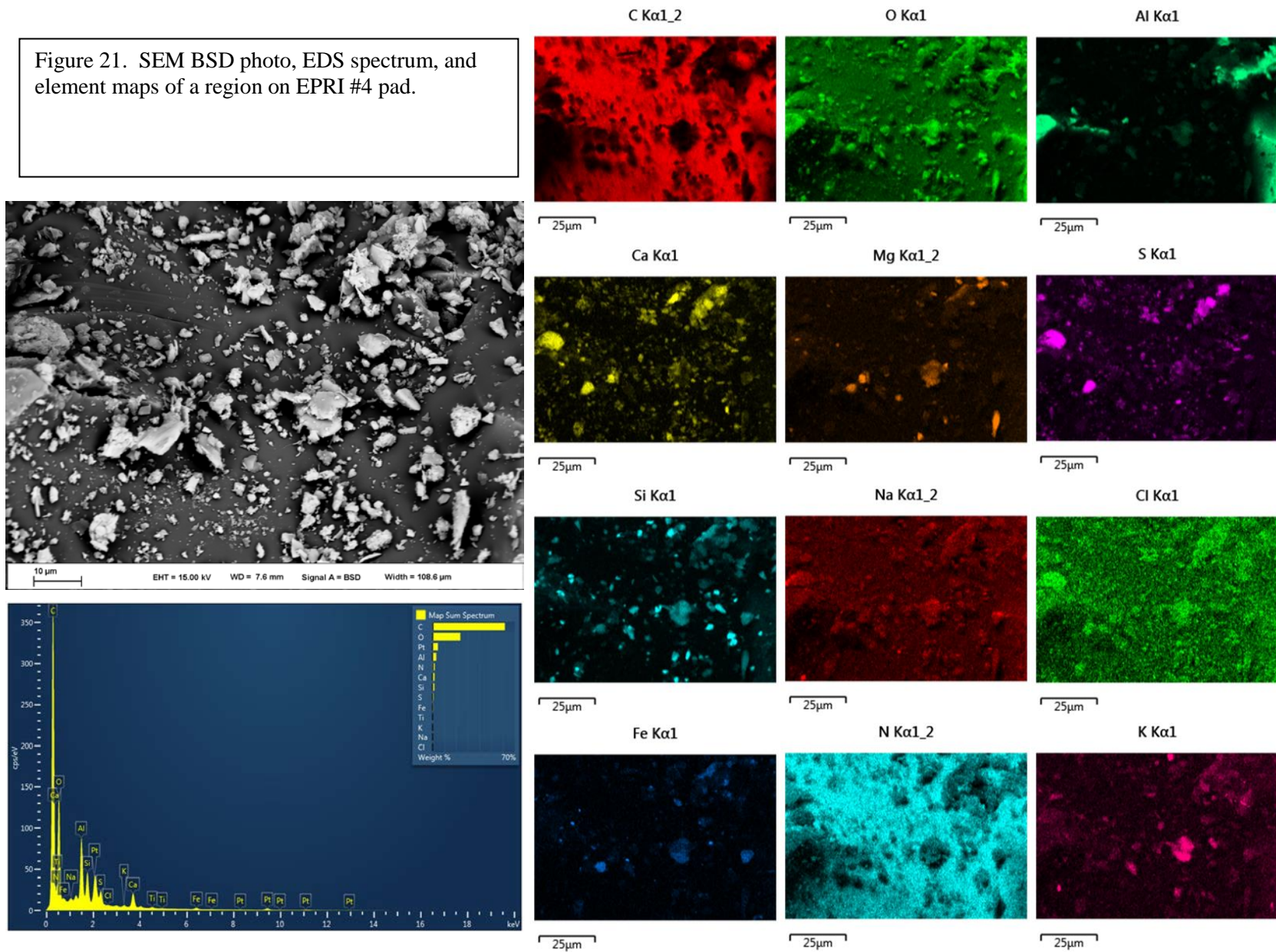
Figure 22. SEM BSD photo, EDS spectrum, and element maps of a second region on EPRI #4 pad.
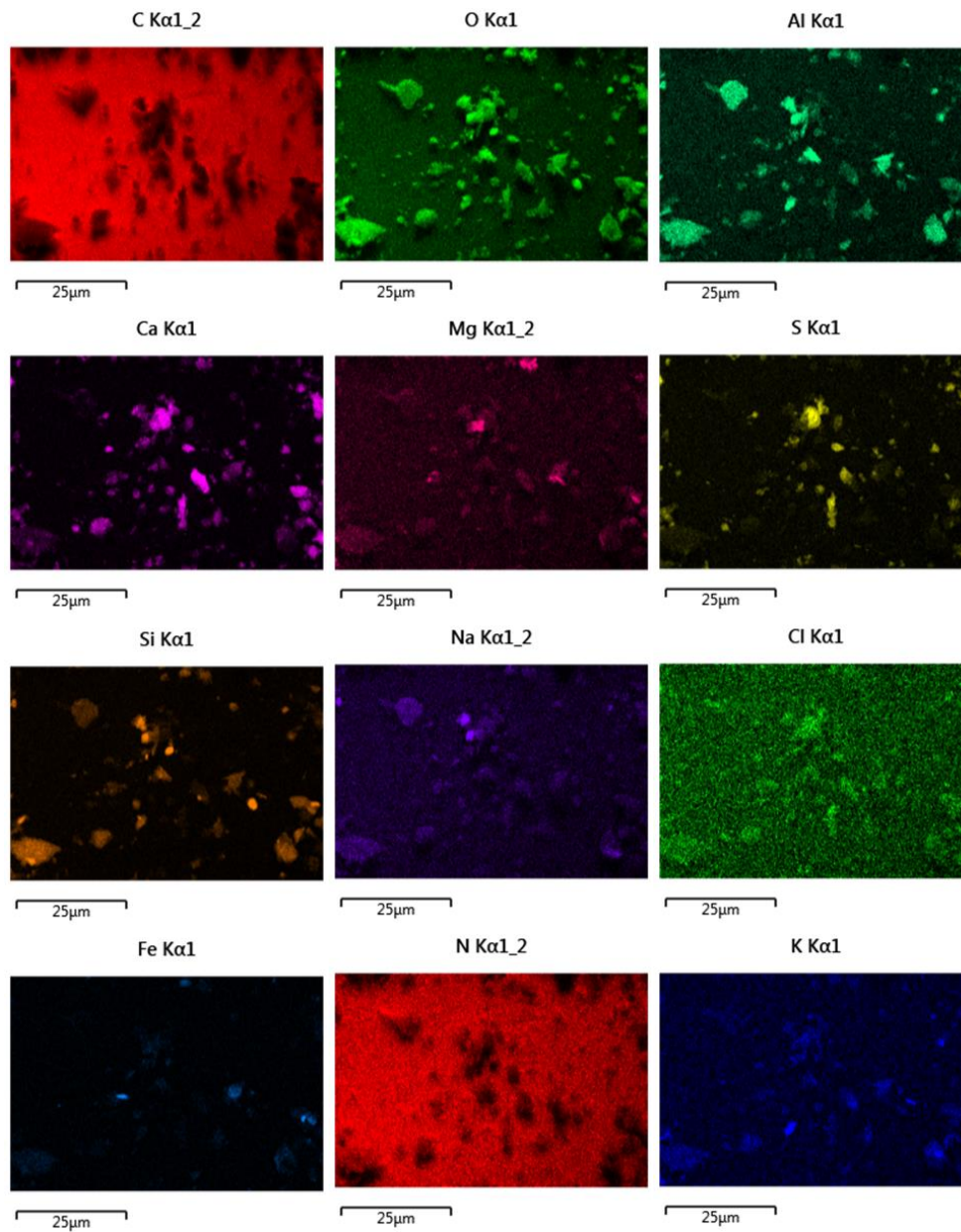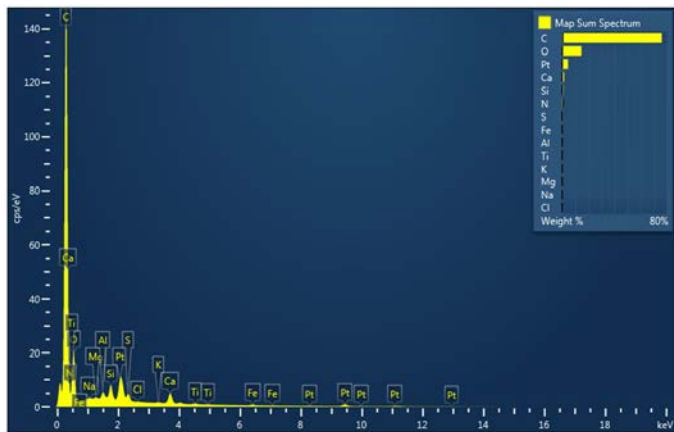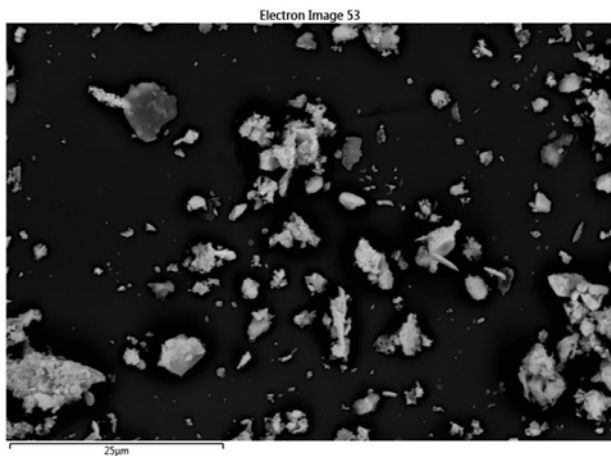
Summary

To summarize the SEM results, the abrasive pads are more amenable to SEM/EDs analyses than the filters, because they suffer from fewer charging effects. However, they pads and filters differ in their efficiency for capturing different sized particles, so both provide useful information. Larger particles pass readily through the porous pad, but are trapped by the fibers of the fibrous filter. Smaller particles collect on the broader regions of the abrasive pads, and are more easily imaged there.

SEM analyses show that the deposits on the EPRI #1 and EPRI#4 samples differ significantly. Pollen comprises a much larger fraction of the dust on the EPRI #1 filter and pad, and appears to be responsible for the strong discoloration on the EPRI #1 filter. The EPRI #4 filter was only slightly discolored, and entrapped much less pollen. However, inorganic particles were common on the #4 filter and coated the EPRI #4 sponge heavily.

SEM/EDS analyses indicate that calcium sulfate is the most common salt phase in the dust, especially on the filters and pads of sample #4. Although small amounts of halite (NaCl and possibly KCl in one case) arre present, chloride bearing phases are rare. No calcium or magnesium chlorides were observed. Calcium and Calcium/magnesium carbonates or hydroxides are present; the organic substrates make differentiating between these difficult, as carbon is not readily detected. However, carbonates seem most likely. Insoluble minerals are dominated by quartz, but alkali feldspars are also common, as are other unidentified alumino-silicate, possibly clays. Magnesium is commonly associated with these silicates.

One potentially useful tool that was not utilized here was EDS particle counting, which bins particles according to similar chemical compositions, allowing quantification of the number of each type of mineral present. This requires EDS mapping for long periods, and particle charging and dislodgement from the surface was a problem. However, additional efforts to implement this will be made, as it would provide an estimate of the modal mineralogy of the sample.

2.3.2.2   XRF Analysis

X-ray fluorescence analysis was used to quantify element concentrations on the filters and pads. The XRF was capable of mapping the filters and pads with a resolution of 50 µm, providing spatial information on the scale of the filters. This information provides a link between the SEM data, which is confined to small areas on the sample surface, and the chemical analysis, which does not discriminate spatially, but rather provides an averaged composition for all the phases present. Moreover, the analysis provides element ratios which can be used to estimate the concentration of silica, which cannot be readily measured on the very small samples.

EPRI Filter blank

The XRF results, X-ray spectrum, element maps, and semi-quantitative chemical analysis, for the EPRI filter blank are shown in Figure 23. The X-ray spectrum shows a strong peak for Ti and not much else. Only elements greater than sodium can be detected with this method, so the filter is largely composed of light elements (C and O) that go undetected in this characterization. Other elements labeled in the spectrum are Rh (from X-ray source), a very weak Fe signal (likely scatter from the beam collimator), K and Sb. Element maps for these elements show that the underlying Teflon holder upon which the samples are placed has a similar signature. Therefore it is likely that the signals for these elements are artifacts and should be ignored.

The Ti signal is real, and is distributed throughout the entire filter sample; it may represent Ti-oxide particles added to color the filters white.

EPRI Scotch-brite blank

Results of the EPRI Scotch-brite© pad blank are shown in Figure 24. XRF mapping showed the ubiquitous presence of Al, consistent with the alumina abrasive dispersed throughout the sample.

Additional elements detected in significant quantities were Si and Ti. The Si signal appeared discrete but reasonably well distributed across the blank. The discrete points of intensity suggest that a quartz crystals may be present throughout the sample.

The Ti signal was also dispersed evenly in this sample. However, in a second sample, the backside of the pad was analyzed. In this case, the Ti showed high spatial dependence, with the Ti signal concentrated in spots corresponding to stenciled white letters on the back of the pads. It is likely present as a pigment in the lettering paint.

Other elements such as Fe, Ca, Mn, and K showed significant intensity above background to warrant being considered components of the pads, and not artifacts. These elements correlate in terms of location in the chemical maps, suggesting that a phase or phases are present that are composed of these elements. The MSD sheet for these pads indicates that the alumina is "mineral"; if the alumina is a natural phase, then other accessory minerals may be present as well.

As with the filter blank, Rh is from the X-ray source and is artifact. The elements Cr and S are only weakly observed in the sample and are arguably at the background level.

EPRI #1 filter

XRF results for the EPRI #1 filter are given in Figure 25. XRF mapping showed evidence of Ti throughout the filter, as seen in the filter blank. However, more importantly, the element maps showed that Ca, Si, Fe, S, K, and Al were spatially concentrated near the center of the filter. This location also corresponds to the visually observed region of discoloration on the filter (Figure 5). This suggests that these elements are enriched in the dust, and are not a contaminant from other sources, or an experimental artifact.

EPRI #1 pad

Results for the EPRI #1 pad are given in Figure 26. The XRF mapping is very similar to the pad blank sample (Figure 20) over most of the pad. However, there is a distinct region of the pad that shows highly correlated chemical maps for Si, Ca, and S. Sulfur not a strong scatterer in terms of overall signal; however, the strong spatial dependence of the S signal and its spatial correlation with Ca and Si suggests that S is indeed a major component in the dust.

EPRI #4 filter

XRF results for the EPRI #4 filter are provided in Figure 27. XRF element mapping of the #4-A filter yielded similar results as for the #1-A filter, in that Ca, Si, S, K, and Al tended to be spatially co-located, in this case along the upper edge of the filter. This filter is less discolored than #1-A, suggesting that less dust was present. A strong Cr signal was detected in the lower middle of the filter, and correlated strongly with Fe at that location. The correspondence of Cr and Fe suggests that the deposited materials at this location may be sourced to a steel alloy. The dust may have have been generated by abrasion of the steel waste package surface by the abrasives in the Scotch-brite© pad, or perhaps by abrasion of corrosion products on the metal surface.

EPRI #4 pad

Results for the EPRI #4 pad are given in Figure 28. XRF mapping for this sample shows a definitive spatial correlation of Ca and S. In this case, the spatial concentration of these elements is at the bottom edge of the pad. The overall XRF spectrum shows a much higher S signal than previous analyses. Visually, one can see a discoloration of the pad on the bottom edge. This would suggest that more material is deposited on this pad than on the others.

Figure 23. Results of XRF analysis of the EPRI filter blank (X-ray spectrum, element maps, and semi-quantitative analytical analysis).
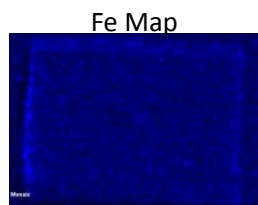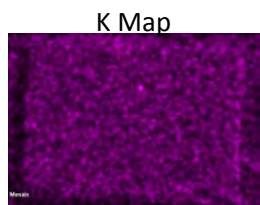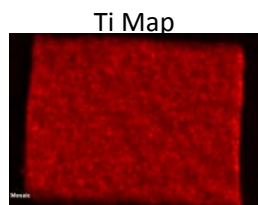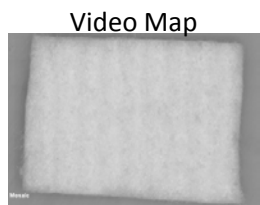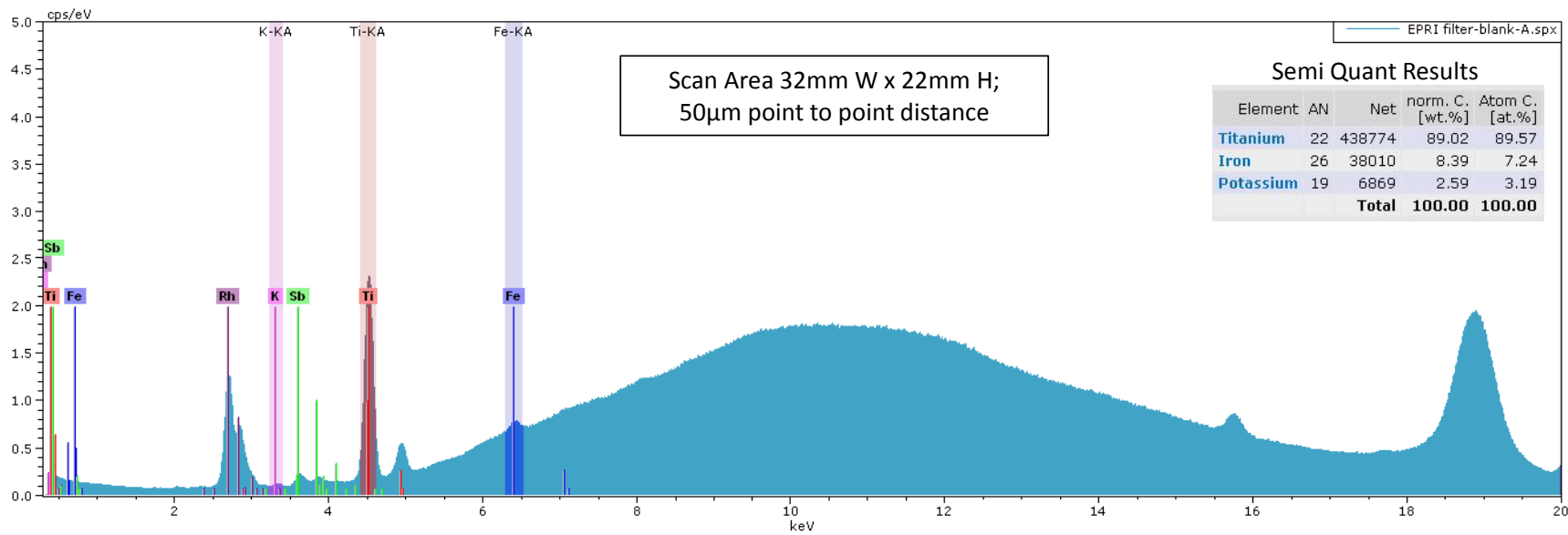
Figure 24. XRD results for EPRI Scotch-brite© pad blank (X-ray spectrum, element maps, and semi-quantitative analytical analysis).
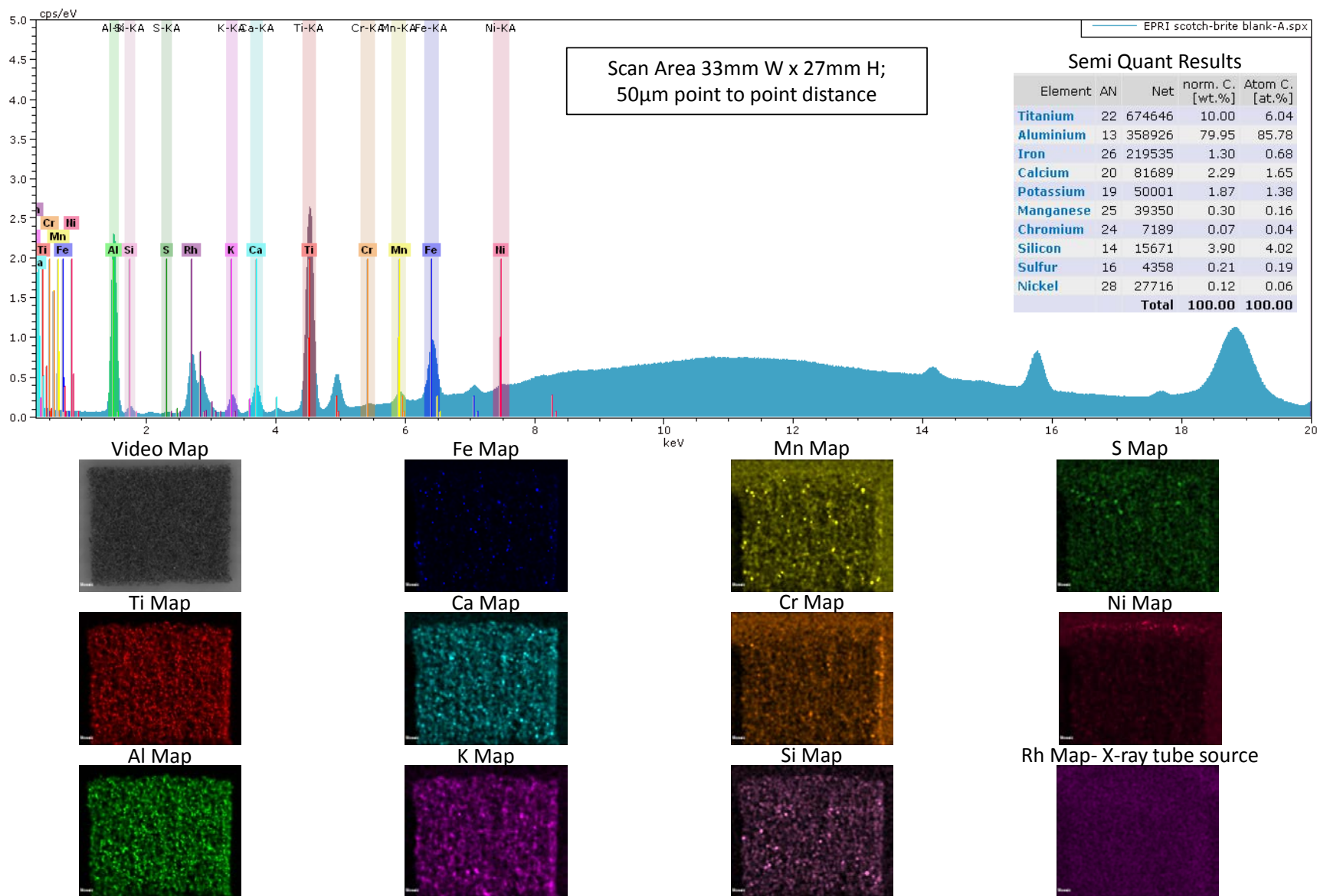
Figure 25. XRD results for EPRI #1 filter (X-ray spectrum, element maps, and semi-quantitative analytical analysis).

Element	AN	Net	norm. C. [wt.%]	Atom C. [at.%]
Titanium	22	419800	34.61	30.00
Aluminium	13	2789	3.97	6.11
Iron	26	363264	16.38	12.18
Calcium	20	277014	26.50	27.45
Potassium	19	33877	3.86	4.10
Manganese	25	22220	1.23	0.93
Chromium	24	6503	0.44	0.35
Silicon	14	21867	11.17	16.51
Sulfur	16	16222	1.83	2.36
Total			100.00	100.00

Scan Area 32mm W x 22mm H; 50µm point to point distance
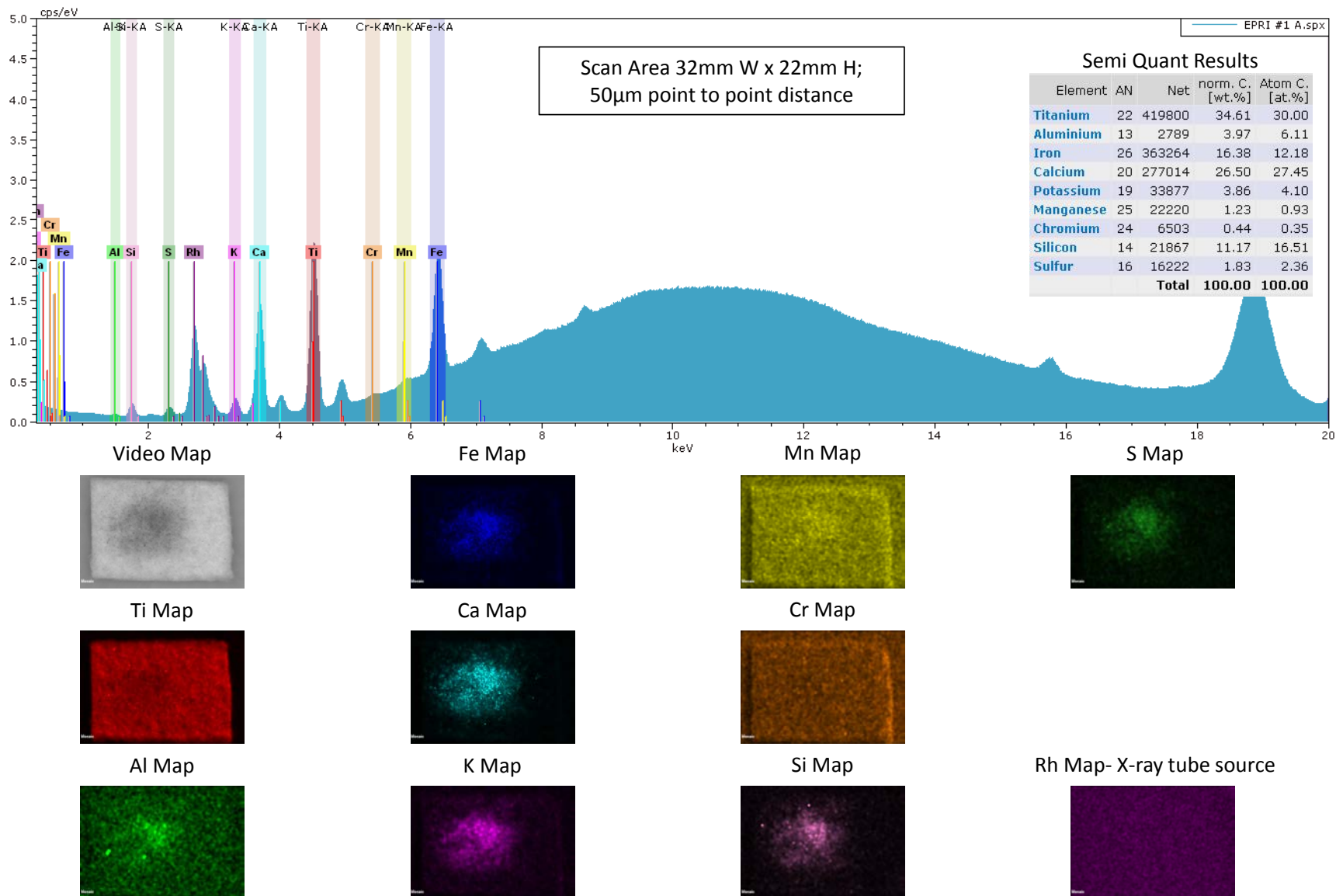
Figure 26. XRD results for EPRI #1 pad (X-ray spectrum, element maps, and semi-quantitative analytical analysis).
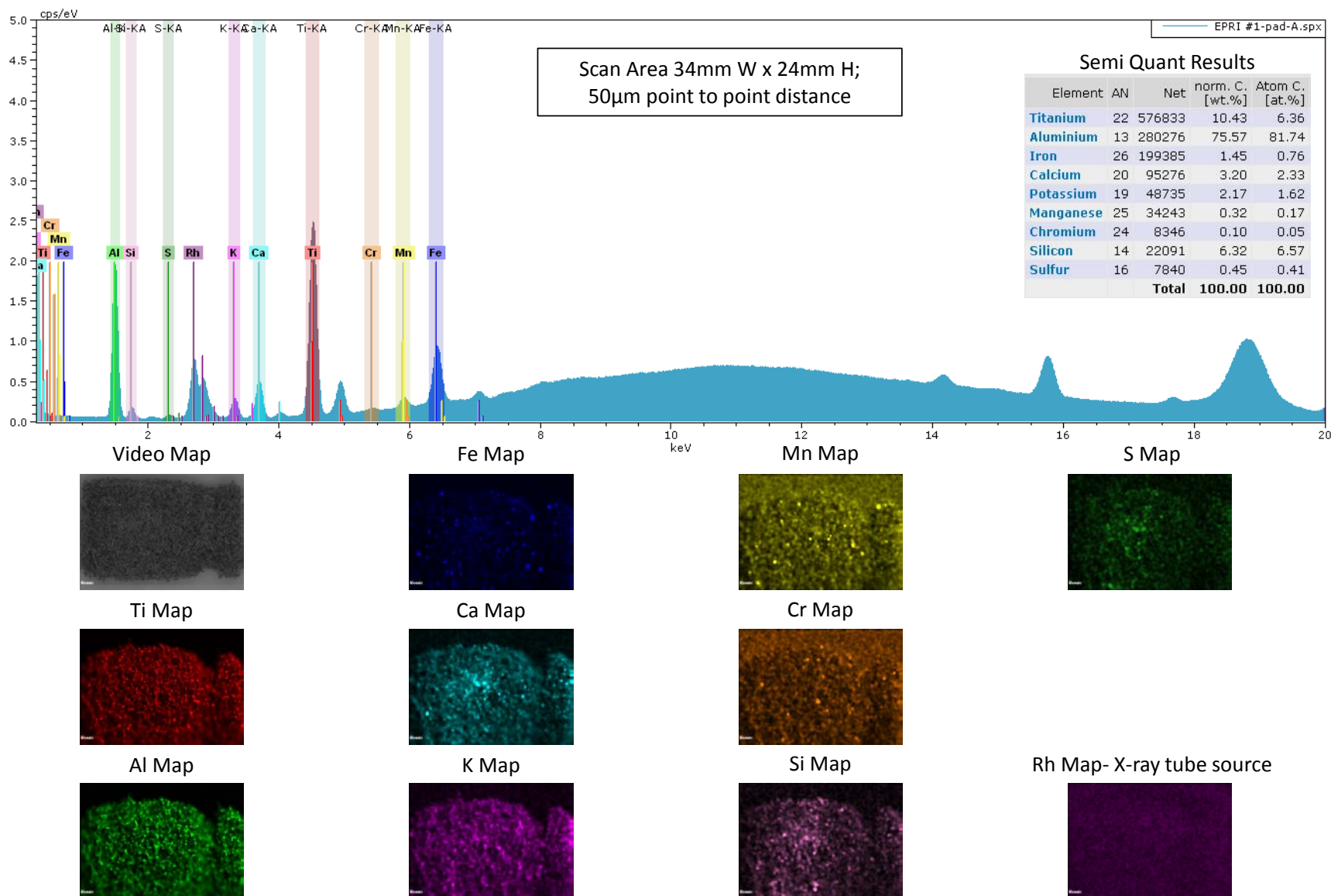
Figure 27. XRD results for EPRI #4 filter (X-ray spectrum, element maps, and semi-quantitative analytical analysis).

Scan Area 32mm W x 22mm H;
50μm point to point distance

Semi Quant Results

Element	AN	Net	norm. C. [wt.%]	Atom C. [at.%]
Titanium	22	388676	46.79	40.78
Aluminium	13	2336	5.46	8.45
Iron	26	158581	12.25	9.16
Calcium	20	117556	17.99	18.73
Potassium	19	10389	1.97	2.11
Manganese	25	12175	1.15	0.88
Chromium	24	12403	1.44	1.15
Silicon	14	11919	10.23	15.20
Sulfur	16	14603	2.72	3.54
		Total	100.00	100.00

Video Map   Fe Map   Mn Map   S Map

Ti Map   Ca Map   Cr Map

Al Map   K Map   Si Map   Rh Map- X-ray tube source

Figure 28. XRD results for EPRI #4 pad (X-ray spectrum, element maps, and semi-quantitative analytical analysis).
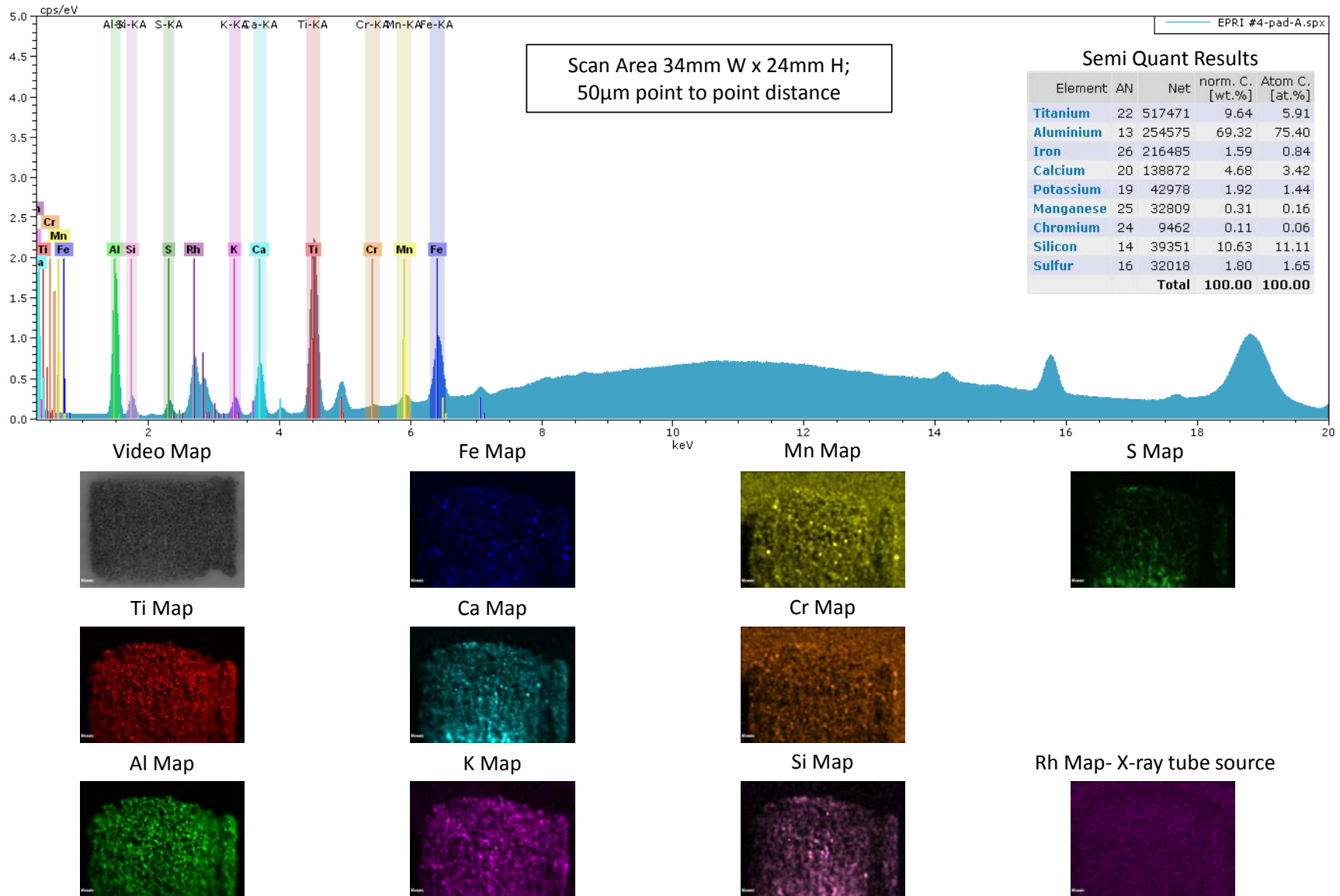
2.3.2.3   XRD Analysis

X-ray diffraction analysis of the dust on the filters and pads was unsuccessful. For the Scotch-brite©
pads, the only the diffraction pattern for the alumina abrasive was observed, and the porous, 3-D nature of
the pads resulted in peak doubling and widening. For the filter samples, the density of material on the
substrates was simply too low for analysis. The XRD patterns (Figure 29) showed the signal from the
polyester fibers, but only faint peaks from the dust were visible—too small to identify any phases. It is
notable, perhaps, that alumina peaks were not observed. Apparently, the Scotch-brite pads did not shed
abrasive particles as badly as initially expected.

During preparation for XRD and XRF, a small amount of powder was inadvertently dislodged from the
EPRI #4 pad. The dust was loaded into the XRD, and analyzed. The resulting diffraction pattern (Figure
30) shows sharp peaks for quartz, and also peaks for gypsum. Perhaps surprisingly, no alumina was
observed. Apparently, although the abrasive in the pads is readily dislodged when the pad is cut, it is not
readily loosened during normal use or handling.

2.3.2.4   GC-MS analysis

GC-MS analysis of possible organic compounds in the dust was unsuccessful. The blanks filter and pad
blanks were anlayzed with the samples, and no organics were observed during sample analysis other than
those observed on the blanks. This is illustrated in Figure 31 for the Scotch-brite© blanks and samples
run in the "split" mode at 250ºC; The patterns for the blanks and samples match exactly.

When a separate aliquot of each sample was run in a no-split mode to improve resolution, more peaks
were observed in each heating step (Figure 32); however, there are no major differences between the
peaks observed in either the filter or Scotch-brite© samples as compared to their respective blanks. The
large signal of the Scotch-brite© samples as the heating temperature is increased necessitated that they
only be tested at 100 and 200°C in the no-split mode.
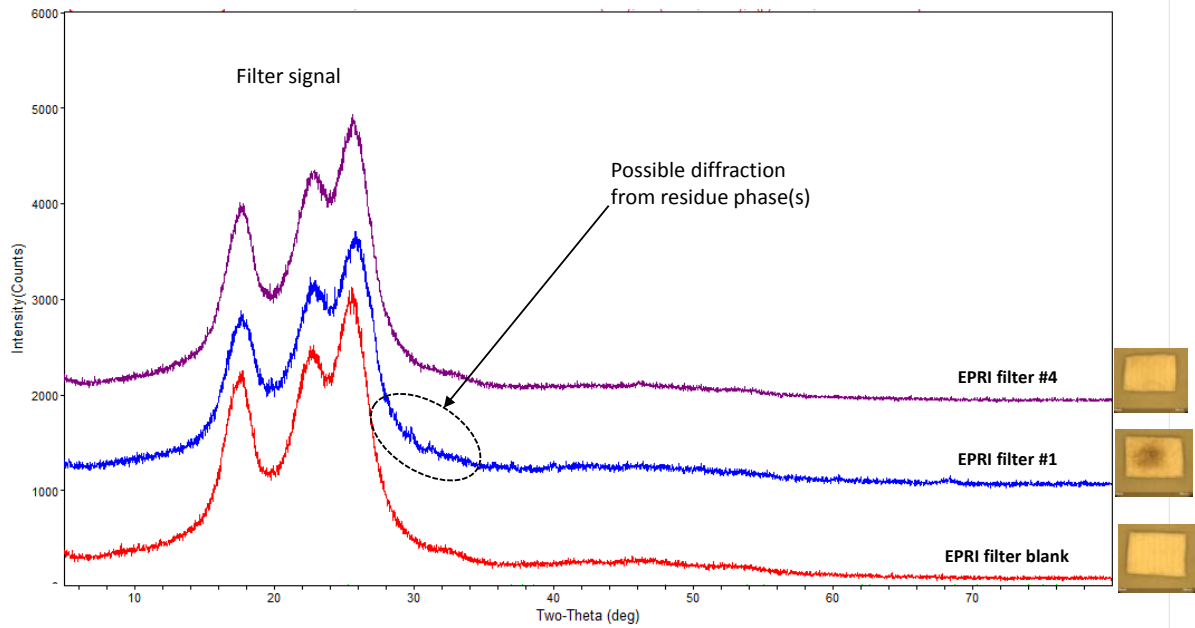
Figure 29. X-ray diffraction patterns for the blank, EPRI #1, and EPRI #4 filters.
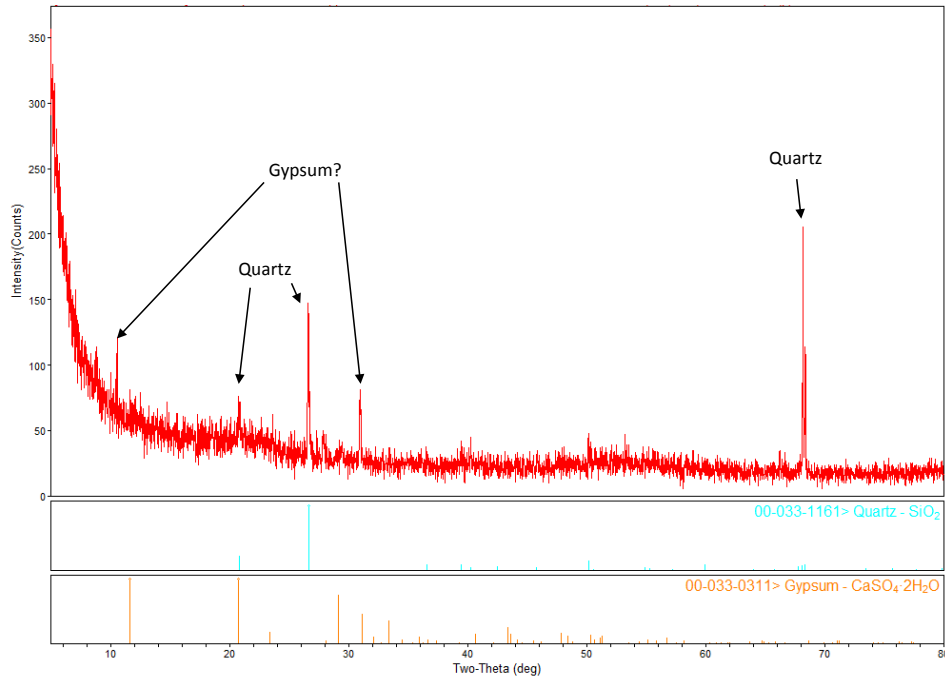
Figure 30. X-ray diffraction pattern for dust particles dislodged from the EPRI #4 pad during handling.
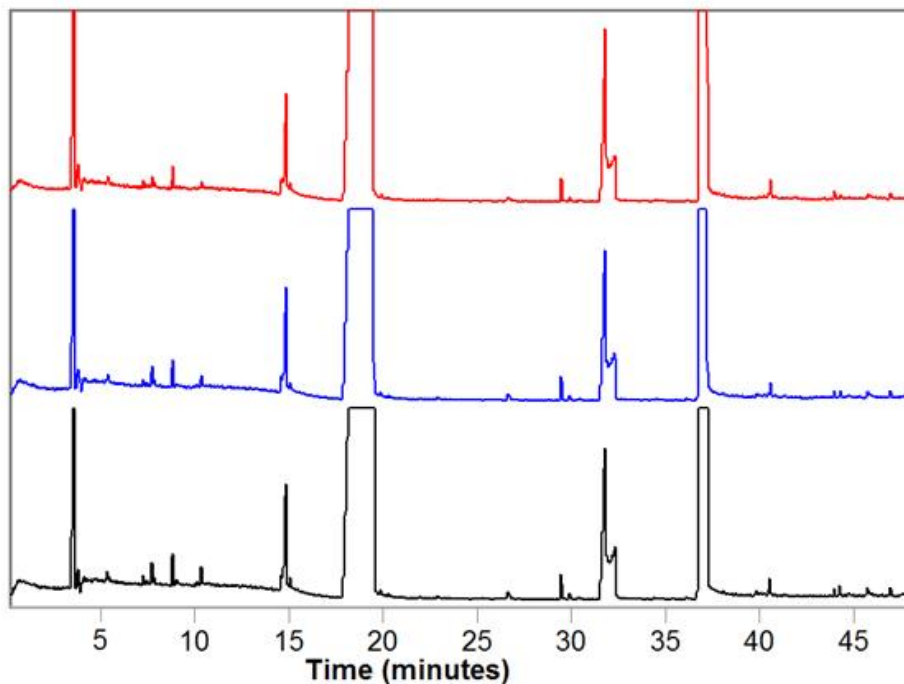
Figure 31. GC-MS total ion signal versus retention time for the Scotch-brite© blank, #1, and #4 samples (top to bottom). The y-axis is greatly expanded to show the minor peaks.
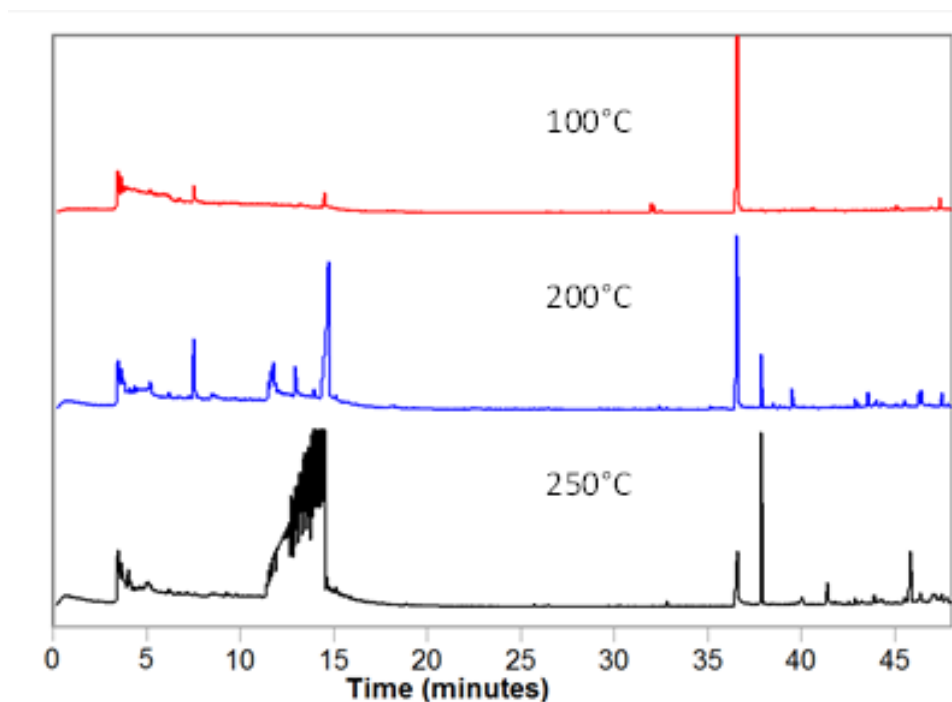
Figure 32. GC-MS total ion signal versus retention time for the EPRI#4-filter sample tested in splitless mode.

2.3.2.5   FTIR Spectroscopic Analysis

FTIR analysis of materials and blanks was accomplished by leaching the samples first with isopropyl alcohol to remove polar organics, and then with hexane the remove hydrocarbons, if present, and then analyzing the leachates (Figure 33). For the filters, there was no significant difference between the blanks and samples, using either leachate. However, for leached pads, a phase leached out of the EPRI #4 pad that was not present in the blank. This phase has been tentatively identified as a primary amide by comparison with reference patterns.

Primary amides are degradation products of proteins, and the amide may represent breakdown of organic matter in the dust due to heat, radiation, or chemical reactions. However, it is more likely that the amide is a contaminant from the filter or pad. Primary amides are widely used in resins and as slip agents and may be present in the cured resin holding the pad together. Moreover, nylon itself an amide. It was hypothesized that the amide was a breakdown product of the scrubber, exposed by abrasive action (or, when the sample was cut into subsamples with scissors), allowing it to be extracted. To test this, a piece of the blank pad was abraded and leached with hexane; however, the resultant leachate did not contain any detectable amides. Further examination of the analyses showed that the amide was present in low concentrations on all of the filter samples, including the blank. It is possible that the source of the amide contaminant is actually the filters, but it was transferred to the EPRI #4 pad during storage. Or, both the pads and the filters may have absorbed the amide while they were stored, or during shipping. In any case, the presence of the amide on the filter blank strongly suggests it is an artifact, and was not a component in the dust.
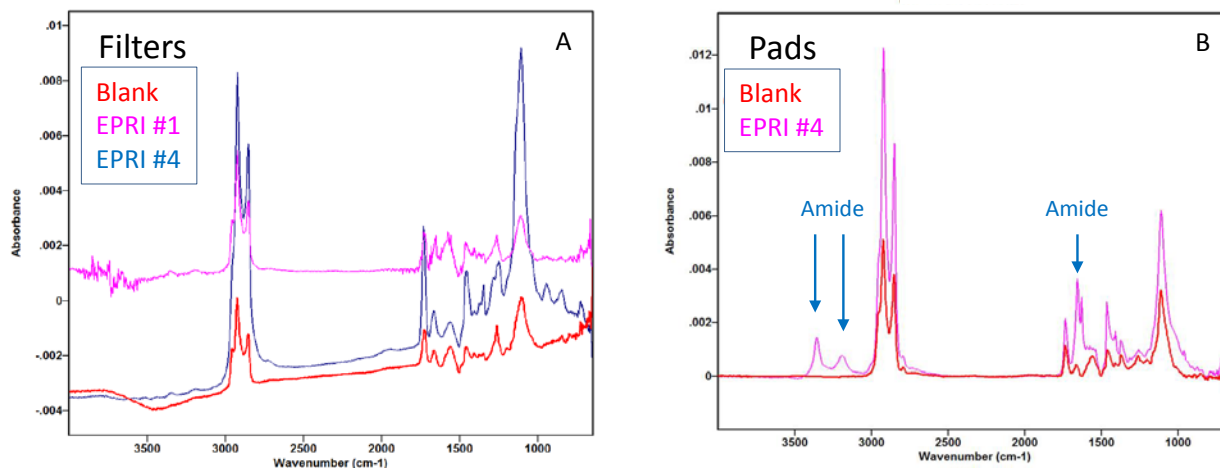
Figure 33. FTIR spectra for the hexane leaches of the EPRI blank and sample filters (A) and Scotch-brite© pads (B). Peaks representing an amide are clearly visible in the EPRI#4 pad sample.

2.3.2.6   Raman Spectroscopic Analysis

For the Raman spectroscopic analysis the pads and filters were gently tapped against a salt plate, and dislodged dust grains were examined by microscope. The EPRI #4 filter and pad yielded very little material, and the grains were too small for even micro Raman analysis. However, the brown material on the EPRI #1 filter was readily dislodged, and transferred to the salt plate. The particles collected are shown in optical microscope images in Figure 34. Microscopic examination showed that the dust particles that were large enough to analyze were dominantly pollen grains. The pollen grains were not analyzed by Raman Spectroscopy—they charred in the laser beam. Glassy mineral grains were also present albeit much rarer than the pollen; Raman analysis showed that they were quartz (Figure 35A). Finally, black granular material was identified as soot (Figure 35B). No other mineral phases were identified. The limits of resolution for this method prevent it from being useful to identify the >5µm inorganic minerals that dominated the inorganic component of the dust in SEM observations.
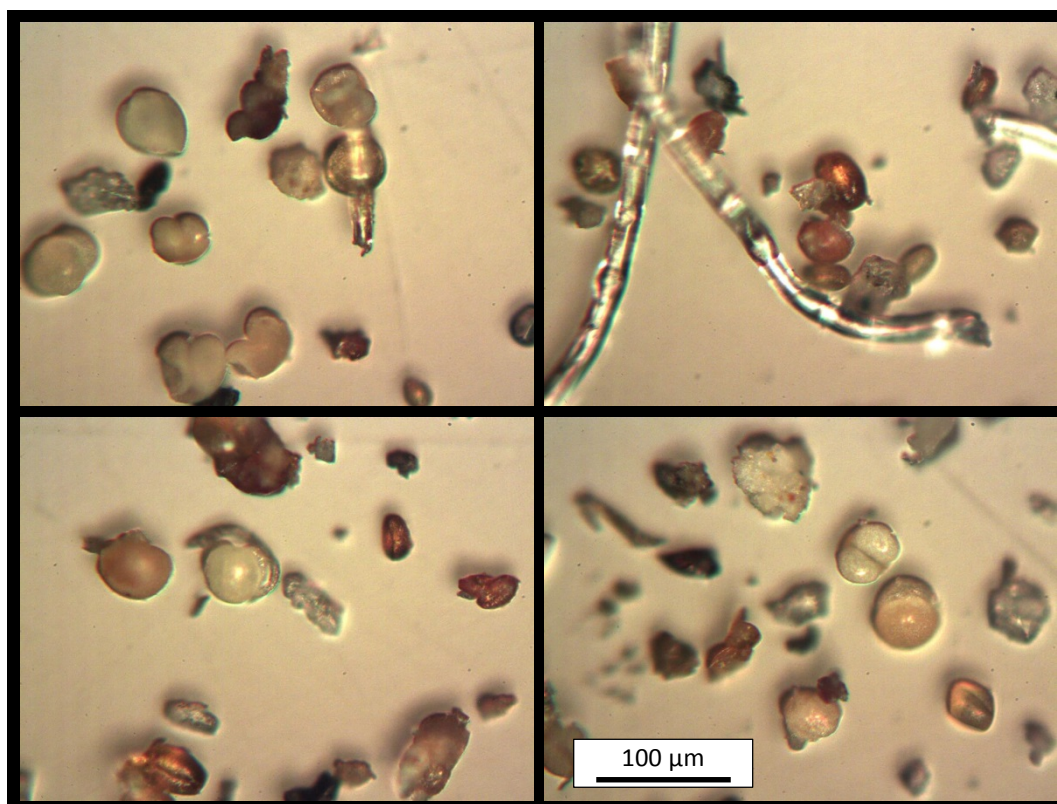
Figure 34. Optical microscope images of dust collected from the EPRI #1 filter for Raman spectroscopic analysis. Large fibers are polyester fibers from the filter.
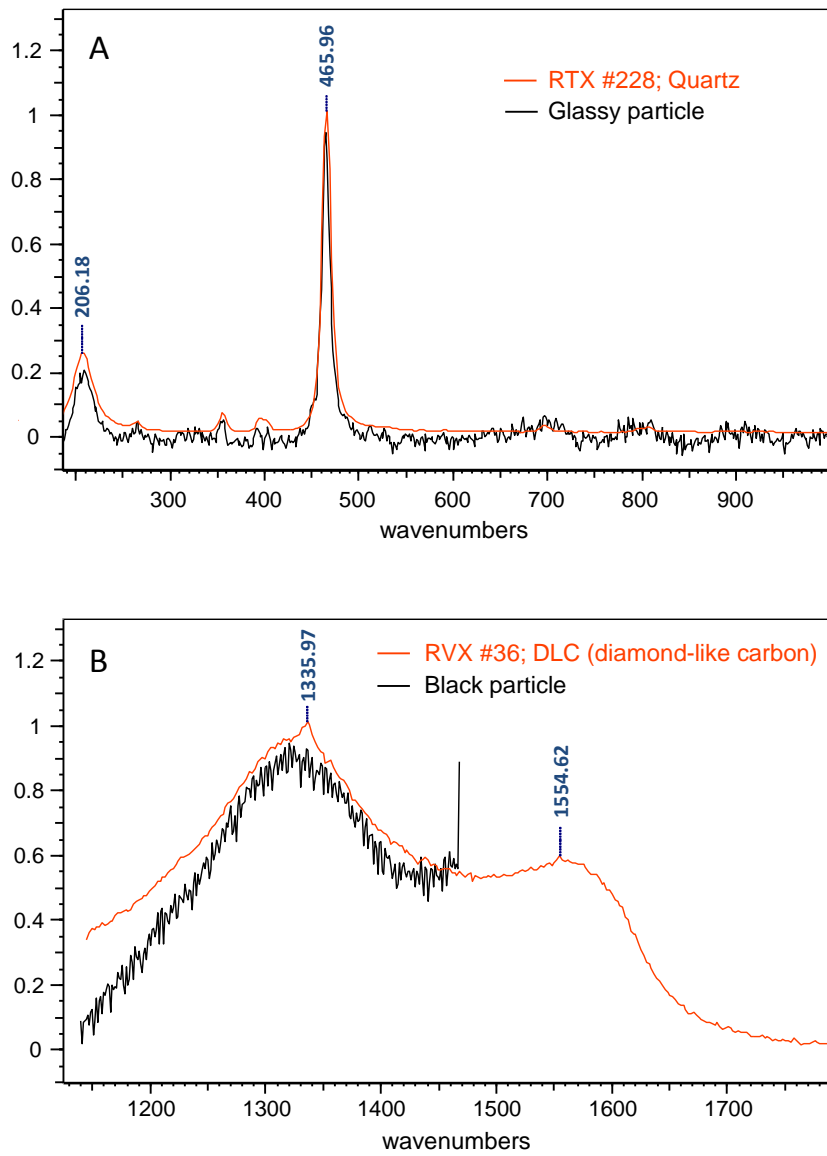
Figure 35. Raw and matching library spectra for dust particles from the EPRI #1 filter. A) quartz; B) soot.

2.3.2.7   Chemical Analyses

Water-soluble salts

Measured masses for the water-soluble solutes in µg in the samples and blanks, including the Whatman filter blank, are shown in Table 3. Not shown are Br^- and NO_2^-, which were below detection limits in all samples. Detection limits are based on analyses of standards as unknowns.

Also provided are the masses of the Whatman paper filters used for each sample, and the total mass of each sample analyzed (~1/2 of each filter or pad). The weights for the Whatman filters vary significantly, because the paper filters were trimmed prior to use to facilitate rinsing with small volumes of water; however, for the Whatman filter blank, an entire filter was used. The masses of the samples vary because each filter and pad was cut in half prior to analysis, and there were variations in the size of the analyzed piece.

Table 3. Compositions of the soluble fraction leached from the blanks and samples (µg/sample).

| Ion	Whatman blank	Filter blank	Pad Blank	EPRI #1 filter	EPRI #1 pad	EPRI #4 filter	EPRI #4 pad
Na^+	1.84	5.11	4.02	23.9	19.2	4.03	15.3
K^+	0.56	3.75	1.96	21.6	15.8	4.05	9.69
Ca^{+2}	0.27	0.97	0.55	78.0	21.3	24.9	154
Mg^{+2}	0.04	0.12	0.03	17.0	6.00	2.04	17.7
F^-	n.d.	0.48	0.37	0.74	1.01	0.15	0.29
Cl^-	19.9	6.47	9.13	12.1	11.0	5.61	11.7
NO_3^-	35.8	7.39	7.22	29.0	25.1	12.6	25.8
SO_4^{-2}	0.81	1.47	2.16	91.0	53.9	49.2	293
PO_4^{-3}	n.d.	0.53	n.d.	7.17	2.05	0.87	n.d.
Total mass, µg	59.2	26.3	25.4	281	155	104	527
Whatman filter mass, g	0.7047	0.1185	0.2447	0.1262	0.3144	0.1422	0.2280
Sample mass, g	—	0.1977	0.9574	0.1816	1.0193	0.1559	0.9523

For most analytes, the contribution from the Whatman paper filter is insignificant. However, the Whatman filter did contain relatively large amounts of nitrate and chloride. As there is no balancing cation, it is likely that these represent acid gases adsorbed from the laboratory atmosphere over the months of storage in the lab environment. Given the importance of chloride and nitrate to this study, this is unfortunate, and in future work, alternate paper filters will be used, or the filters will be thoroughly rinsed prior to use to eliminate adsorbed anions. In some cases, the mass of analyte leached from the Whatman filter paper sample was larger than that from the samples—that is because a much larger mass of the Whatman filter paper was used to determine the filter paper concentrations. Correcting for the

Whatman filter requires normalizing the measured Whatman blank value to the amount of Whatman filter present.

In Table 4, the masses have been corrected for the Whatman filter blanks. Because chloride and nitrate values are quite low in the blanks and in the samples, correcting for the Whatman filters had a significant effect on the concentrations of these analytes. The data in Table 2 provide information on what is being leached from the pads and filters, as opposed to the deposited dust. Concentrations in the blank leachates are quite low for all the analytes, but are significant relative to the concentration in the sample leachates for Na^+, K^+, F^- and Cl^-. To determine the actual dust compositions, the contribution of the fiber filters and abrasive pads was subtracted from the sample values, using the mass of each sample relative to the mass of the blank to correct for the blank contributions. This is valid because the mass of the actual dust is negligible relative to the mass of the substrate.

Table 4. Compositions of the soluble fraction, after subtracting the Whatman filter contribution (µg/sample).

Ion	Filter blank	Pad Blank	EPRI #1 filter	EPRI #1 pad	EPRI #4 filter	EPRI #4 pad
Na^+	4.80	3.38	23.6	18.4	3.66	14.7
K^+	3.66	1.77	21.4	15.6	3.93	9.50
Ca^{+2}	0.92	0.46	78.0	21.1	24.9	154
Mg^{+2}	0.11	0.01	17.0	5.98	2.03	17.7
F^-	0.48	0.37	0.74	1.01	0.15	0.29
Cl^-	3.13	2.23	8.52	2.08	1.60	5.32
NO_3^-	1.37	n.d.	22.6	9.09	5.43	14.2
SO_4^{-2}	1.33	1.87	90.9	53.5	49.0	292
PO_4^{-3}	0.53	n.d.	7.17	2.05	0.87	n.d.
Total mass, µg	16	10	270	129	92	508

In Table 5, the sample concentrations are presented after correcting for both the Whatman filter and the fiber filter and pad planks; these values represent the actual amount of each analyte extracted from the dust on each sample. These amounts are converted to microequivalents in Table 6.

There are several important features to the data. Charge balances are poor for all samples, especially for the #1 samples. In all cases, there is a deficiency of anions relative to cations. It is possible that the analyses are poor; however, a large deficiency in anions was also observed in independent analyses carried out on samples collected from the packages at the Calvert Cliffs ISFSI (Calvert Cliffs Nuclear Power Plant LLC 2013b). It is more likely that an unanalyzed anionic species, such as carbonate or hydroxyl, is present.

Table 5. Compositions of the soluble fraction of the dusts, after subtracting the Whatman filter and filter and pad contributions (µg/sample).

Ion	EPRI #1 filter	EPRI #1 pad	EPRI #4 filter	EPRI #4 pad
Na^+	19.2	14.8	n.d.	11.3
K^+	18.1	13.7	1.05	7.75
Ca^{+2}	77.1	20.6	24.1	153
Mg^{+2}	16.9	6.0	1.95	17.6
F^-	0.30	0.61	n.d.	n.d.
Cl^-	5.64	n.d.	n.d.	3.10
NO_3^-	21.3	9.09	4.34	14.2
SO_4^{-2}	89.7	51.5	48.0	291
PO_4^{-3}	6.68	2.05	0.45	n.d.
Total mass, µg	255	118	80	498

Although the EPRI#1 filter was strongly discolored, The EPRI #4 pad was the most heavily loaded. It is quite likely that the mass of dust from the EPRI #1 samples was greater than the EPRI#4 samples; however, it consisted largely of pollen, which did not contribute significantly to the salt load. No pollen was observed on the EPRI #4 samples, but the fine dust fraction was very abundant, especially on the pad. It is clear that this is the dust fraction that is most heavily salt-loaded.

For all samples, Ca^{+2} is the dominant cation present , comprising 59% and 41% of the total cation equivalents in the #1 filter and pad, respectively, and 87% and 78% in the #4 filter and pad, respectively. SO_4^{-2} is the dominant anion that was measured, comprising 72% and 81% of the total anion equivalents measured in the #1 filter and pad, and 92% and 95% in the #4 filter and pad, respectively. However, given the deficiency of anions in all of the analyses, another anion, such as carbonate could contribute significantly, or, for the #1 samples, even be the dominant anion.

Table 6. Compositions of the soluble fraction of the dusts, in µEq.

Ion	EPRI #1 filter	EPRI #1 pad	EPRI #4 filter	EPRI #4 pad
Na^+	0.84	0.64	n.d.	0.49
K^+	0.46	0.35	0.03	0.20
Ca^{+2}	3.85	1.03	1.20	7.64
Mg^{+2}	1.39	0.49	0.16	1.45
F^-	0.02	0.03	n.d.	n.d.
Cl^-	0.16	n.d.	n.d.	0.09
NO_3^-	0.34	0.15	0.07	0.23
SO_4^{-2}	1.87	1.07	1.00	6.05
PO_4^{-3}	0.21	0.06	0.01	n.d.
Total cations (µEq)	6.54	2.51	1.39	9.78
Total anions (µEq)	2.60	1.32	1.08	6.37
Charge Balance, %*	43.1	31.3	12.4	21.2

*Charge bal. = [(Cations – Anions)/(Cations + Anions)] * 100

Bulk chemistry of the insoluble fraction

Measured masses for the insoluble materials in the samples and blanks, including the Whatman filter blank, are shown in

Table 7. The insoluble materials in the blanks and samples, after correcting for the Whatman filter, are shown in

Table 8. Finally, after subtracting the blank concentrations,

Table 9 shows the insoluble fraction of dust adhering to the EPRI #1 and #4 filters and Scotch-brite© pads. The Si concentrations in

Table 9 were calculated from the summed soluble and insoluble Ca concentrations in each sample and the Ca/Si ratio for each sample, as determined by XRF (Section 2.3.2.2)

If it is assumed that all soluble salts, including carbonates, where extracted by the DI water leaching step, then the remaining elements are present as oxides and silicates. Converting the measured elemental concentrations to oxide concentrations allows calculation of the actual mass of dust present, as it intrinsically includes the mass of oxygen in the material. That is why bulk compositions of geomaterials are commonly presented as oxide concentrations. The oxide concentrations of the insoluble dust residues are given in Table 10. Despite the heavy discoloration on the EPRI #1 filter, it is the EPRI #4 Scotch-

brite© pad that has the highest insoluble dust load, at nearly 2 mg. It is important to remember, however, that the values here do not include insoluble organics; carbon was not analyzed. It is likely that the total mass of dust was greatest on the EPRI#1 filter, but the largest fraction of that material was pollen and other plant material, and has not been included here.

Table 7. Compositions of the insoluble materials in the blanks and samples (µg/sample).

Element	Whatman blank	Filter blank	Pad Blank	EPRI #1 filter	EPRI #1 pad	EPRI #4 filter	EPRI #4 pad
Na	7.74	3.25	3.98	16.8	11.5	7.12	10.5
K	1.91	3.65	1.40	25.8	13.9	7.63	13.5
Ca	8.46	5.59	4.44	225	90.2	52.6	92.1
Mg	0.98	0.67	0.53	81.3	30.6	22.2	36.0
Fe	2.27	4.49	1.76	84.2	33.9	32.5	41.1
Al	1.98	1.24	1.36	104	43.3	23.0	48.6
Total	23.3	18.9	13.5	537	223	145	242

Table 8. Compositions of the insoluble materials in the blanks and samples, corrected for the Whatman filter contribution (µg/sample).

Element	Filter blank	Pad Blank	EPRI #1 filter	EPRI #1 pad	EPRI #4 filter	EPRI #4 pad
Na	1.94	1.30	15.4	8.00	5.55	7.97
K	3.33	0.74	25.4	13.0	7.24	12.9
Ca	4.17	1.50	223	86.4	50.9	89.4
Mg	0.51	0.19	81.1	30.2	22.0	35.7
Fe	4.10	0.97	83.8	32.9	32.0	40.3
Al	0.91	0.67	104	42.4	22.6	48.0
Total	15.0	5.4	533	213	140	234

Table 9. Compositions of the insoluble dust fractions (µg/sample).

Element	EPRI #1 filter	EPRI #1 pad	EPRI #4 filter	EPRI #4 pad
Na	13.6	6.62	4.02	6.68
K	22.4	12.2	4.61	12.2
Ca	219	84.8	47.6	87.9
Mg	80.6	30.0	21.6	35.5
Fe	80.0	31.8	28.8	39.4
Al	103	41.7	21.9	47.3
Si*	137	280	46.7	679

* Si was estimated from XRF Ca/Si ratios

Table 10. Compositions of the insoluble dust fractions recalculated as oxides (µg oxide/sample).

Element	EPRI #1 filter	EPRI #1 pad	EPRI #4 filter	EPRI #4 pad
Na_2O	18.3	8.93	5.42	9.00
K_2O	26.9	14.7	5.55	14.6
CaO	307	119	66.6	123
MgO	134	49.7	35.8	58.9
Fe_2O_3	114	45.5	41.1	56.3
Al_2O_3	195	78.8	41.4	89.3
SiO_2	293	600	100	1452
Total	1088	916	296	1803

The oxide compositions are normalized to 100% in Table 11. This normalization allows direct comparison of the bulk compositions of the different samples. Examining this data, it is apparent that the pad samples are consistently more silica-rich. When the oxides are normalized to 100%, the higher silica in the pad samples drives the mass fraction of all the other components lower.

It seems likely that the difference in dust composition between the filters and the pads is due to differences in the retained particle size. The coarsely porous pads no doubt capture a different size fraction than the filter pads. The coarse dust particles of pollen and quartz observed during Raman analysis may be preferentially retained by the Scotch-brite© pads, while smaller particles pass through and are retained by the filter.

Table 11. Compositions of the insoluble dust fractions in wt%.

Element	EPRI #1 filter	EPRI #1 pad	EPRI #4 filter	EPRI #4 pad
Na_2O	1.68	0.97	1.83	0.50
K_2O	2.48	1.61	1.88	0.81
CaO	28.2	13.0	22.5	6.8
MgO	12.3	5.43	12.1	3.27
Fe_2O_3	10.5	4.97	13.9	3.12
Al_2O_3	17.9	8.6	14.0	4.96
SiO_2	26.9	65.5	33.8	80.5
Total	100	100	100	100

However, the converse may also be true. Perhaps the coarser particles are readily drawn through the porous pad and retained by the filter, while the finer particles, including fine quartz, impact the broad pad fibers and are retained there. This may be more consistent with observation, as pollen was very abundant of the EPRI#1 filter sample, while fine particles (including the highest salt concentrations) were strongly concentrated on the EPRI #4 pad.

Given the high silica concentrations, it is clear that the majority of the silica must be present as a distinct silica phase such as quartz—the concentrations of other oxides are too low to account for the silica as any type of mixed silicate phase. If we assume that a separate silica phase is responsible for the relatively elevated silica concentrations, then it is useful to convert the insoluble compositions to molar concentrations (Table 12) of each element, and then to ratio the concentrations to Ca, the second most abundant species. This removes the diluting effect of the silica. The element/Ca ratios are given in Table 13. The ratios are quite consistent for each element, suggesting that the insoluble fraction other than quartz is compositionally similar for all of the samples.

Table 12. Elemental concentrations in the insoluble dust fractions, (μmoles).

Element	EPRI #1 filter	EPRI #1 pad	EPRI #4 filter	EPRI #4 pad
Na	0.59	0.29	0.17	0.29
K	0.57	0.31	0.12	0.31
Fe	1.43	0.57	0.52	0.70
Al	3.83	1.55	0.81	1.75
Ca	5.47	2.12	1.19	2.19
Mg	3.32	1.23	0.89	1.46
Si	4.87	9.99	1.66	24.2

Table 13. Element/Ca molar ratios in the dust samples

Element	EPRI #1 filter	EPRI #1 pad	EPRI #4 filter	EPRI #4 pad
Na	0.108	0.136	0.147	0.133
K	0.104	0.148	0.099	0.142
Fe	0.262	0.269	0.434	0.321
Al	0.700	0.730	0.683	0.799
Ca	1.00	1.00	1.00	1.00
Mg	0.606	0.583	0.748	0.666
Si	0.890	4.72	1.40	11.0

2.3.2.8   Summary

Two samples of dust that were collected from the surface of interim storage containers at the Calvert Cliffs ISFSI were characterized using several different methods. The most effective methods included chemical analysis, SEM/EDS analysis, and X-ray fluorescence, which can be used to describe the chemical and mineralogical composition of the dusts. Data interpretation is ongoing for these samples, so only the results of the analyses are summarized here.

Dust collected from the packages at Calvert Cliffs displays a bimodal size distribution, with a coarser fraction (~20 – 40µm in diameter) that consists largely of pollen and quartz grains. Sample EPRI #1 is especially pollen-rich. The finer fraction (<5 µm in diameter) consists of both soluble salts (sulfates, nitrates, chlorides, and carbonates) and insoluble minerals (silicates and oxides). The significant differences in salt concentration and bulk mineralogy occur between the filters and the pads, probably because of size segregation in the trapped fraction, and variations in chemical composition with particle size (e.g., the larger size fraction may be more quartz-rich). The soluble cations in the dust are dominated by Ca^{2+}, and the anions, by SO_4^{2-}. Chloride comprises only a small fraction of the total solubles, and SEM analysis indicate that it is present almost entirely as NaCl.

It is clear that, despite the location of the Calvert Cliffs ISFSI adjacent to Chesapeake Bay, the salts deposited on the storage containers are not sea salts. The composition of sea water is provided in Table 2. Cations in sea water are dominated by Na^+, with lesser amounts of Mg^{2+}, Ca^{2+}, and K^+. Cl^- is by far the most abundant anion, but SO_4^{2-} is also abundant. The assemblage of salts that precipitate when seawater evaporates is dominated by NaCl, with lesser amounts of $CaSO_4 \times nH_2O$, $MgCl_2 \times nH_2O$, and KCl. Sea salt aerosols are characterized by high concentrations of Na, Mg, and Cl relative to continental aerosols (Figure 36).

Conversely, the salts sampled from the storage containers are dominantly calcium sulfate-rich; chloride is a trace species, present largely as NaCl. While particle-gas conversion reactions such as those described in Section 2.2 can modify deposited salts after deposition, these processes only affect the anionic components (e.g., exchange of nitrate or sulfate for chloride); they do not affect the alkali metal or alkaline earth concentrations. The trace amounts of Na in the soluble fraction of the dust samples strongly suggests that the salts are not marine in origin; instead, the composition of the soluble materials strongly suggests that they are largely continental in origin (Figure 37). Given the proximity of the Calvert Cliffs site to the ocean, or at least to the brackish Chesapeake Bay, this was not expected.
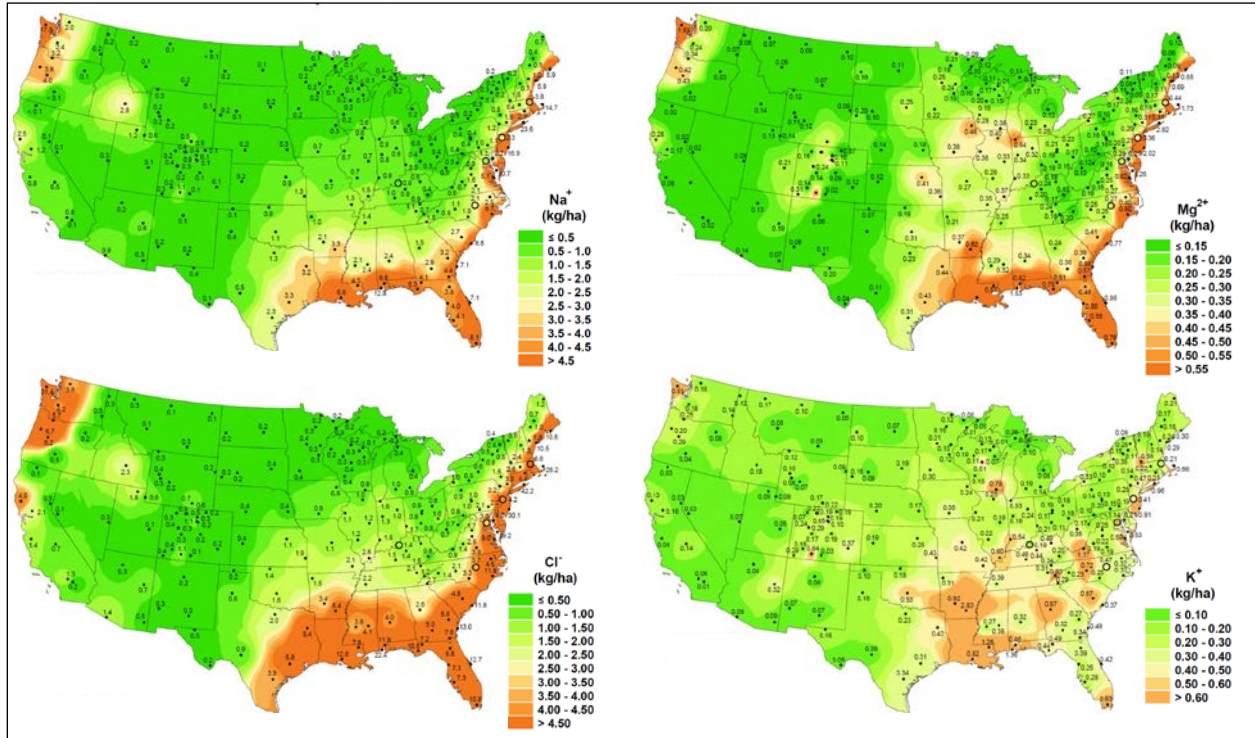
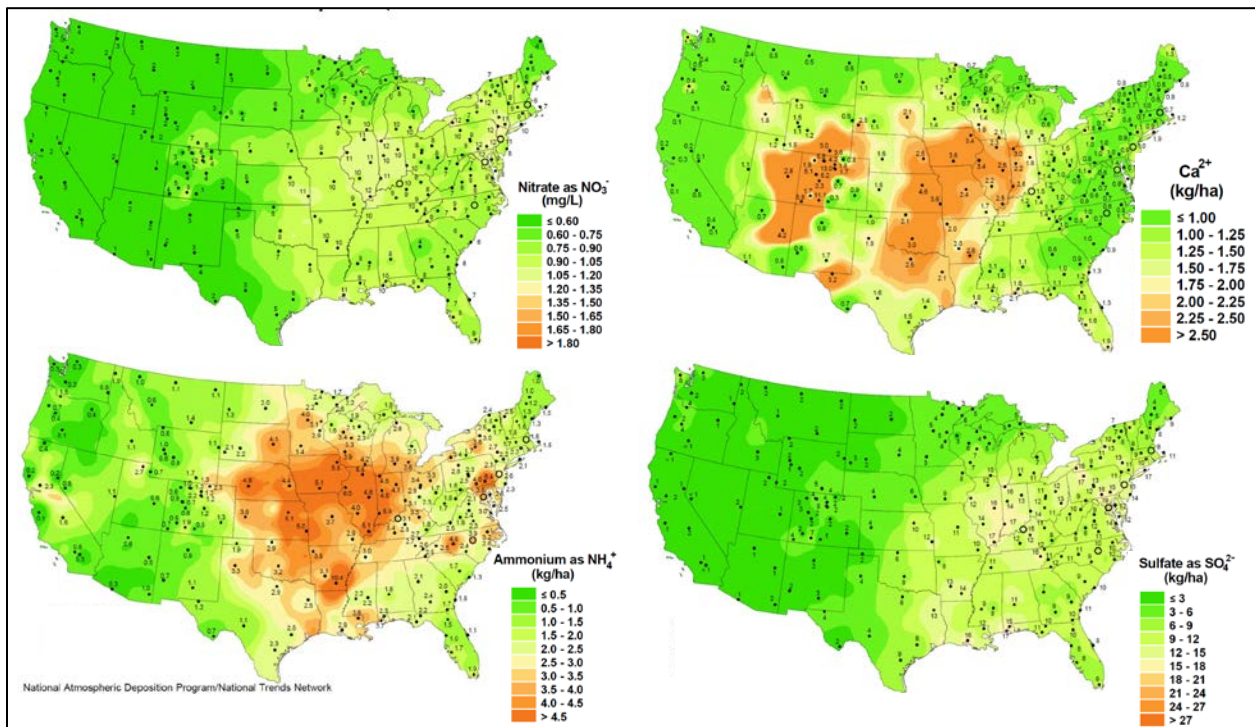Figure 36. NADP deposition maps for elements enriched in marine aerosols.

Figure 37. NADP deposition maps for elements enriched in continental aerosols.

3.   IMPACT OF DELIQUESCED BRINES ON LOCALIZED CORROSION PERFORMANCE OF INTERIM STORAGE MATERIALS

As discussed in Section 1, the materials used to construct most interim storage containers (i.e., austenitic stainless steels such as 304 and 316) are susceptible both to localized attack and stress corrosion cracking in chloride rich solutions. The goal of the work discussed here is to explore the susceptibility of these materials in terms of the extent of attack that can be supported under atmospheric conditions, where a bulk electrolyte is not present. Understanding the susceptibility of the materials to localized attack will provide considerable insight into the existence of potential SCC nucleation sites on the metal surface, as well as the extent of electrochemical activity (crevice corrosion, pitting, or SCC) that can be supported under such conditions.

3.1   Experimental methods

3.1.1   Materials

Stainless steel test coupons (UNS S30400) from a commercial vendor with dimensions 1" x 2" x 0.0625" and a 0.265" diameter centered hole were mechanically polished to a mirror finish. They were degreased using an alkali detergent and acetone and ethanol solvents, and were rinsed in deionized water and dried. The mirror finish was selected as it facilitates both the formation of a narrow crevice on the surface, as well as the identification of any corrosion that takes place upon completion of the test. Salt layers were deposited on the coupon surface by airbrushing a salt solution in a methanol carrier. ACS reagent grade chemicals were used for the 0.1M salt solution comprised of 50/50 NaCl/KCl and methanol. A region approximately 1.5 inches in diameter was masked on each coupon to define the deposition area via a template (i.e., a shadow mask), and a quartz crystal microbalance placed adjacent to the deposition region was used to monitor the quantity of material deposited. The resulting deposit was a relatively uniform film as shown in bottom half of the right image in Figure 38 . Figure 38 shows the salt deposition area on the left and a close-up view of the uniform salt layer on the right. In the right image, the top half of the salt layer was removed to show the contrast between the bare sample surface and the continuous salt layer deposited. Salt was deposited in 50, 100 and 200μg/cm^2 loadings for experimental evaluation.
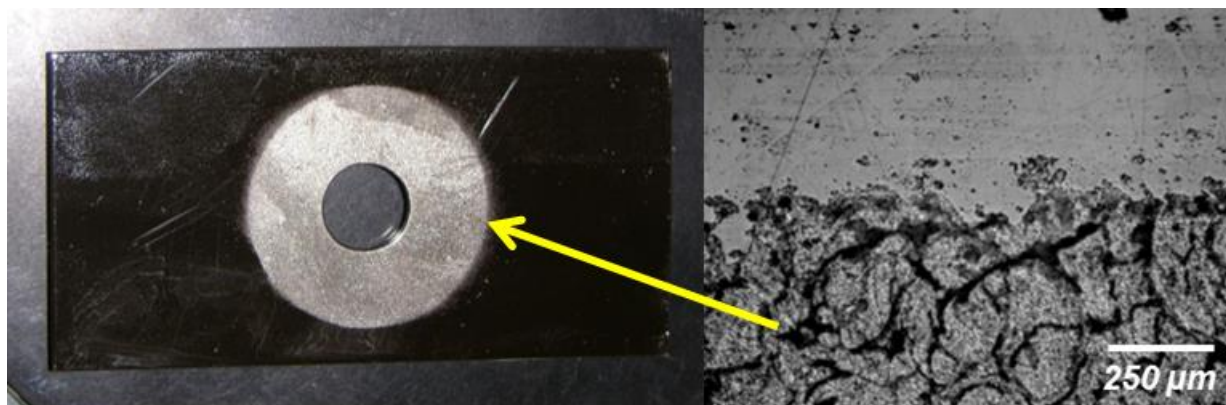

Figure 38. Sample coupon with salt deposit (L) and close-up view of salt layer (R).

3.1.2   Crevice former configuration

The established crevice corrosion test method for steel alloys in chloride-containing environments (ASTM 2001 [R 2012]) was used in developing the experimental protocol. A multiple crevice former assembly (MCA) was fixtured atop the deposited salt pattern on each test coupon. As depicted in Figure 39, the ceramic crevice formers are circular and have 12 radial teeth on the contact face. When in contact

with the sample surface the circumferential edge of each tooth produces an occluded environment enabling crevice corrosion to occur.

Titanium and PTFE fittings were used for fixturing the crevice former to the test coupon surface. The complete assembly is shown in Figure 40. All titanium hardware was electrically isolated from the sample coupon via use of a PTFE washer and by wrapping the titanium bolt thread length with PTFE tape prior to assembly. The crevice former teeth were wrapped in PTFE tape to provide better contact between each tooth and the sample surface. The assembly hardware was torqued to 70 in-lbs. The combination of coupon surface finish, PTFE wrapped MCA, and applied torque were based upon prior work that demonstrated this was the most aggressive manner in which to evaluate the potential for crevice corrosion initiation (Shan and Payer 2007).
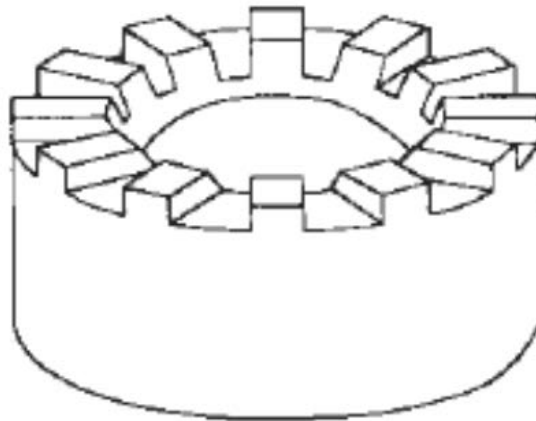

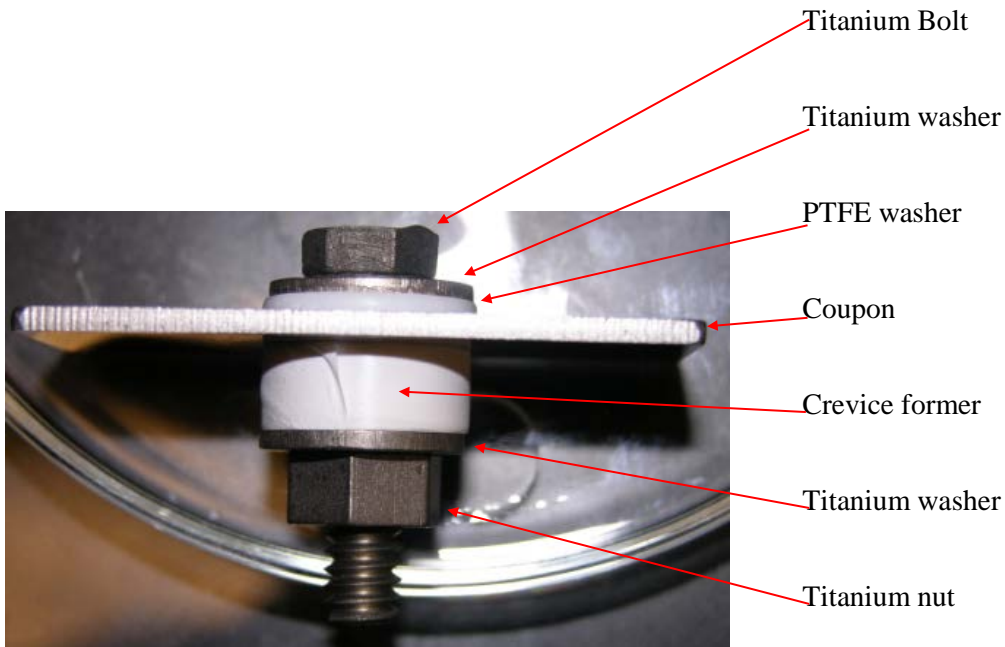Figure 39. Crevice former representation.

Figure 40. Complete assembly of crevice former on test coupon.

3.1.3   Dust deliquescence environmental chamber

A high-temperature, controlled dew point test chamber was used for environmental exposure (Figure 41). A gas stream (predominantly water as steam) was provided by utilizing a mass flow controller to feed liquid water to a steam generator. The gas flow rate through the chamber provided multiple environment exchanges per hour. Throughout each experiment, the conditions within the chamber were monitored via a series of thermocouples along with a chilled mirror. A bulk salt sample was placed in the chamber and monitored throughout test exposure to verify that a liquid brine was maintained and that little or no second phase precipitation was taking place (this could alter the brine composition). The assembled samples were placed on glass shelves within the test chamber as shown in Figure 42. Three replicates of each salt mass loading were exposed at 105°C, $T_d \approx 95$°C at time intervals of 7, 14, 25, 50 and 100 days.
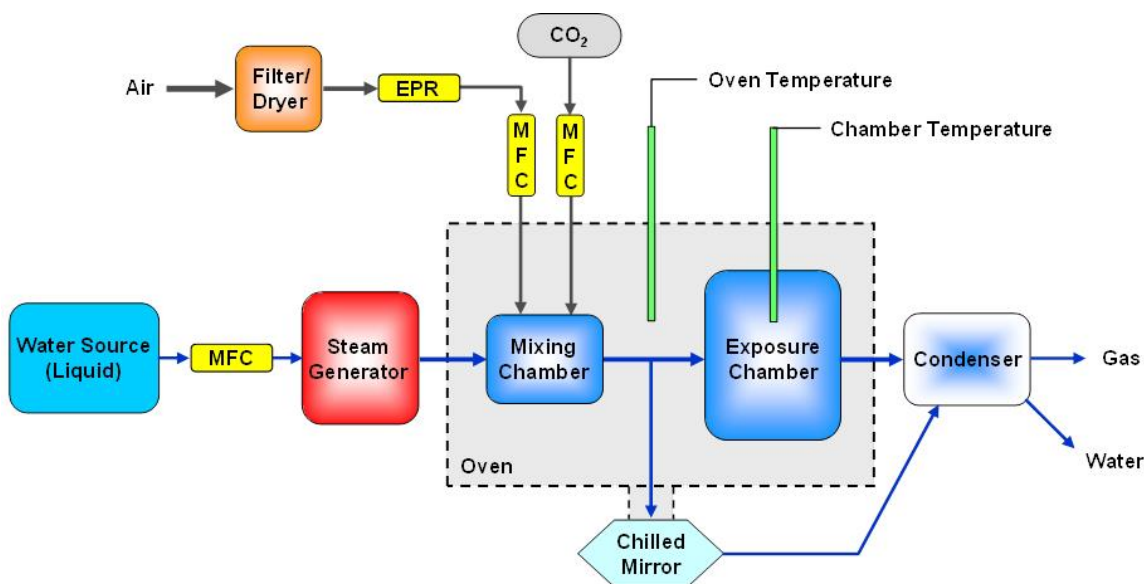
EPR = Electronic Pressure Regulator and MFC = Mass flow controller

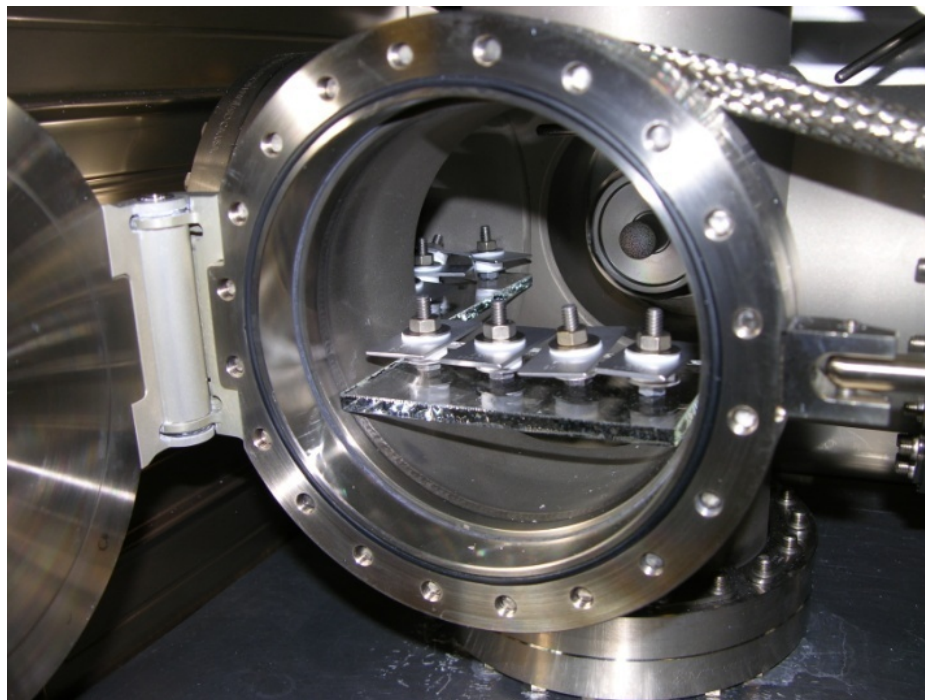Figure 41. Elevated temperature, high dew point exposure system.

Figure 42. Dust deliquescence chamber interior.

3.1.4   Samples post environmental exposure

The 304SS samples with three replicates of 50, 100 and 200 $\mu g/cm^2$ salt loadings were exposed for 7, 14, 25, 50 and 100 days. After removing the samples from the environmental chamber and allowing them to cool, the crevice former assembly was taken apart and the residual surface salt and metal oxides on the coupon were cleared away via sonication in distilled water. The post environmental exposure sample in Figure 8 was exposed for 7 days and had a 200 $\mu g/cm^2$ salt loading.

Figure 8. 304SS coupon with 200 $\mu g/cm^2$ and 7 day exposure after crevice former removal (L) and rinsing (R).

3.1.5   Crevice corrosion survey methods

A complete survey of the edge around each tooth was conducting using SEM imaging. Images were taken around the circumferential edge of each tooth in the pattern shown in Figure 43. The outer circle is the edge of the salt coating. The first three teeth are outlined; even in SEM images the tooth edge, and therefore the area where crevice corrosion can occur, was usually apparent. These images were used to conduct a thorough survey of the extent of crevice corrosion on all teeth in each sample. A SEM image with a tooth over view is shown in Figure 44, and Figure 45 has a higher magnification image of corrosion attack on the crevice former tooth edge. Figure 43 shows clearly the outline of the crevice former tooth, with fairly substantial attack present along the top long edge. Most sites are smaller and require higher magnification as represented in Figure 45. In Figure 45 the general location of the crevice former tooth edge is show in red and a site is highlighted in yellow. The area of each site was estimated by fitting an oval of approximate area to the site as in Figure 46. The presence of very shallow surface etching under the tooth face, and in some cases along the edge, is common and present to varying extent in all samples. This surface etching, or mottling, is the possible result of high localized attack independent of the intended crevice corrosion occluded environment. The location of the tooth edge is important as it the location where the occluded geometry is created for crevice corrosion. Even with a general tooth edge outline visible on most SEM images the exact location of tooth edge cannot always be identified. It is also not apparent how far inward or outward from the visible tooth edge pattern on the sample an occluded environment exists. For surveying crevice corrosion sites throughout the sample images a general rule of approximately ±100 μm around the tooth contact edge was followed in identifying valid sites.
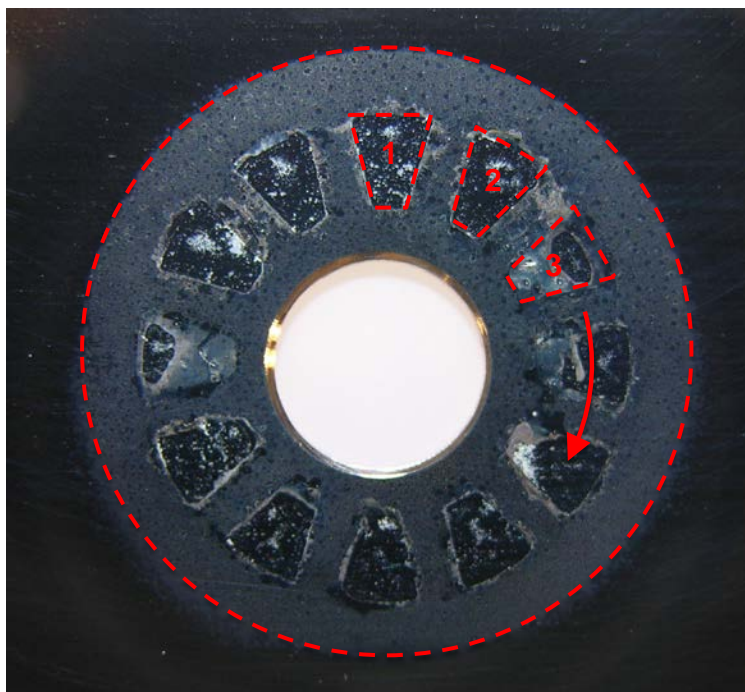

Figure 43. Crevice corrosion site survey location and pattern.
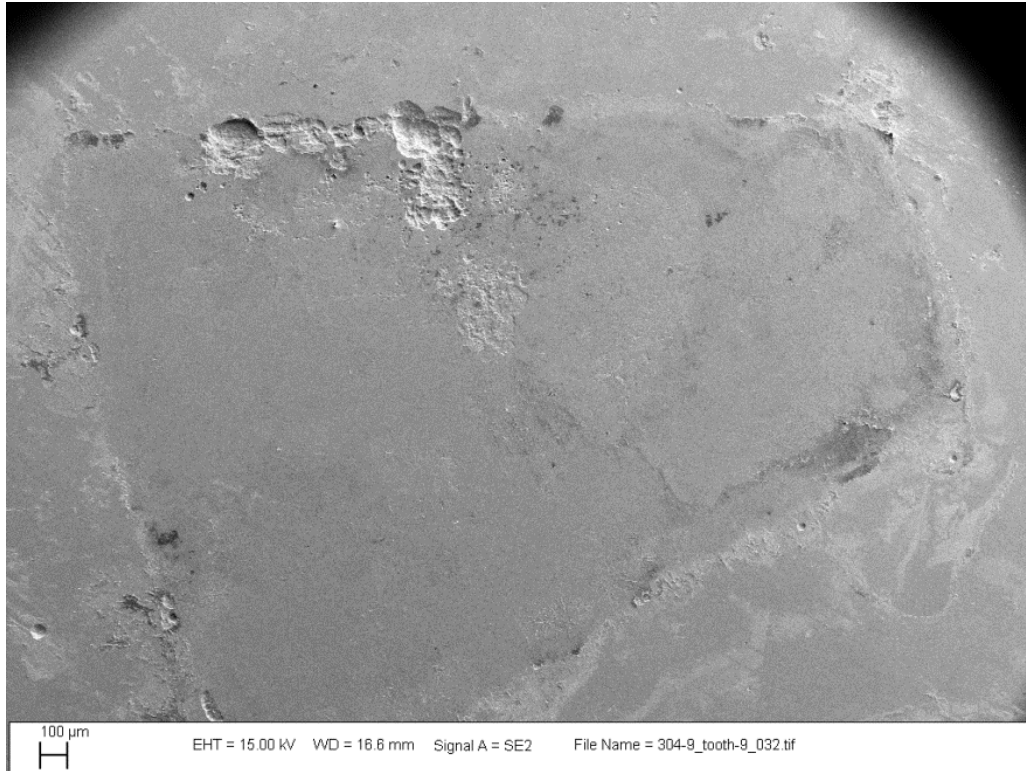
Figure 44. Tooth outline from sample with 100μg/cm^2 salt and 100 days exposure.
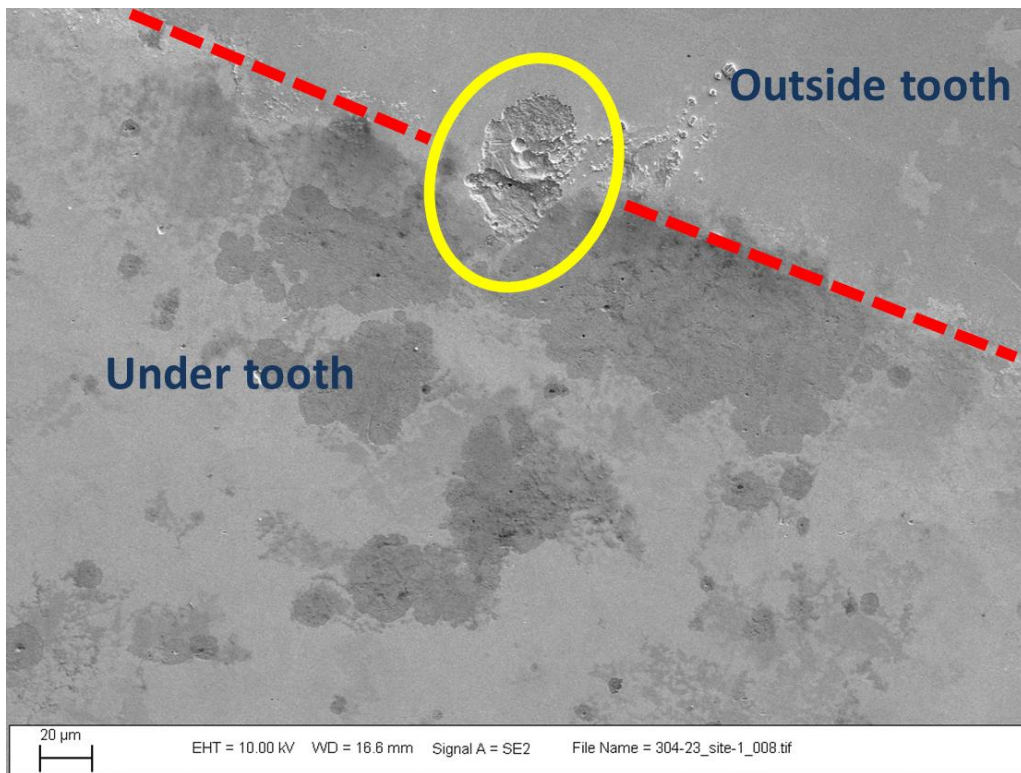

Figure 45. Crevice corrosion in sample with 100μg/cm^2 loading and 50 days exposure.
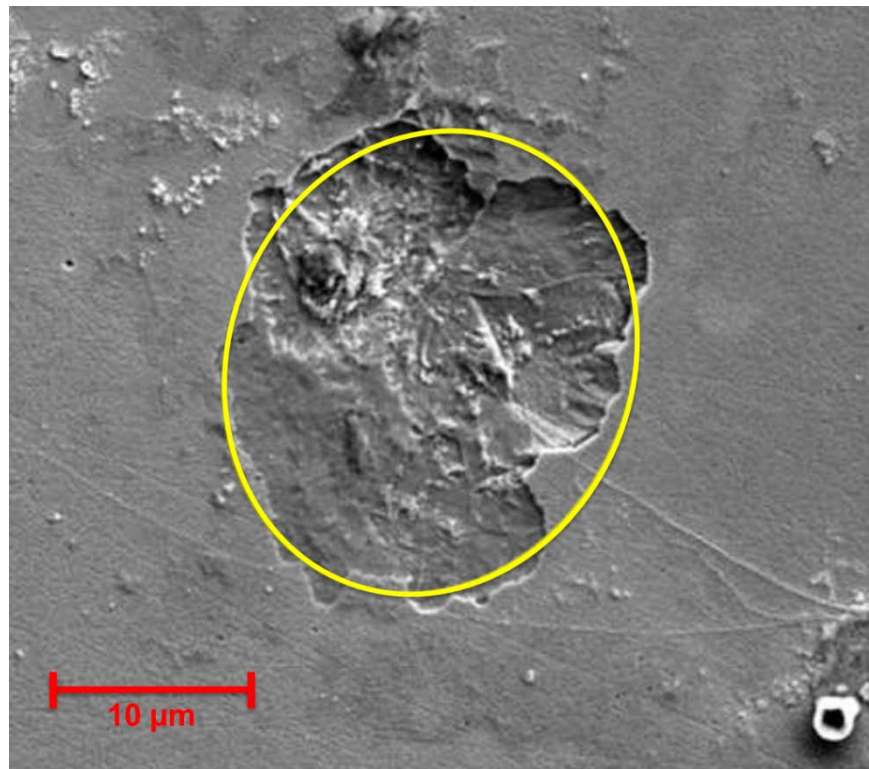
Figure 46. Example of estimating area of a crevice corrosion site.

For each sample set of SEM images the following surface observations were recorded. The area of each valid site generated from crevice corrosion was estimated by fitting an oval of approximate area to the site. The site was categorized and described for the extent of attack. Sites were labeled as very shallow, shallow, moderate depth, deep and extremely deep using a qualitative assessment of site depth. These characterizations will be quantified more completely through the use of laser confocal microscopy, where representative images will be used to extract average depth values for each category of attack. Figure 47 and Figure 48 show examples of how crevice corrosion sites were characterized: Figure 47 has examples of very shallow, shallow and moderate sites while Figure 48 shows deep and extremely deep sites.
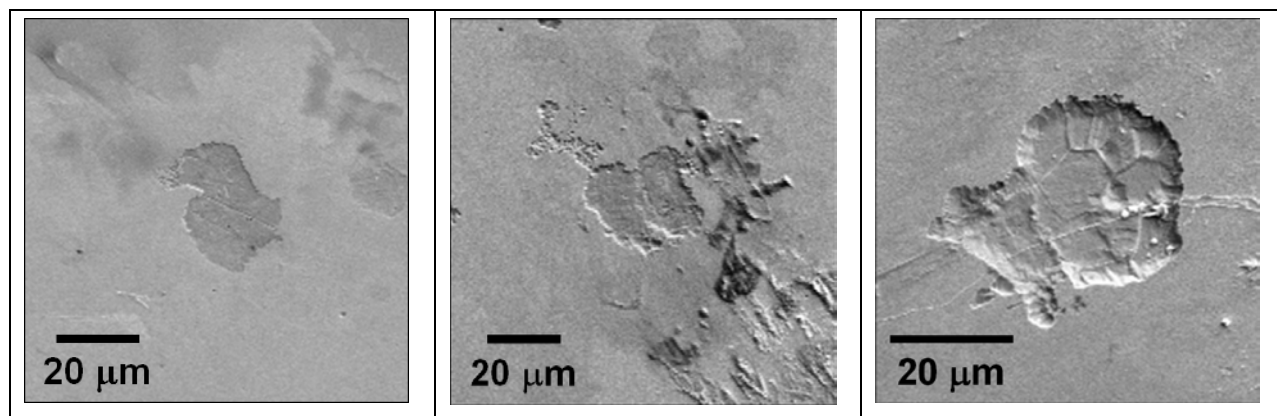

Figure 47. Crevice corrosion sites characterized as very shallow (L), shallow (M), and moderate (R) in depth.
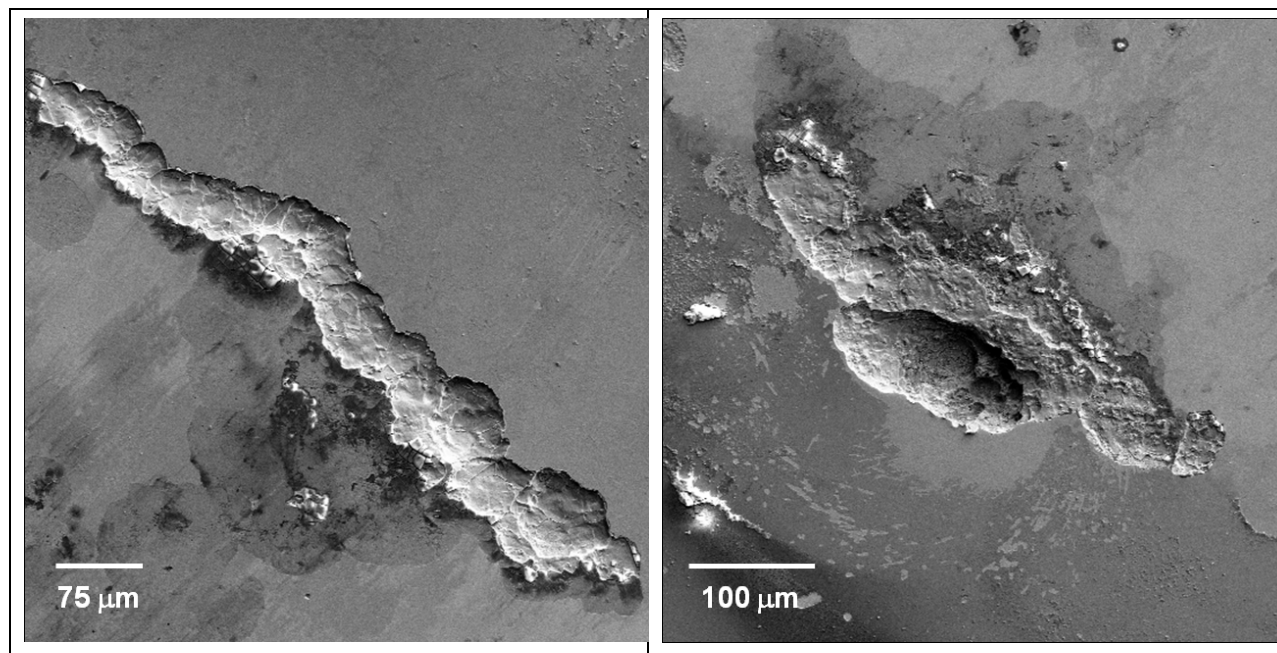
Figure 48. Deep and extremely deep crevice corrosion sites.

The surface roughness was noted as uniform, mild or moderate. Pitting and pit size within each site were also noted. Surface cracking along the edge of a site or within the site were also noted. Any features of note, such as a crack, crevice, plateau or extreme meandering of attach was also noted. The state of the sample surface around the sites was also noted, i.e. pitting, very shallow surface etching and cracking. The overall appearance of each tooth was also noted. In some cases it appeared contact with the sample surface was apparent for only a portion of the tooth area—see Figure 49. Occasional absence of complete tooth surface contact was observed throughout all samples and is expected to be uniformly average throughout the sample population. In the case of unclear tooth surface contact, the entire area in question was treated as being an occluded environment and all sites within were counted.
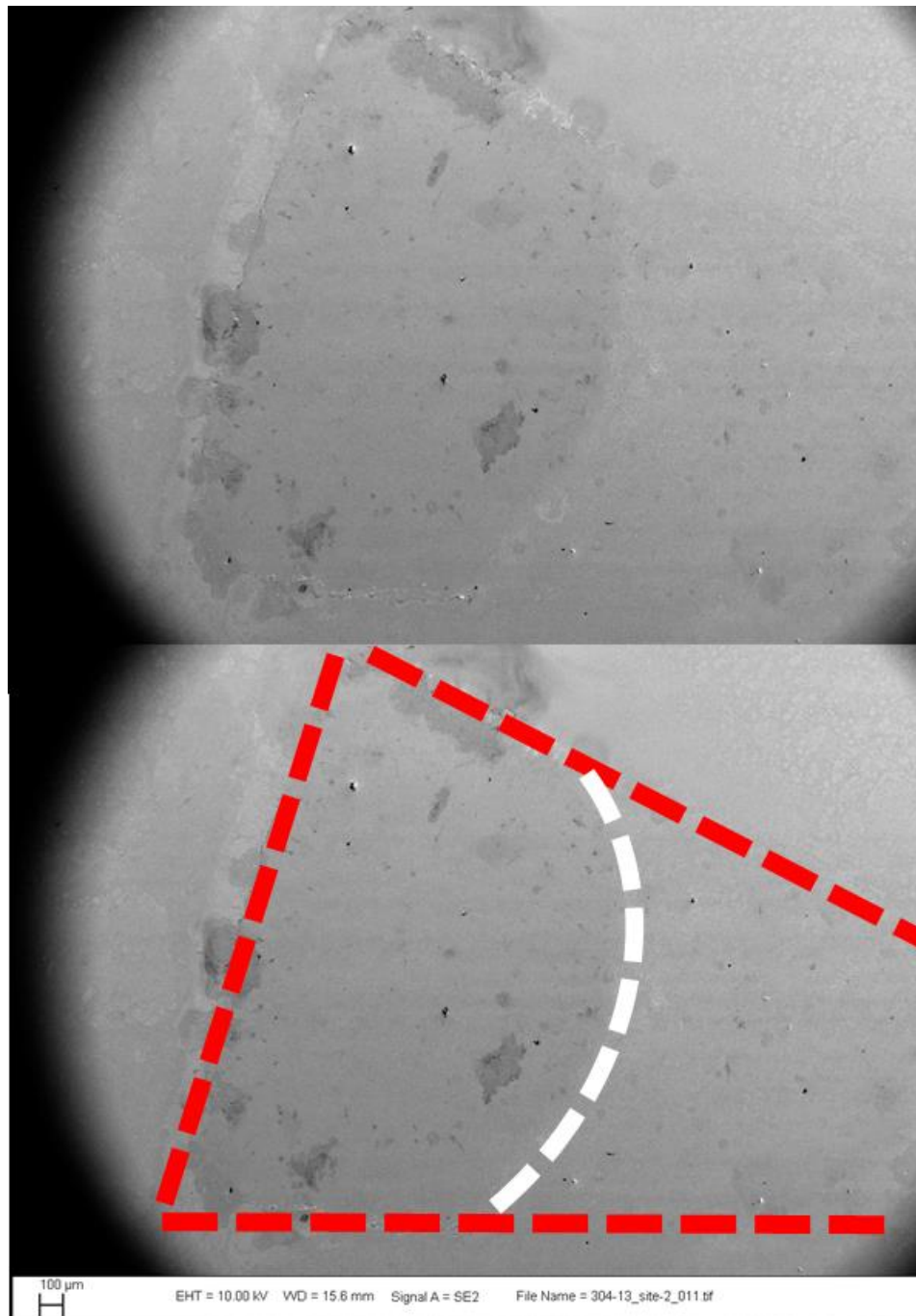
Figure 49. Apparent non-uniform contact of crevice former tooth on sample 304-13 (200ug/cm^2, 14 days exposure).

3.2   Crevice site survey results and analysis

During the crevice corrosion site survey process, it became apparent there were numerous features on the samples surface that, while their origin was corrosion, could not be attributed to the crevice attack that dominated each specimens response. As such, these sites could be omitted from formal consideration as actual crevice corrosion sites during the initial evaluation. These include lightly etched or mottled areas

and pitting, as it is plausible either feature was formed from direct attack of the surface independent of an occluded environment. Part way through the survey, crevice corrosion sites categorized as very shallow were also disregarded. There were a significant number of very shallow sites, and in addition them being difficult to distinguish from mottling sites, the very small volume of material removed has less impact on the total amount of corrosion product removed from the surface. While these features weren't included in the data analysis, their presence was noted for future consideration. Variability in both total crevice corrosion site area and number of sites from tooth to tooth was observed in all samples. Variation in crevice former tooth surface contact (i.e. Figure 15) due to neither the crevice former nor the 304SS sample coupons being perfectly flat has likely contributed to this distribution. To evaluate the distribution of sites and crevice corrosion area across all teeth within a given sample, the number of sites or total area per tooth is sorted and plotted from smallest to largest. As it is likely the variability in surface area contact is similar from sample to sample, it isn't expected to skew the resulting data to any significant degree.

3.2.1   Number of crevice corrosion sites

The number density of crevice corrosion sites corresponds to the total sites per sample – each site is counted only once, irrespective of its magnitude. Minimal correlation between number of sites and either loading or exposure time was observed. The total number of sites per coupon as a function of exposure time is shown in Figure 50. There is no correlation between exposure time and salt loading for 7, 14 and 25 days. There is a general trend of increasing number of sites for exposures of 25, 50 and 100 days, but not as a function of loading. The fewer number of sites for longer exposure times is likely the result of sites coalescing over time into fewer (and larger) sites. Below are figures showing the number of sites per tooth for each sample as a function of both loading and exposure time. Figure 51, Figure 52, and Figure 53 show the number of sample sites as a function of exposure time for 50, 100 and 200 $\mu g/cm^2$ respectively. Note that while only half of all samples have been surveyed, all replicates are included in all plots. For example, in Figure 53, two samples with 14 and 25 days of exposure were surveyed. The 7, 25, and 50 days samples with 50 200 $\mu g/cm^2$ loadings (Figure 51) have a similar number of observed sites. The 100 day sample has a considerably larger number of sites, indicating the longer time frame may have allowed for more sites to initiate. The 14 day sample has more sites per tooth than any other sample. The samples with 100$\mu g/cm^2$ loading do not show a discernible correlation between number of sites and exposure time.

While the observation that some of the samples with longer exposure times have fewer sites seems counterintuitive, there are a couple possible explanations. Recall that in the counting of sites, all sites are treated equally, irrespective of their magnitude. With increasing time, an crevice corrosion site has more time to expand and if the aggressive species, such as chloride, are sequestered by the corrosion product, may consume all available reactant and may be larger than a site where corrosion was stopped before reactant consumption was complete. Longer exposure times also allow more opportunity for site initiation, and there may be more sites for this reason. Having more and larger sites from long exposure times can allow for coalescing of sites, and as the average site area has yet to be considered (on a per site basis), fewer sites for long exposure samples may result from large or more sites coalescing into fewer and considerably larger sites. The 200$\mu g/cm^2$ loading samples (Figure 53) show a similar trend. With the exception of a couple teeth, the 25, 50 and 100 day samples have fewer sites per tooth.

Correlation between number of crevice corrosion sites and salt mass loading was not observed. Figure 54, Figure 55, and Figure 56 shows the number of sites per tooth for each exposure time.
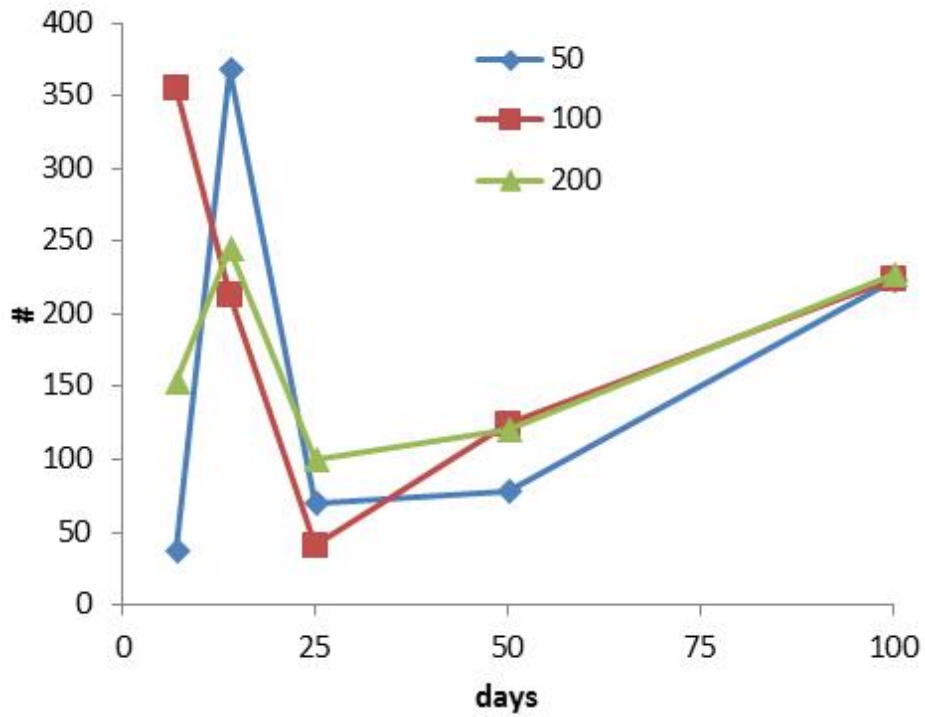
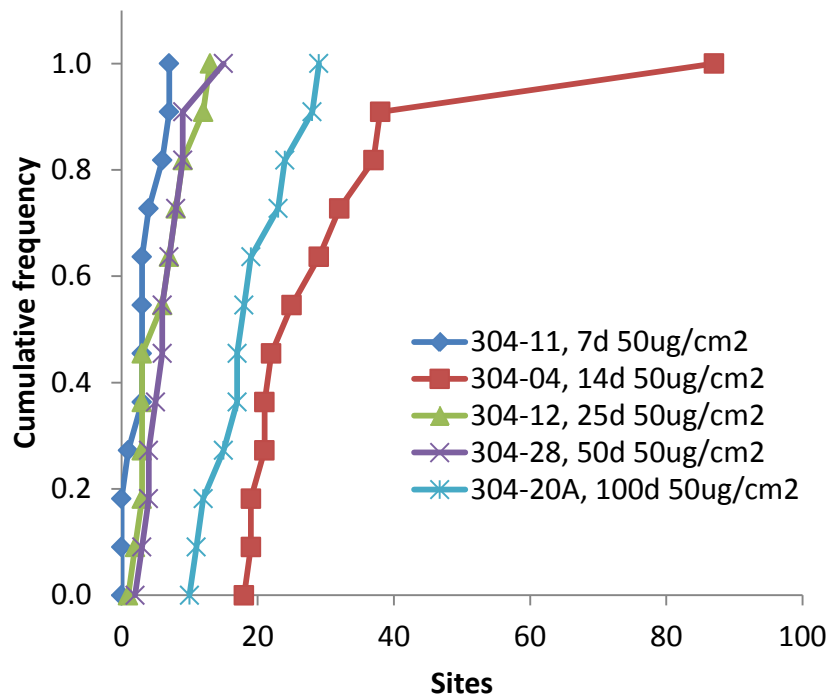Figure 50. Total sites per sample over time(loadings in μg/cm^2).

Figure 51. Crevice corrosion sites per tooth over time with 50μg/cm^2 salt loadings.
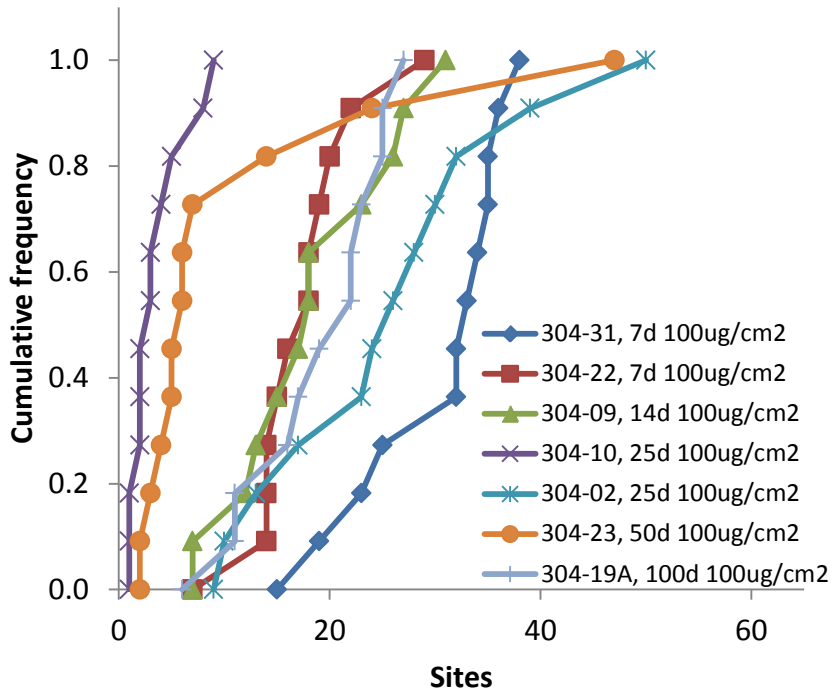
Figure 52. Crevice corrosion sites per tooth over time with 100μg/cm^2 salt loadings.
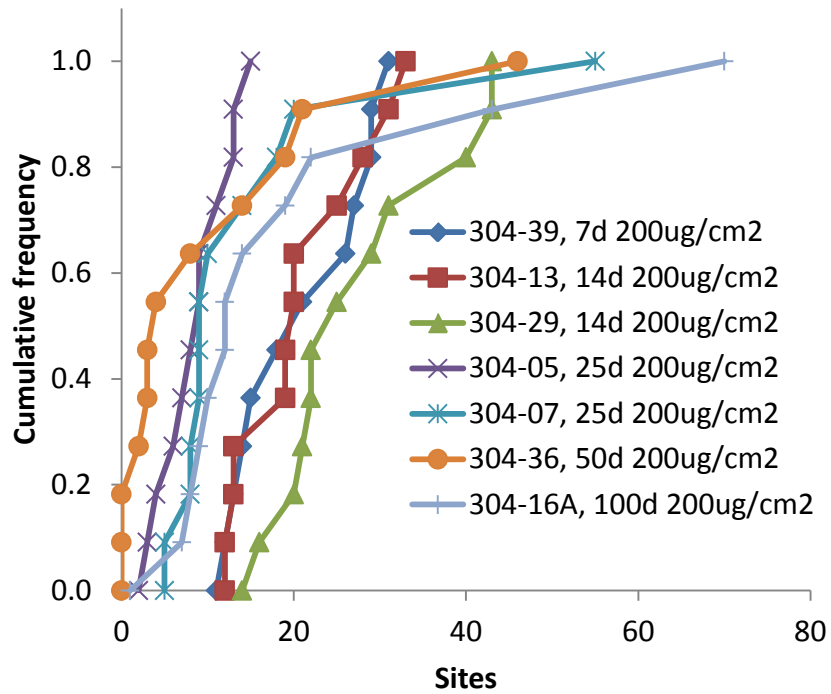

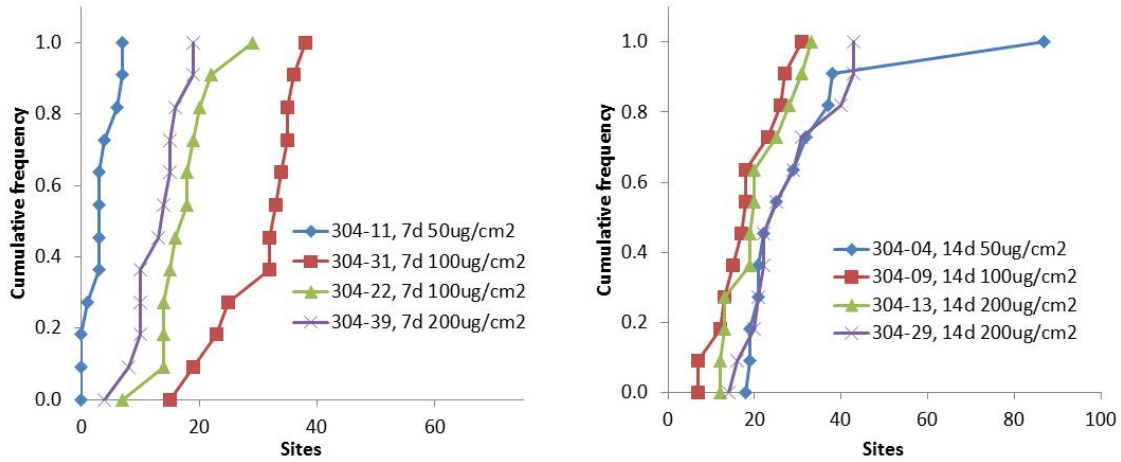Figure 53. Crevice corrosion sites per tooth over time with 200μg/cm^2 salt loadings.

Figure 54. Number of sites per tooth as a function of salt loading for 7 day (L) and 14 day (R) exposure times.
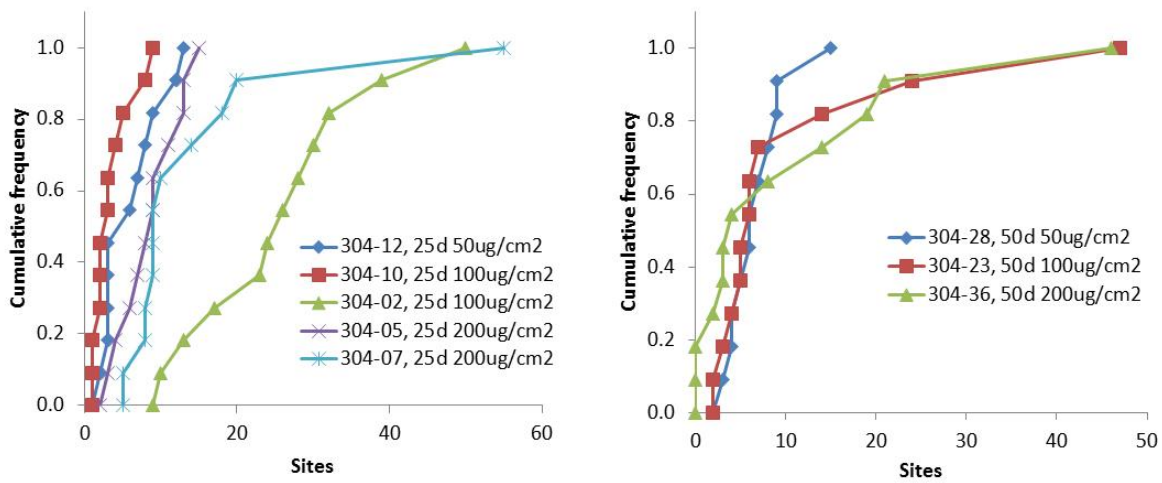

Figure 55. Number of sites per tooth as a function of salt loading for 25 day (L) and 50 day (R) exposure times.
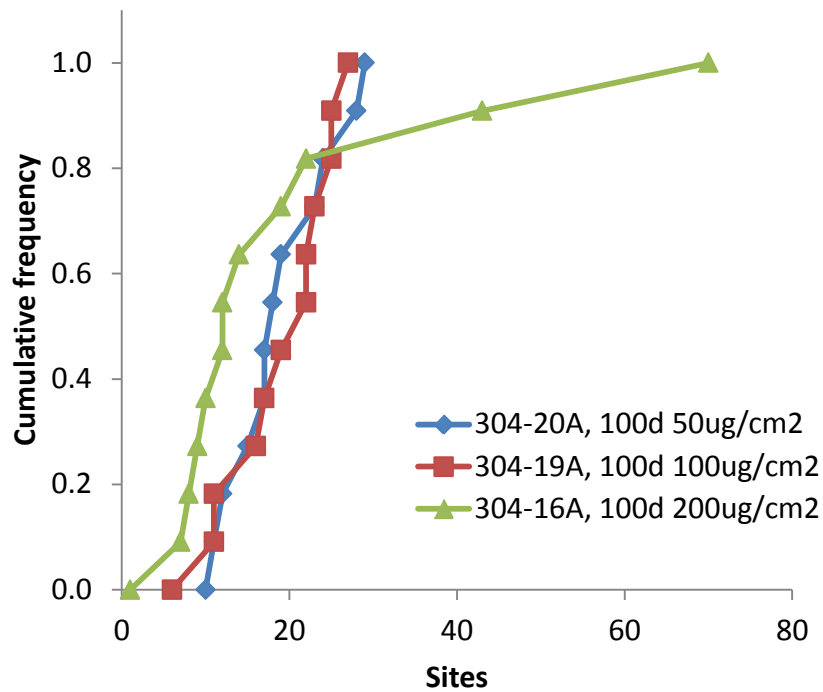
Figure 56. Number of sites per tooth as a function of salt loading from 100 days exposure.

3.2.2   Area of crevice corrosion sites

Given the impracticality of measuring each and every crevice corrosion site across all sample coupons with a depth profiling technique such as laser confocal microscopy or white light interferometry, a comprehensive survey of the observable area of crevice corrosion sites was used for evaluation. It should be noted that the true extent of corrosive attack is most accurately measured via volume of removed material, and for this reason the qualitative degree of corrosive attack (shallow, moderate, deep) was noted in an effort to get a better representation of the crevice corrosion on the sample coupons.

The total area of sites counted on each coupon is shown in Figure 57. With the exception of the 7 day exposure samples, a general trend of increasing area with increasing salt load is observed for all exposure times. In addition to confirming a uniform salt particle distribution, this shows the crevice corrosion technique employed is a valid method of discerning the extent of attack of a given quantity of surface salt deposition.
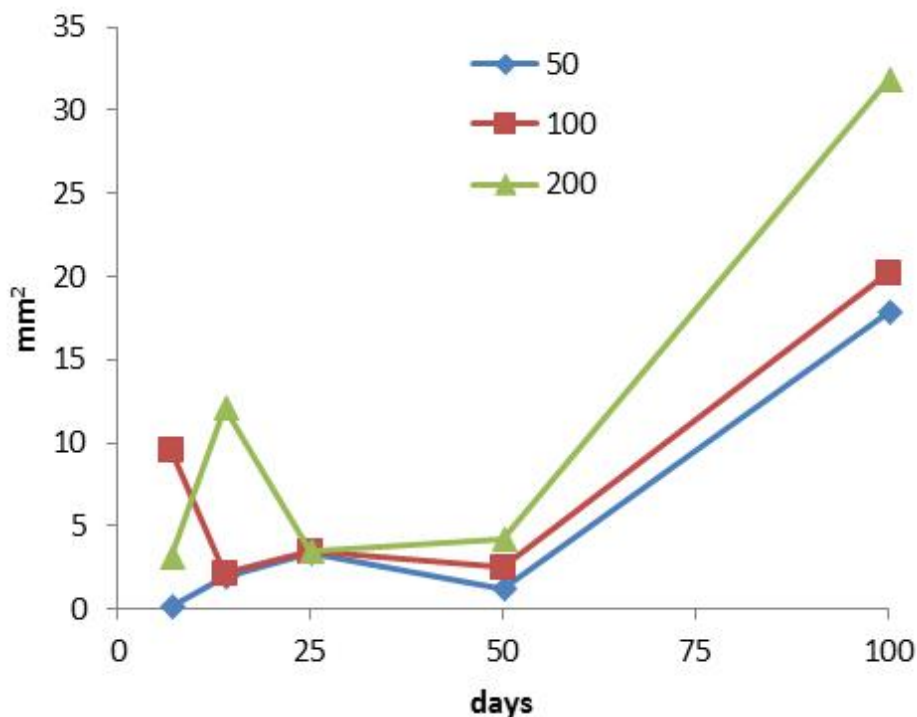
Figure 57. Total area of observed crevice corrosion sites per sample over time (loadings in $\mu g/cm^2$).

Figure 58, Figure 59, and Figure 60 show the total crevice corrosion per tooth for all exposure times evaluated. It should be noted that while the entire surface area is counted, the depth of attack is not – thus a large relatively shallow site would have a greater 2-D area than a smaller, but much deeper, site. This could result in the shallow site being emphasized more than the deep site, even if the total quantity of material removed for the deep site was much larger than the shallow one.

While the seven day exposure samples (Figure 58) have the greatest exposure area from $100\mu g/cm^2$ salt loading, the fourteen day samples show a general trend of increasing area with increasing exposure. When looking at crevice corrosion area per tooth in the 25 day samples (Figure 59) there is no apparent correlation between salt loading and exposure time. Examining the data trends in Figure 59, there appears to be no change in average area at all due to varying salt concentration. The 50 day exposure samples show a reasonably clear trend between increasing salt loading and crevice corrosion area for individual teeth. The 100 day exposure samples (Figure 60) also show a clear trend of increasing area per tooth as a function of increasing salt loading.
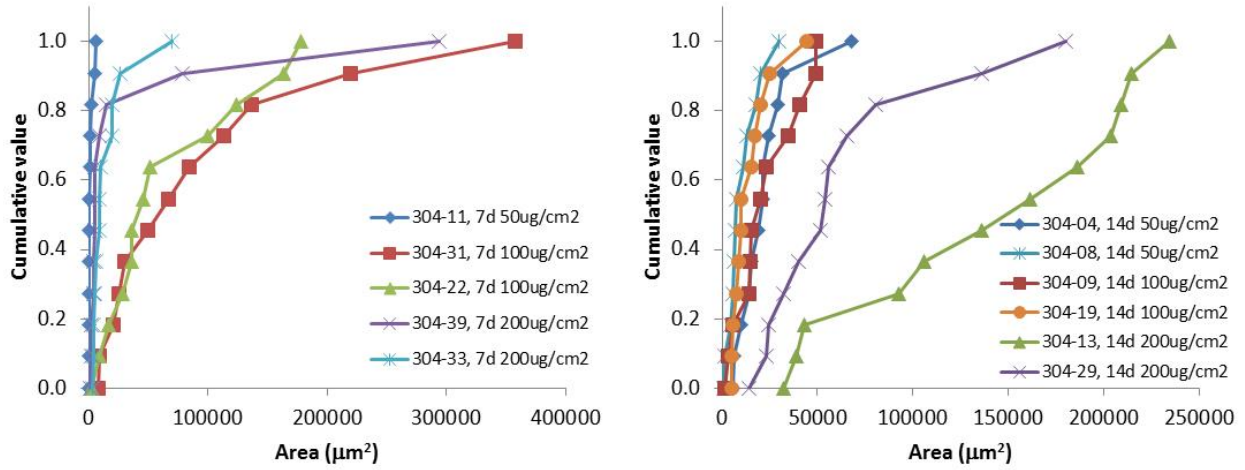
Figure 58. Total crevice corrosion area as a function of salt loading for 7 day (L) and 14 day (R) exposure times.
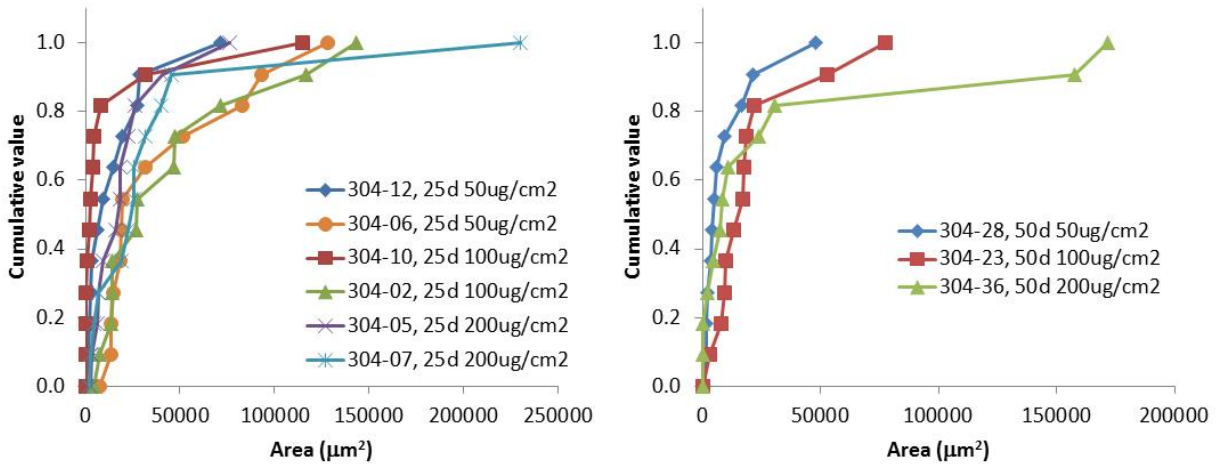

Figure 59. Total crevice corrosion area as a function of salt loading for 25 day (L) and 50 day (R) exposure times.
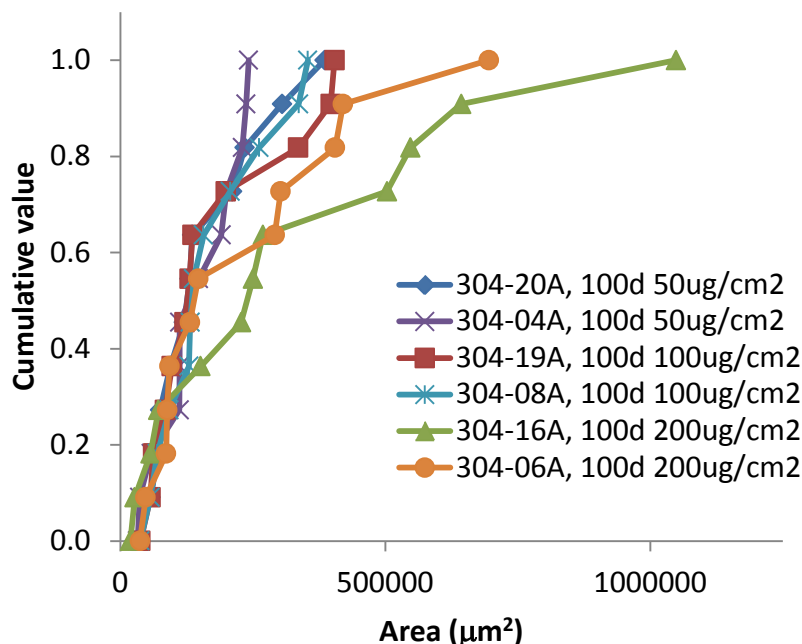
Figure 60. Total crevice corrosion area as a function of salt loading from 100 days exposure.

Figure 61, Figure 62, and Figure 63 show the measured crevice corrosion area per tooth as a function of time for 50, 100 and 200μg/cm^2 loadings respectively. The onset time of crevice corrosion was not observed as the first time interval observed (7 days) already showed measurable attack. There is very little correlation between tooth corrosion area and exposure time for the 7, 14, 25 and 50 day samples for all three loadings. In addition, there is apparent variability in both the average tooth area and total area between replicate samples. For examples, the 25 day samples with 100μg/cm^2 loading in Figure 62 (both green lines) have different observed areas. Marked difference in area are also apparent in the 7 day samples with 100μg/cm^2 loading (Figure 62), the 25 day samples with 50μg/cm^2 loading (Figure 61) and the 14 day samples with 200μg/cm^2 area (Figure 63). It isn't clear if additional sample data would prove useful. There is a possibility that some variability in the data could be the result of using different sample coupon lots. It is also possible that there is too much variability in the crevice corrosion phenomenon in the first 50 days using this experimental setup to isolate and identify any meaningful trends.

Between any of the shorter environmental exposure times and 100 days there is a definite increase in crevice corrosion surface area. As a time interval of no less than 50 days is the apparent minimum necessary to observe a difference in corrosion surface area, it is possible either too much reactant or too little exposure time was used in this set of experiments. While there is no apparent corrosion stifling in the time period observed, it is not clear if this observation is due to an insufficiently long time interval for the experiments reported here or if stifling simply does not occur under these conditions, or if some other factor were determining the response.
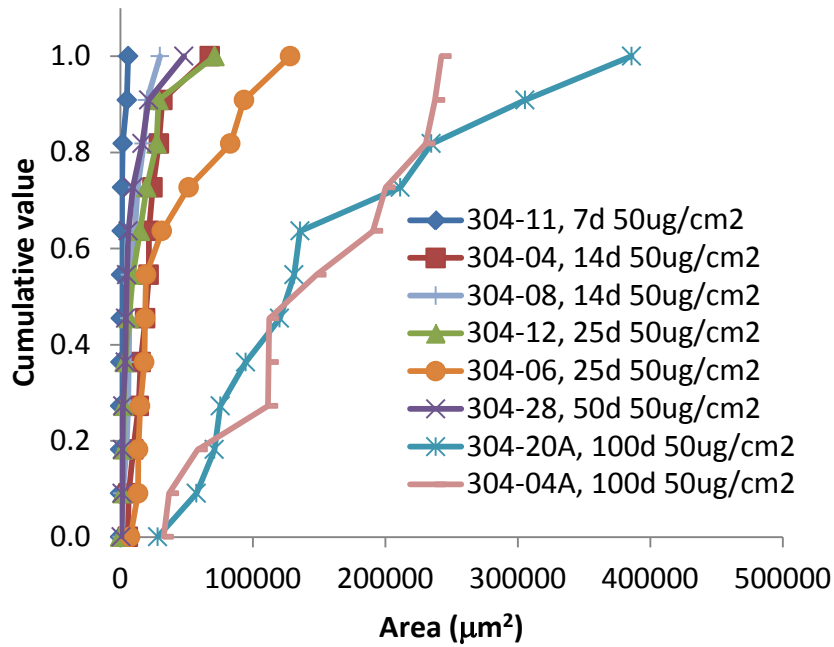
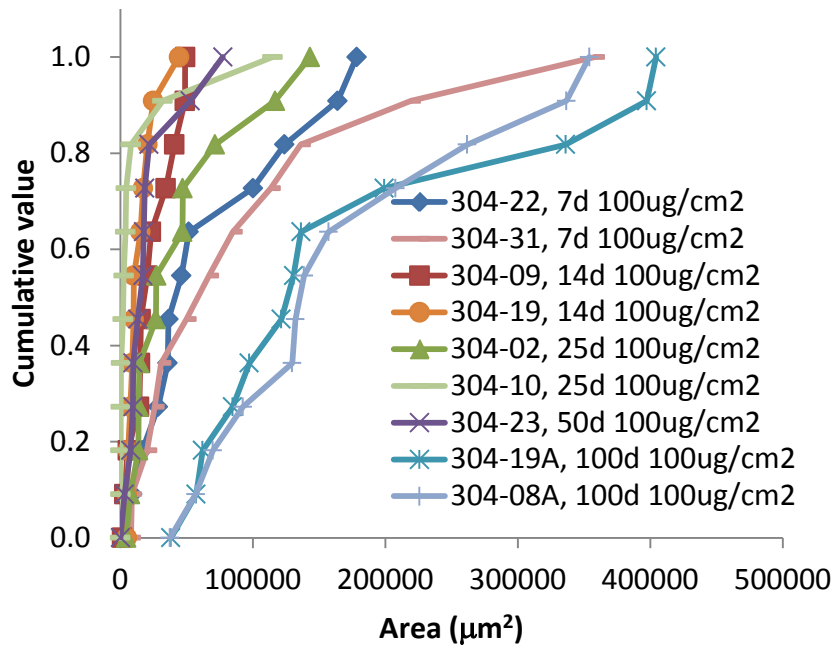Figure 61. Crevice corrosion area per tooth over time from 50μg/cm² salt loading.

Figure 62. Crevice corrosion area per tooth over time from 100μg/cm² salt loading.
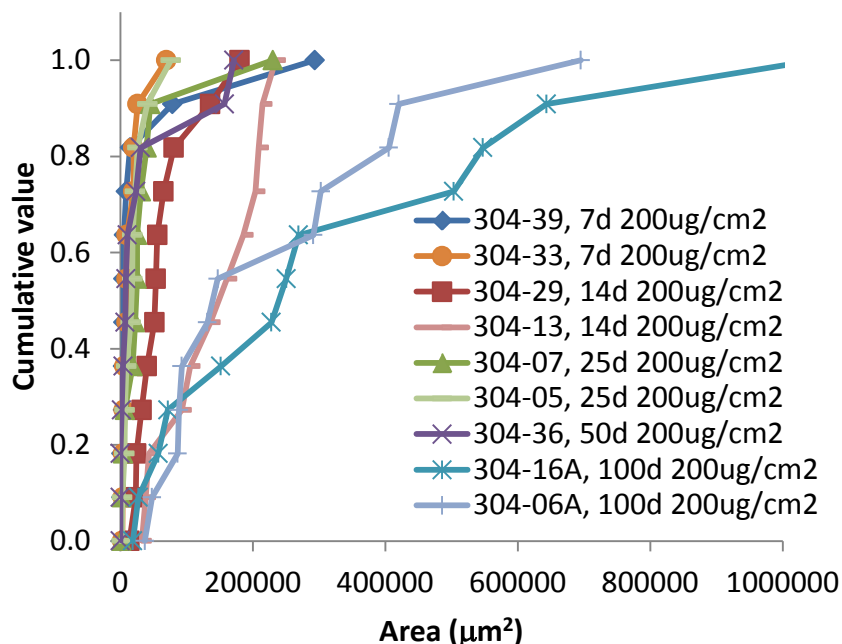
Figure 63. Crevice corrosion area per tooth over time from 200μg/cm^2 salt loading.

Figures 64-71 show the percentage of site type compared to the total measured area. Site types included are shallow, moderate and deep (extremely deep sites are included in the deep category). See Figures 13 and 14 for examples of each site type. Deep sites are representative of the most severe attack by volume, followed by moderate and shallow sites. Without knowing the volume of the corrosion sites, it is possible that shallow sites may be representative of very little volume loss and may not contribute substantially to total amount of crevice corrosion that occurred. Figure 64, Figure 65, and Figure 66 show that the percent of aggressive attack increases as a function of time for all three salt loadings. Regardless of how much total corrosion area was observed for each sample, these trends show convincing evidence that more aggressive attack corresponding with more volume loss is observed with increasing exposure time. This trend could be quantified using the volume of each site type. Without the actual volume values it isn't clear if there is a distinct trend of increasing total volume loss as a function of exposure time throughout the 7-100 day time frame. Figures 67-71 show the percentage of site type with varying salt loading. When considering the entire set of figures there is little correlation between salt loading and the site type. This may indicate there was insufficient time for available reactant in a particular site to be consumed, and either longer test times or significantly less reactant are necessary to demonstrate stifling.

Figure 64. Percentage of corrosion area as a function of site severity for 50μg/cm^2 samples.

Figure 65. Percentage of corrosion area as a function of site severity for 100μg/cm^2 samples.

Figure 66. Percentage of corrosion area as a function of site severity for 200µg/cm^2 samples.

Figure 67. Percentage of corrosion area as a function of site severity for 7 days exposure.
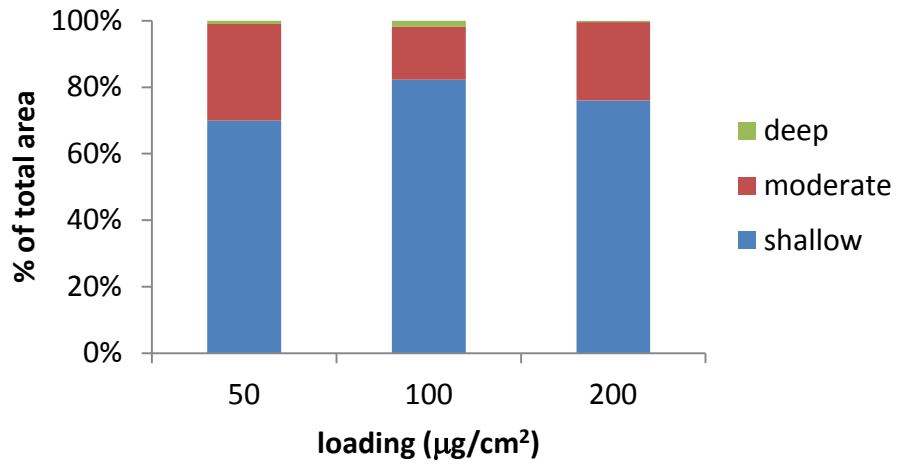
Figure 68. Percentage of corrosion area as a function of site severity for 14 days exposure.
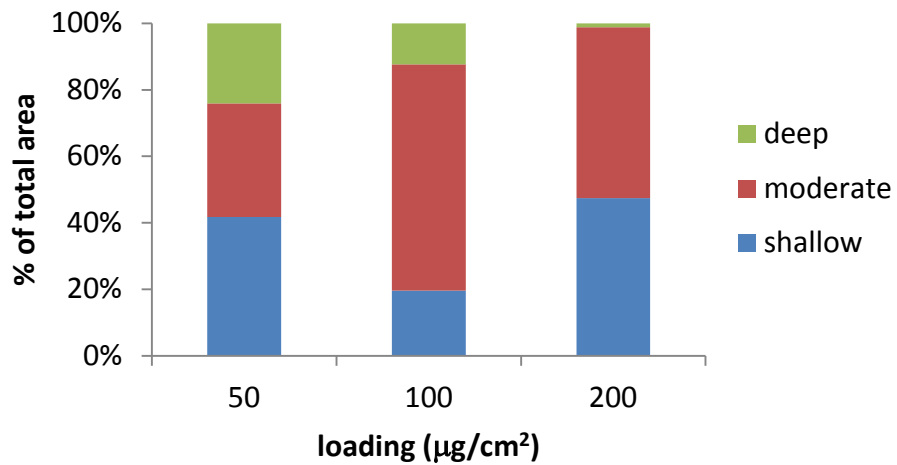
Figure 69. Percentage of corrosion area as a function of site severity for 25 days exposure.
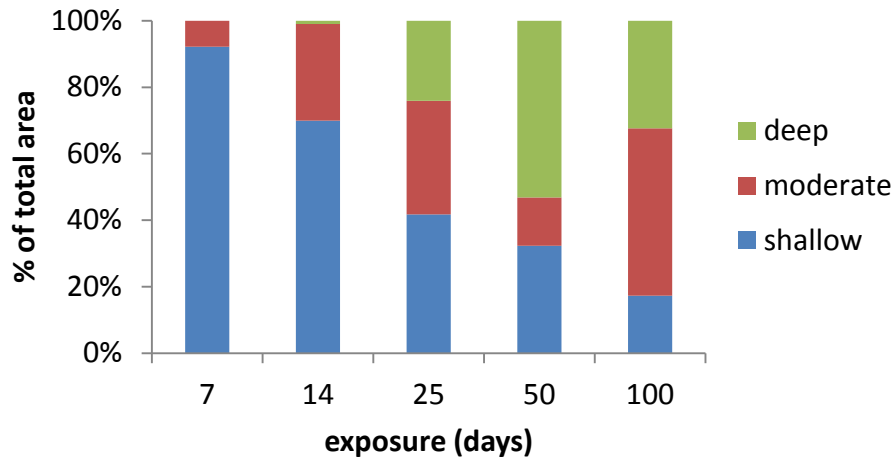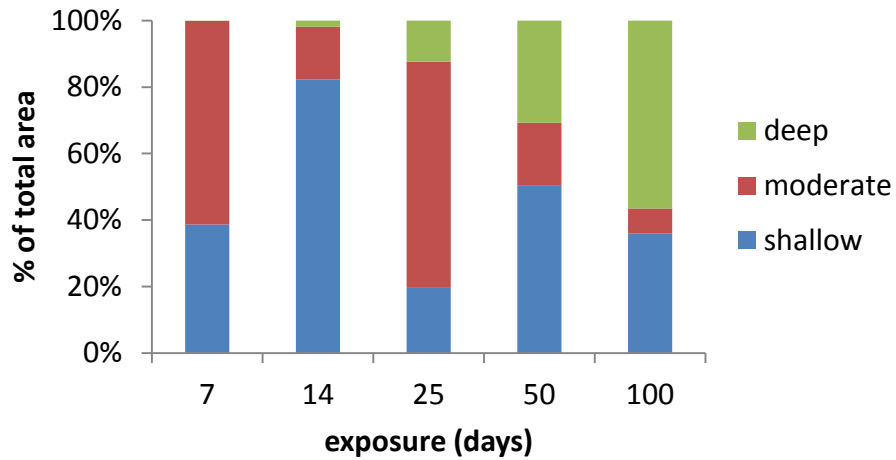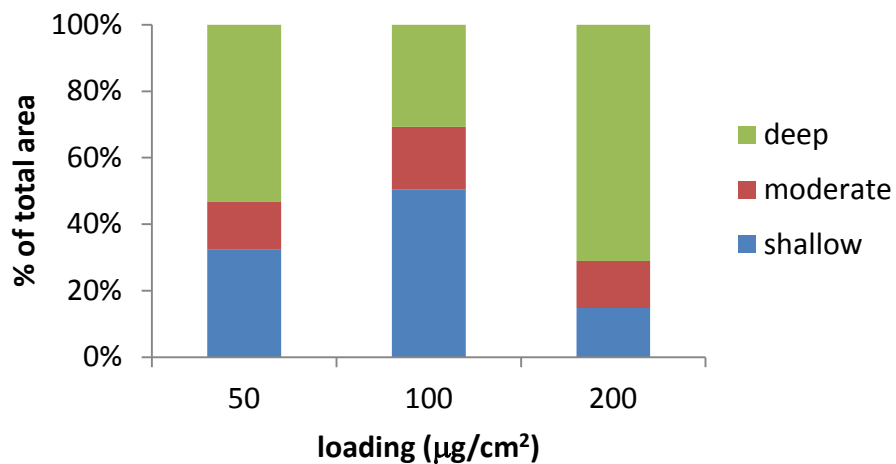
Figure 70. Percentage of corrosion area as a function of site severity for 50 days exposure.

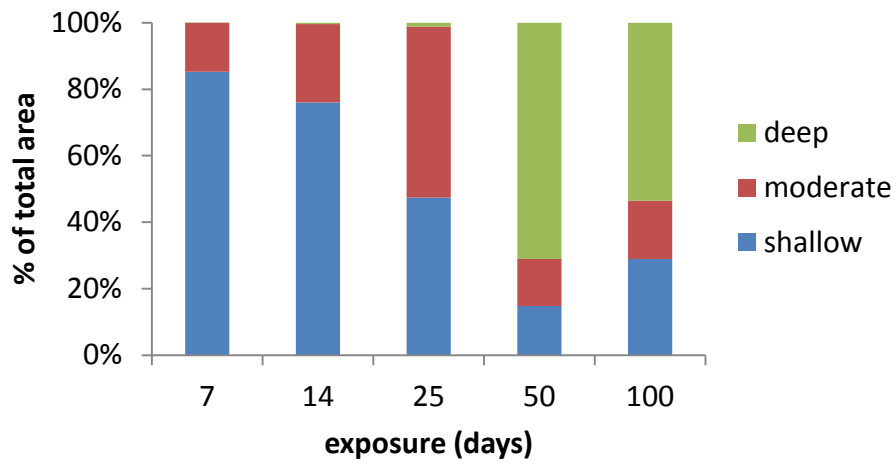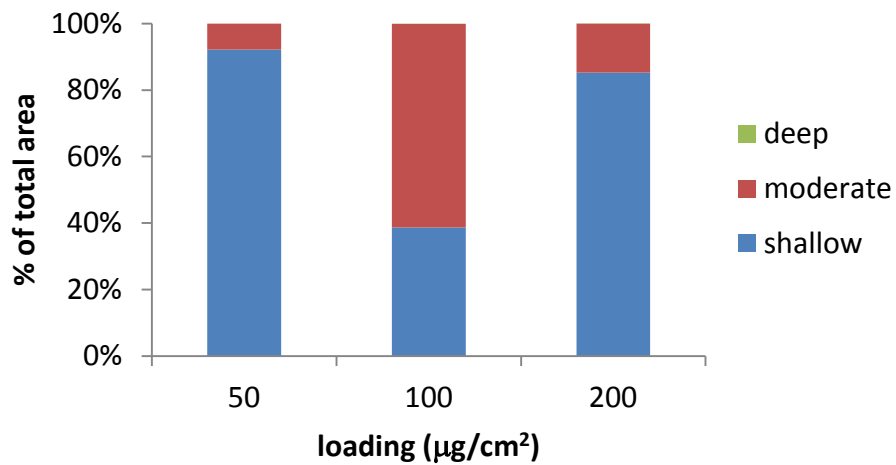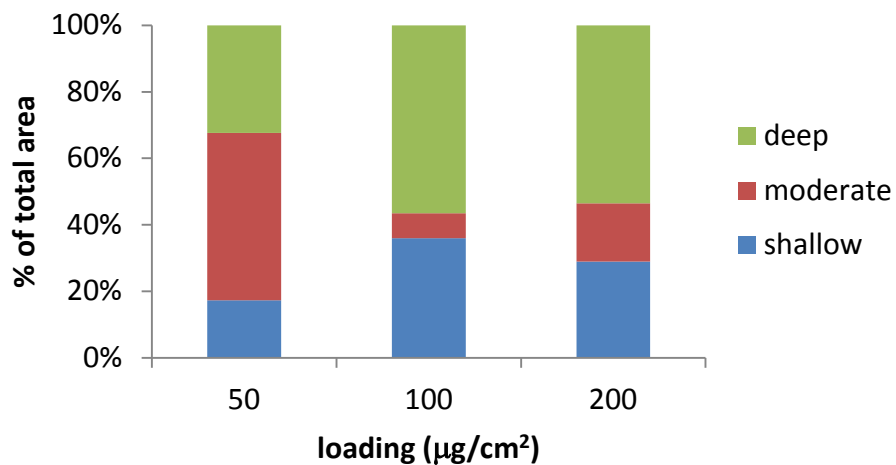Figure 71. Percentage of corrosion area as a function of site severity for 100 days exposure.

3.3 Summary and Future Work

A comprehensive review of the number density and two dimensional surface area of corrosion sites has revealed that neither measurement, in and of itself, can satisfactorily explain the observed trends. As such, a third dimension (i.e., depth) will be added to the existing measurements to see if a trend becomes more clear. By adding depth, the reported results will be more like a volume of material, corresponding to the actual degree of attack that has taken place. This observation is closer to the actual anodic activity (and hence cathodic activity) that led to the observed response. Looking at the data, there is a clear discontinuity in the degree of attack reported at 50 days and 100 days. As such, the performance of a subset of experiments at times bracketing 100 days (perhaps 75 days and 150 or 200 days) will be considered.

4. CONCLUSIONS

This progress report describes work done at Sandia national Laboratories (SNL) to assess the localized corrosion performance of container/cask materials used in the interim storage of used nuclear fuel. A detailed evaluation of the environment to which these storage systems are exposed is included to provide context for the experimental evaluation of the effect of deliquesced salts on storage-relevant steels. The results of dust deliquescence testing on 304SS obtained to date are presented and evaluated regarding feasibility of stifled localized corrosive attack.

Salt deliquescence can occur on interim storage containers only over a small part of the temperature and RH range that the storage containers will experience. A reasonable maximum possible absolute humidity is 40-45 g/m^3; for sea salts, this corresponds to a maximum temperature of deliquescence of ~85ºC. However, it should be noted that complex mixtures of nitrate and chloride salts, potentially relevant at inland sites and even at coastal sites, may deliquesce at much higher temperatures. Existing experimental work investigating stress corrosion cracking of stainless steel in marine environments indicates that SCC is likely to occur under storage conditions. However, test conditions may not be representative of field conditions for several reasons. The experiments use synthetic sea water as the salt source, while field studies show that other salt components, including ammonium and nitrate, are significant in atmospheric aerosols even in near-marine environments. Moreover, experimental designs limit gas-phase exchange with the atmosphere, which can modify salt compositions after deposition or after deliquescence. Finally, experiments do not assess the effects of other components in dust, such as organics or pH-buffering minerals, in either reducing or increasing the corrosivity of deliquesced brines in dust.

Because of the uncertainty in the composition of dusts on the surface of storage containers, the Electrical Power Research Institute and the U.S. Department of Energy have initiated a sampling program for *in situ* dust deposits on current storage containers. This program will provide critical compositional data for new stress corrosion cracking studies, and will allow evaluation of the applicability of existing studies of stainless steel stress corrosion cracking under conditions of dust deliquescence.

Sandia is collaborating with EPRI on the dust sampling, analyzing the dusts and aiding in data interpretation. Two samples of dust that were collected from the surface of interim storage containers at the Calvert Cliffs ISFSI were delivered to Sandia and were characterized using several different methods. Dust collected from the packages at Calvert Cliffs displays a bimodal size distribution, with a coarser fraction (~20 – 40µm in diameter) that consists largely of pollen and quartz grains. The finer fraction (<5 µm in diameter) consists of both soluble salts (sulfates, nitrates, chlorides, and carbonates) and insoluble minerals (silicates and oxides). The soluble cations in the dust are dominated by Ca^{2+}, and the anions, by SO_4^{2-}. Chloride comprises only a small fraction of the total solubles, and SEM analysis indicate that it is present almost entirely as NaCl.

It is clear that, despite the location of the Calvert Cliffs ISFSI adjacent to Chesapeake Bay, the salts deposited on the storage containers are not sea salts. Rather, they are compositionally similar to salts from continental sites. Sea salt aerosols are characterized by high concentrations of Na^+, Mg^{2-}, and Cl^- relative to continental salts, which are richer in Ca^{2+}, NH_4^+, SO_4^{2-}, and NO_3^-. Ammonium and nitrate are more strongly affected by degassing reactions, however, than the other two components. The salts sampled from the storage containers are dominantly calcium sulfate-rich; chloride is a trace species, present largely as NaCl. While particle-gas conversion reactions such as those described in Section 2.2 can modify deposited salts after deposition, these processes only affect the anionic components (e.g., exchange of nitrate or sulfate for chloride); they do not affect the alkali metal or alkaline earth concentrations. The trace amounts of Na in the soluble fraction of the dust samples indicate that only a very small fraction of the salts could be marine in origin.

In an effort to determine if there is indeed a potential for deliquescent brines to result in extensive localized corrosion, or if any localized corrosion will stifle due to limitations as described above, a series of experiments has been (and continues to be) performed. Materials of interest have been decorated with

thin layers of salt in the presence of an occluded geometry in an effort to establish if localized corrosion (i.e., crevice corrosion) could initiate and propagate under such conditions. In these experiments, no inert species were added, so potential physical sequestration of the brine by the dust layer due to capillary forces have been eliminated, allowing all of the material deposited on the metal surface to participate in the corrosion reaction.

Experiments performed on 304 stainless steel, a material used to manufacture interim storage containers for a number of manufacturers, demonstrated that localized corrosion was able to initiate and propagate into the material. Assessment of stifling requires characterization of the extent of corrosion as a function of exposure time. While characterization of the test samples continues at this time, results to date from specimens with mass loadings from 50 to 200 $\mu g/cm^2$ of chloride bearing salt exposed to an elevated temperature and dewpoint for time intervals from 7 to 100 days suggest that stifling has not yet taken place. Additional tests and more detailed analyses are planned, as discussed above.

5.   REFERENCES

ASTM (2001 [R 2012]) *Method G78: Standard Guide for Crevice Corrosion Testing of Iron-Base and Nickel-Base Stainless Alloys in Seawater and Other Chloride-Containing Aqueous Environments.* West Conshohocken, PA: ASTM International.

ASTM International (2008) *D1141-98: Standard Practice for the Preparation of Substitute Ocean Water.* West Conshohocken, PA: American Society for Testing and Materials.

Calvert Cliffs Nuclear Power Plant LLC (2013a) *Response to Request for Additional Information, RE: Calvert Cliffs Independent Spent Fuel Storage Installation License Renewal Application (TAC No. L24475).* Lusby, MD. ADAMS ML13170A574,:

Calvert Cliffs Nuclear Power Plant LLC (2013b) *Attachment 1. Calvert Cliffs Response to RAI #E-3.* Lusby, MD. ADAMS ML13119A243,:

Chang, M. C., Sioutas, C., Kim, S., Gong, H. and Linn, W. S. (2000) Reduction of nitrate losses from filter and impactor samplers by means of concentration enrichment. *Atmospheric Environment* **34**(1)**,** 85-98.

Cook, A., Duff, J., Stevens, N., Lyon, S., Sherry, A. and Marrow, T. J. (2010) Preliminary evaluation of digital image correlation for in-situ observation of low temperature atmospheric-induced chloride stress corrosion cracking in austenitic stainless steels. *ECS Transactions* **25**(37)**,** 119-132.

DOE (2011) *Title 10 CFR part 72.42: Licensing Requirements for the Independent Storage of Spent Nuclear Fuel and High-Level Radioactive Waste.* Washington D.C.: Nuclear Regulatory Commission.

Enos, D. (2012) Impact of Atmospherically Deposited Contaminants on Materials of Interest for the Interim- and Long-Term Storage of High-Level Nuclear Waste. *In: Corrosion 2012*, Salt Lake City, UT. NACE. paper no. 1525.

EPRI (2006) *Climatic Corrosion Considerations for Independent Spent Fuel Storage Installations in Marine Environments.* Report # 1013524, Palo Alto, CA: Electric Power Research Institute.

Gellrich, G. H. (2012) *Calvert Cliffs Independent Spent Fuel Installation Lead and Supplemental Canister Inspection Report.* NRC Document ID ML12212A216: Calvert Cliffs Nuclear Power Plant LLC.

Hanson, B., Stockman, C., Alsaed, H., Enos, D., Meyer, R. and Sorenson, K. (2011) *Gap analysis to support extended storage of used nuclear fuel.* FCRD-USED-2011-000136: U.S. Department of Energy.

Hitchcock, D. R., Spiller, L. L. and Wilson, W. E. (1980) Sulfuric acid aerosols and HCl release in coastal atmospheres: Evidence of rapid formation of sulfuric acid particulates. *Atmospheric Environment* **14,** 165-182.

Holtec International (2010) *HI-STORM FSAR, Rev. 8.*

Kain, R. M. (1990) Marine atmosphere corrosion cracking of austenic stainless steels. *Materials Performance* **29**(12)**,** 60-62.

Kelly, R. G., Agarwal, A. S., Cui, F., Shan, X., Landau, U. and Payer, J. (2006) Considerations of the Role of the Cathodic Region in Localized Corrosion. *In: International High-Level Radioactive Waste Managment Conference (IHLRWMC)*, Las Vegas, NV. American Nuclear Society.

Marcolli, C., Luo, B. P. and Peter, T. (2004a) Mixing of the organic aerosol fractions: Liquids as the thermodynamically stable phases. *Journal of Physical Chemistry A* **108**(12)**,** 2216-2224.

Marcolli, C., Luo, B. P., Peter, T. and Wienhold, F. G. (2004b) Internal mixing of the organic aerosol by gas phase diffusion of semivolatile organic compounds. *Atmospheric Chemistry and Physics* **4**2593-2599.

Ming, Y. and Russell, L. M. (2002) Thermodynamic equilibrium of organic-electrolyte mixtures in aerosol particles. *Aiche Journal* **48**(6)**,** 1331-1348.

Mintz, T. S., Caseres, L., He, X., Dante, J., Oberson, G., Dunn, D. S. and Ahn, T. (2012) Atmospheric Salt Fog Testing to Evaluate Chloride-Induced Stress Corrosion Cracking of Type 304 Stainless Steel. *In: Corrosion 2012*, Salt Lake City, March 11-15. NACE.

NAC International (2005) *NAC-UMS FSAR, Rev. 5*.

NADP. 2013. *National Trends Network* [Online]. National Airfall Deposition Program. Available: http://nadp.sws.uiuc.edu/ntn/.

Nakayama, G. (2006) Atmospheric stress corrosion cracking (ASCC) susceptibility of stainless alloys for metallic containers. *In:* VanIseghem, P. (ed.) *Scientific Basis for Nuclear Waste Management XXIX*. **932**. pp. 845-852.

Parsons, M. T., Knopf, D. A. and Bertram, A. K. (2004) Deliquescence and crystallization of ammonium sulfate particles internally mixed with water-soluble organic compounds. *Journal of Physical Chemistry A* **108**(52)**,** 11600-11608.

Payer, J., Shan, X., Agarwal, A. S. and Landau, U. (2008) Crevice Corrosion Processes in Thin Films of Electrolyte. *NACE Corrosion Conference, March New Orleans, LA* Paper no. 08266.

Peterman, Z. E. (2008) Effects of Temperature on the Compositions of Soluble Salts in Dust at Yucca Mountain. Presentation to the Nuclear Waste Technical Review Board, Jan. 16, 2008. Las Vegas NV: U.S.G.S.

Peterman, Z. E. (2009) Thermal Experiments on Atmospheric and Subsurface Dust at Yucca Mountain, Nevada. Presentation to the Nuclear Waste Technical Review Board, Jan. 28, 2009. Las Vegas NV: U.S.G.S.

Pio, C. A. and Lopes, D. A. (1998) Chlorine loss from marine aerosol in a coastal atmosphere. *Journal of Geophysical Research-Atmospheres* **103**(D19)**,** 25263-25272.

Prosek, T., Iversen, A. and Taxén, C. (2009) Low temperature stress corrosion cracking of stainless steels in the atmosphere in presence of chloride deposits. *Corrosion* **65**(2)**,** 105-117.

Rossi, M. J. (2003) Heterogeneous reactions on salts. *Chemistry Reviews* **103**(12)**,** 4823-4882.

Seinfeld, J. H. (1986) *Atmospheric Chemistry and Physics of Air Pollution.* New York, NY: John Wiley & Sons.

Shan, X. and Payer, J. (2007) Comparison of ceramic and polymer crevice formers on the crevice corrosion behavior of Ni-Cr-Mo Alloy C-22. Paper No. 07582. *In: CORROSION/2007*, Houston, TX. NACE International.

Shirai, K., Tani, J., Arai, T., Wataru, M., Takeda, H. and Saegusa, T. (2011) SCC evaluation test of a multi-purpose canister. 10-14 April. *In: 13th International High-Level Radioactive Waste Management Conference (IHLRWMC)*, 824-831. American Nuclear Society.

SNL (2008) *Analysis of dust deliquescence for FEP screening*. ANL-EBS-MD-000074 REV01, Albuquerque, NM: Sandia National Laboratories.

Suffield, S., Fort, J. A., Cuta, J. M. and Adkins, H. E. (2012) *Thermal Modeling of NUHOMS HSM15 Storage Module at Calvert Cliffs Nuclear Power Station ISFSI*. FCRD-UFD-2012-000114: U.S. Department of Energy.

Tani, J. I., Mayuzurmi, M. and Hara, N. (2009) Initiation and propagation of stress corrosion cracking of stainless steel canister for concrete cask storage of spent nuclear fuel. *Corrosion* **65**(3)**,** 187-194.

Transnuclear Inc. (2007) *NUHOMS-HD FSAR, Rev. 0*.

Transnuclear Inc. (2008) *NUHOMS FSAR, Rev. 10*

Turnbull, A. (1997) Implications of internal cathodic reactions for crevice attack of stainless steels in chloride environments. *British Corrosion Journal* **32**(4)**,** 283-290.

Zhang, X. and McMurry, P. H. (1992) Evaporative losses of fine particulate nitrates during sampling. *Atmospheric Environment* **26A**(18)**,** 3305-3312.